Simplified fatigue assessment of offshore wind support structures accounting for variations in a farm

Vasileios Michalopoulos

Master of Science Thesis

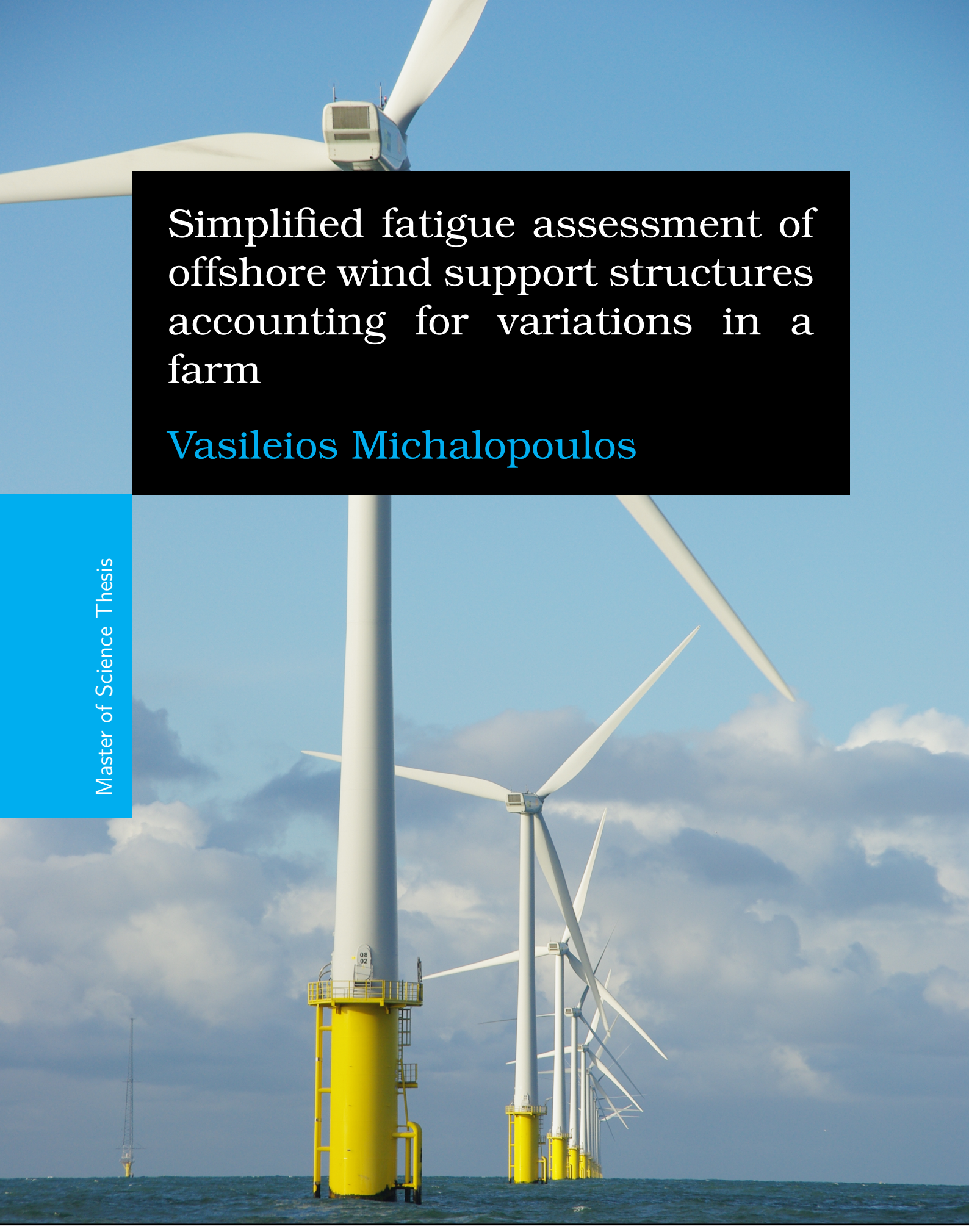

TU Delft Delft University of Technology

Simplified fatigue assessment of offshore wind support structures accounting for variations in a farm

Master of Science Thesis

For the degree of Master of Science in Sustainable Energy Technology
at Delft University of Technology

Vasileios Michalopoulos

Supervisor:

Dr.Ir. M. Zaaijer

July 10, 2015

Faculty of Aerospace Engineering (AE) and Applied Sciences (AS)

TU Delft Delft University of Technology

Delft University of Technology
Department of
Wind energy, Aerospace Engineering

The following academic staff certifies that it has read and recommends to the Faculty of Aerospace Engineering (AE) and Applied Sciences (AS) for acceptance a thesis entitled

Simplified fatigue assessment of offshore wind support structures accounting for variations in a farm

by

Vasileios Michalopoulos

in partial fulfillment of the requirements for the degree of

Master of Science Sustainable Energy Technology

Dated: July 10, 2015

Supervisor: Dr.Ir. M. Zaaijer

Readers: Prof. G. van Bussel

Dr.Ir. M. Zaaijer

Dr.Ir. E.M. Lourens

Abstract

The optimal design and preliminary strength assessment of offshore wind support structures gain growing interest given the potential to drive the costs further down. This study develops a framework for Fatigue Limit State (FLS) estimations of monopiles in a simple and quick manner so as to address site variations in an offshore wind farm (OWF). Additionally, it serves the need for optimisation of all structures in the farm in the early design phase. The framework consists of two elements: *(a)* a stand-alone model that predicts in a simplified way the damage caused by the varying loading and *(b)* correction factors that increase its reliability. The concept of the model relies on the analytical approximation of the dynamic response, thus bypassing time consuming numerical processes and advanced software. The above step renders it a simplified version of the conventional frequency-domain. Its benchmarking against the time-domain aeroelastic code Bladed yields sufficient accuracy but also certain systematic errors. Effectively, these are tackled by the correction factors that are generated at a reference position where time-domain detailed assessment is necessary. Once calculated, they are transferred to the positions of interest in the farm. A case study examining the variations in a site shows an efficient performance of the proposed scheme specifically at the parts of the structure close to the seabed with errors lower than 5 % with respect to the outcome of Bladed. Finally, provided the fatigue estimations at every location, the foundation piles are designed individually in order to fulfill the target of mass reduction. By using the outcome of the case study as input for the tailoring of the geometry, it is shown that a considerable amount of steel, up to 16 %, can be saved.

Table of Contents

List of Figures

List of Tables

Acknowledgements

I would like to sincerely express my gratitude to my supervisor Dr.Ir. Michiel Zaaijer. The close cooperation at every stage, the elaborate discussion on approaches but most importantly his triggering comments were vital for the finalisation of this thesis. In addition, I am thankful for his willingness to support my efforts to get across the concept of this study to the scientific community.

Special thanks go to Dr.Ir. Eliz-Mari Lourens who kindly gave me access to Bladed at many stages and without time restrictions. Besides that, my motivation to get involved with the field of offshore wind support structures resulted from the corresponding courses she was instructing.

Finally, I couldn't forget the people I daily shared the student room with at the Faculty of Aerospace. A genuinely pleasant atmosphere was created which was always giving rise to interesting discussions and opinion sharing.

Delft, University of Technology
July 10, 2015

Vasileios Michalopoulos

Nomenclature

List of Symbols

α_{sh}	power law exponent
$\bar{U}$	mean wind speed
$\Delta\sigma_{EQ}^{ref}$	equivalent stress at the reference position (target for tailored design)
$\Delta\sigma$	stress range
$\Delta\sigma_{EQ}$	equivalent stress
Δr	length of blade element
$\dot{u}_w$	water particle acceleration
γ	unit weight
λ	wavelength
$[K_e]$	mass matrix
$[K_g]$	geometric stiffness matrix
$[K_s]$	soil stiffness matrix
$[M_e]$	elastic mass matrix
Ω	rotational speed of the rotor
ϕ	friction angle
ρ_{air}	air density
ρ_{wat}	water density
σ_i	standard deviation of wind speed in i direction
θ	rotor azimuth
ξ	damping ratio
b	rotor overhang
C_u	undrained shear strength
$C_{D,T}$	tower drag coefficient
C_L	lift coefficient
C_M	moment coefficient
D	rotor diameter
d	water depth

$D_P^{'}$	pile diameter of tailored design
D_P	pile diameter
D_{SS}	secondary steel diameter
D_{TP}	transition piece diameter
D_T	tower diameter
DAF	dynamic amplification factor
$Damage$	fatigue damage
DEL	damage equivalent loads
DEL^{new}	damage equivalent loads at the new location
dF_D	incremental aerodynamic drag
dF_L	incremental aerodynamic lift
$e50\%$	strain for 50% of the maximum strength
f	frequency
f_p	wave peak frequency
F_{1P}	1P centrifugal force
$f_{H,D}$	drag hydrodynamic force
$f_{H,M}$	inertia hydrodynamic force
f_H	total hydrodynamic force
f_{lim}	limit unit skin friction
$f_{T,dyn}$	dynamic term of tower drag
f_T	tower drag
Fz	vertical force
g	acceleration of gravity
H_s	significant wave height
I	moment of inertia
k	wave number
KC	Kreulegan-Carpenter number
L_S	scour depth
L_v	integral length scale
m	inverse slope of S-N curve
M_{1P}	1P moment range
m_{1P}	mass imbalance
M_{3P}	3P moment range
$M_{T,dyn}$	moment by the dynamic term of tower drag
N	allowable cycles to failure
n	cycles present in a loading signal
N_q	bearing capacity factor
N_{EQ}	equivalent cycles
q_{lim}	limit unit end bearing pressure
R_{1P}	radial position of mass imbalance

$S_{\Delta\sigma}$	(normal) stress spectral density
S_{Fz}	vertical force spectral density
S_{JS}	JONSWAP spectrum
S_{Kaimal}	Kaimal turbulence spectrum
S_{Karman}	Von Karman turbulence spectrum
$S_{MM,wave}$	spectral density of (mudline) moment by hydrodynamic load
$S_{MM,total}$	spectral density of (mudline) moment by aerodynamic and hydrodynamic loading
$S_{MM,wind,R}$	spectral density of (mudline) moment by rotor thrust
$S_{MM,wind,T}$	spectral density of (mudline) moment by tower drag
$S_{MM,wind}$	combined spectral density of (mudline) moment by aerodynamic load
S_{PM}	Pierson-Moskowitz spectrum
S_{uu}	spectral density of wind field
S_{ww}	spectral density of the sea state
T	thrust
T_p	wave peak period
t_P	pile thickness
$t_P^{'}$	pile thickness of tailored design
T_{dyn}	dynamic thrust
TI_i	turbulence intensity in i direction
TRF	transfer function
U	instantaneous wind speed
u	turbulent wind speed around mean
u_w	water particle velocity
U_{3P}	resultant velocity (disturbed by the tower shadow)
U_{tower}	wind speed deficit by the tower shadow)
W	relative velocity
z	elevation
z_o	surface roughness
z_{ref}	reference height

Chapter 1

Introduction

This first chapter of the thesis familiarises the reader with the topic and all the related issues. More specifically, the necessary background information is firstly provided so that the reader identifies the field of research to which the present work is aligned. Additionally, this information gives an insight in the most relevant and recent developments and describes in general the status quo. Next, the problem that is here addressed is analysed and the methods that are followed towards its solution are discussed. Finally, the translation of the present work in terms of industry benefit and usefulness is proven by presenting the objectives. As for the last section, this explains the structure of the thesis by giving the outline of the following chapters.

1-1 Background Information

Despite the substantial decrease of the cost of offshore wind energy over the last years, a further and radical drop is essential to effectively compete with other energy sources [23]; the most recently defined targets have been set to 40% reduction by 2020. Unlike onshore wind energy, the contribution of the turbine system to the overall cost is lower, giving thus rise to the share of the foundation and installation to around 27% [5]. This capital cost breakdown shows the direction in which cost-decreasing technologies should go.

With respect to the support structure design, the orientation that developers currently follow is the division of the entire farm into clusters and design for the most onerous set of site conditions of each such portion. Hence, meeting the structural requirements of the most challenging position implies suitability for the other positions as well [13] [7]. Consequently, this procedure does not provide fully site-specific support structure design. As a result, the majority of the structure within a wind farm are over-dimensioned. A significant amount of the offshore wind-related research is conducted on the principles of these site-specific aspects. Particularly the prospects of cost reduction of support structures without compensating with lower structural integrity have motivated the development of optimisers. Main goal of the latter is the most efficient design through an extensive analysis of the given parameters such

as environmental data and site conditions. Some of the most worth-highlighting efforts are briefly presented in the following paragraphs.

Thiry, Bair, Buldgen, Raboni and Rigo formulated an optimisation scheme for a monopile by coupling an analyser with a genetic algorithm [45]. With the minimisation of the weight as cost function/objective and the structural criteria as constraints, a powerful tool was created. After testing this algorithm in a case study, they claimed an impressive 20% support structure cost reduction. However, the probabilistic nature of the use of evolutionary algorithms introduces a degree of uncertainty to the scheme.

Fischer, Rainey, Bossanyi and Kühn, who focused on fatigue loading considering that it becomes design governing for deeper water and/or larger turbines, were involved in the optimisation process from another perspective: through the addition of the operational control level as an extra degree of freedom in the problem [12]. By adjusting the controller set-up appropriately so that the fore-aft motion of the system is sufficiently damped and the fatigue loading reduced, they achieved structure that was lighter by 7%. Despite the promising outcome, the limited access that a foundation designer has to the controller of the turbine poses in dispute to what extent this approach can be implemented in practice.

An even more complex framework targeted at site-sensitive design, consequently at site-specific optimum monopiles, was later introduced again by Fischer and Kühn [13]. They innovated by designing support structures with natural frequency within the 1P region and simultaneously increasing the rated rotational speed of the rotor. These two enabled them to shift the resonance to the partial load area, having thus the possibility to apply an operational window to the resonance frequency by adjusting the controller accordingly. The test case on an offshore wind farm (OWF) with several site variations showed approximately 7% cost reduction of each structure. On the other hand, the difficulties with regards to the close cooperation of the turbine manufacturer (that is responsible for the controller) and the foundation designer remains as before. This cooperation would be required for such an approach.

Evidently, putting for now aside the details of the optimisers, what is here worth to mention regarding these models is the importance of the constraints, as they affect massively the result. Furthermore, they have a strong impact on the speed of the calculations. The above models are indeed powerful and capable of addressing the earlier defined problems; undeniably, in a more efficient way than the regular straight-forward and detailed (but simultaneously rather time-consuming) design. As it has become to the industry stakeholders clear by now how great the benefits originating from growing interaction between the design stages are, reliable estimations of the systems' performance are vital even from early phases. Focusing on the initial design steps, it is therefore beneficial to reduce the complexity of among others the structural assessment, a part of which includes the Fatigue Limit State (FLS).

To this direction, extensive research on fatigue assessment has been conducted, the most interesting of which shortly follow. The basis of fatigue analyses is the framework of time-domain assessment and is nowadays considered to be the main practice, especially when advanced software is used for this purpose. However, certain bottlenecks that accompany this approach have alternatively shifted the interest of researchers to the frequency domain. The strong points of the latter, as discussed later in this report, come in agreement with the desired reduction of complexity. On top of that, the wide application of the frequency domain in the offshore oil and gas industry is an even more stimulating fact.

Already in 2001, Kühn studied the dynamics of offshore wind turbines and investigated the prospects of simplifying the fatigue calculations based on the principles of frequency spectra [24]. Van der Tempel placed emphasis on the validation of the frequency domain by comparison of the results with those of time-domain analysis for several operational wind farms [46]. Additionally, he tested the uncoupled approach which is on the one hand not the optimal but on the other hand realistic in the status quo of the industry.

Finally, moving to the latest and state-of-the-art fatigue-related studies, Seidel treated the issue of wave induced fatigue loads on monopiles in the principles of the frequency-domain and got involved in new approaches for lumping of scatter tables and site-specific equivalent loads [38]. Furthermore, Alati, Nava, Failla, Arena and Santini applied the frequency-domain framework with the motivation to assess the damage equivalent loads of various types of support structures and come to the optimum [1]. Lately, Peeringa approached the effect of currents on waves and ultimately their effect - combined with the wind load - on the fatigue of the support structure by working with frequency spectra [33]. Finally, a detailed spectral fatigue assessment under wind and wave loading was also performed by Yeter, Garbatov and Soares [52].

1-2 Problem Analysis

The motivation of the thesis lies on the prediction of the resistance of support structures within a wind farm to cumulative damage caused by varying loads. Additionally, it emphasises particularly on the extent to which this prediction can be conducted by simplified yet still reliable means.

Targeting to the early design phase, the working principles of the developed FLS assessment should not be computationally expensive and complex. The highly iterative nature of this design stage necessitates flexibility, identification of critical aspects and disregard of the non-governing ones. This can be accomplished only by simplifying the engaged steps. In principle, a simplification of any calculation may often sound convenient but this poses numerous challenges: among others, uncertainty of the results and thorough knowledge for the distinction between valuable and trivial design variables. Therefore, all aspects need be looked at extensively as well as critically.

The problem analysis relies on an acknowledged limitation: simplified estimation of fatigue at several locations cannot be a stand-alone process. The effect of site variations can be accurately captured only when a detailed assessment at a certain location serves as the starting point. The analysis should therefore be based on a reliably calculated resistance to cyclic loading and then on the extrapolation of this resistance to the rest of the locations. This comprises the main concept of the research in this thesis. Effectively, the framework is structured on the grounds of the analysis in two positions: the *reference* and the *new* position. The desirable speed-up is achieved provided that the meticulous and time-consuming analysis is conducted only once for the reference position. In other words, the baseline location does not have to be investigated repeatedly and quick estimations for the locations of interest are made instead.

The realisation of this concept requires primarily the development of a suitable methodology for FLS assessment (also referred to as *framework* or *methodology* in following chapters).

Target of this methodology is to examine the response of the system to varying loading and estimate the cumulative damage over the lifetime (*Simplified Fatigue Assessment* of Fig. 1-1). The challenge of this stage lies on the level at which the complexity of the process can be reduced. The flexibility is gained by appropriate structuring of this methodology so that the excitation is captured in a distinct manner. Prerequisite of this, however, is the identification of the specific type of excitation (*Fatigue Parameters*), originating from the environment, that rises the fatigue of the structure. As mentioned earlier, the basis of the above is the in-depth assessment (*Detailed Fatigue Assessment*) that eases the extrapolation by leading to necessary corrections (*Correction Factors*). Once the latter are transported to the new location, the location-specific damage can finally be estimated.

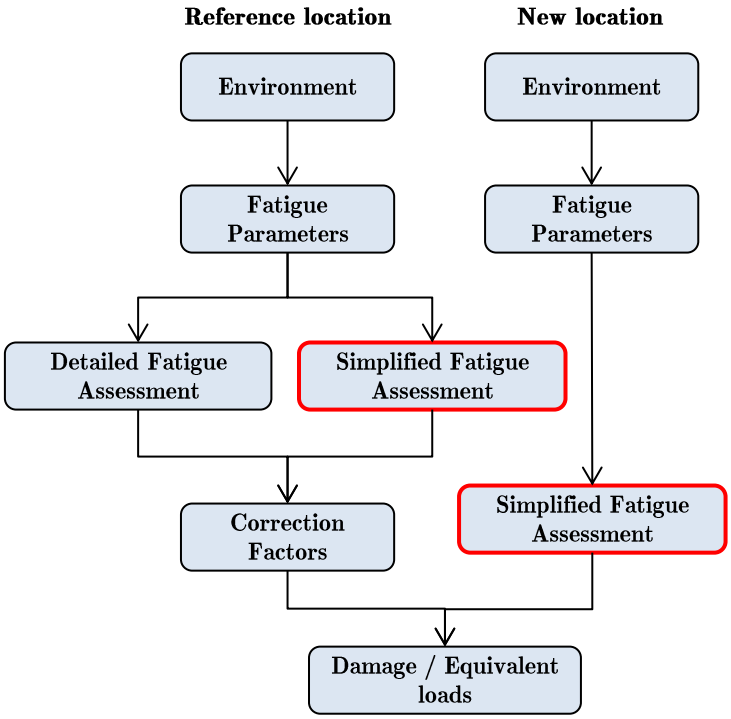

Figure 1-1: Proposed model for the realisation of fatigue extrapolation from a reference position to the rest of the locations within an OWF

The fatigue damage varies over the farm depending on the local conditions when the aforementioned estimations are made. As a last step, the adjustment of the design specifically for each location follows. It aims to optimise the structures individually and thus prevent overdimensioning. The tailored design is in this study driven by FLS which renders this procedure suitable for the first phase of the design similarly to the methodology for FLS extrapolation.

1-3 Objectives

The ultimate target is to enhance the decision-making process throughout the first interfering development stages of an OWF. By supplying the developers with this solid framework for

the sub-structure analysis, the initial phase capabilities are further extended: from energy yield and rough cost estimations to assessment of the very uncertain structural strength. To accomplish the above, this framework should be able to:

- provide OWF layout designers with an additional parameter to evaluate, besides wake losses and internal cabling costs: how does positioning of turbines affect fatigue in support structures?
- facilitate financially strategic choices when it comes to support structure design clustering or tailored design: how many different support structure designs should be used within the farm?
- enable the investigation of various proposals by increasing the time-efficiency: how many more design choices can be evaluated compared to the time-consuming detailed procedure?

The areas for which this research can be an asset are numerous as described above. Firstly, the design of the wind farm layout can be enriched by an additional indicator of suitability: location-specific fatigue damage estimations. The commmon-practice for this procedure is in most cases limited to the investigation of the trade-off between wake effects and internal cabling costs. This can be characterised insufficient. The framework here targets to identify structural risks which would conventionally be done in a far more complex way and supply this knowledge to the layout designers.

Moreover, big discussions always rise with regards to the advantages and disadvantages of tailored and mass produced foundations. It would perhaps be very optimistic to argue that the answer is given by the present research study. However, the identification of specific areas within a site that either favour the mass production or require customised structures is undeniably a plus. Defining the cluster strategy can be hugely assisted by the effective translation of site variability into variation of structural reliability on which this project emphasises. Especially when a tailored geometry is at the end of the procedure suggested for each location, it becomes clear that a wind farm developer can conclude to the most efficient choice.

Furthermore and very related to the above, the time-efficiency of the required procedures is expected to increase. To be more specific, the desired simplification of the developed methodology enables a broad assessment of either numerous locations or designs. The same number of simulations would evidently be difficult to be assessed with the conventional detailed framework. Ultimately, this flexibility reduces engineering costs.

Finally but most importantly, the conclusion is that the gain to each and every aspect can in the long term benefit the realisation of a global and multi-objective optimisation of the development process of an offshore wind project. This would require rigorous assessment of the dependencies between diverse aspects: permitting process, layout design, structure specifications, component selection, O& M strategies and more. Although, it is unanimously acknowledged by all engaged parties, e.g. developers, financiers, suppliers etc., that this has the potential to lead to decisive cost reduction, there are several obstacles. The multi-disciplinary fields and hugely interfering procedures are detrimental for the progress. Therefore, there is currently no alternative to the straight-forward design process with time-consuming (therefore only limited) feedback and with disputably optimum results.

1-4 Thesis Outline

The thesis consists of 8 main chapters. Chapter 1 introduces the topic: the problem that is principally addressed, the method to solve it and the motivation behind this work. Before that, it familiarises the reader with the presently predominant approaches of problems at the offshore wind industry with regards to the support structures and presents state of the art research on this field. Next, the most relevant parts of the background theory are given briefly by Chapter 2 for the sake of completeness.

The framework for simplified FLS assessment, which is the core of the present research, requires firstly a discussion that serves as a basis for its development. This discussion can be found in Chapter 3. As for the proposed methodology itself, it is rigorously presented in Chapter 4. In the same chapter, it is also validated.

The variations in a farm are treated making use of this methodology at a first stage individually in Chapter 5. In addition, observations that are worth to highlight are extracted by the sensitivity analysis given in the same chapter. Chapter 6 demonstrates the effectiveness of the incorporation of the proposed methodology (as presented in Chapter 4) in a scheme that extrapolates the results of FLS analyses to several locations in an OWF under combined variations. This is achieved by formulating a case study and applying the correction factors that are introduced (but not applied) in Chapter 5.

Finally, a scheme for tailored design of support structures is developed and proposed in Chapter 7. Its funcionality is tested based on the outcome of the case study of Chapter 6. As for the conclusions that stem throughout all the phases of this thesis work, these are provided in Chapter 8 along with useful suggestions on future work.

Chapter 2

Background Theory

The generation of electricity from wind off the mainland is accompanied by technical challenges originating from the multidisciplinary engineering fields that offshore wind comprises. For the sake of completeness and since the majority of these aspects are treated in following chapters, some basics of offshore wind are presented. For more detailed content, the reader can refer to textbooks [27][6].

2-1 Wind

This section includes the basic characteristics of the wind: wind turbulence, shear and finally the loading that these exert on a structure.

Wind Speed and Turbulence

Accounting for time variations of the wind, the wind speed at height z is given by the following equation:

$$U(z,t) = \bar{U}(z) + u(z,t) \tag{2-1}$$

where U the instantaneous wind speed at time t, $\bar{U}$ the mean wind speed (constant in magnitude over a time period Δt with $0 \leq t \leq \Delta t$) and u the turbulent wind speed around the mean speed $\bar{U}$.

The typical wind spectra over a broad range of frequencies show that the mean wind speed over a period of about 10 minutes can be regarded as constant, forming a wind state: a state during which only the turbulence term fluctuates. Focusing on the wind direction i, a time-series of wind speed is characterised by a mean wind speed and a standard deviation. These define the turbulence intentsity as follows:

$$TI_i = \frac{\sigma_i}{\bar{U}} \tag{2-2}$$

where TI_i is the turbulence intensity in i direction and σ_i the standard deviation of wind speed in i direction.

The spatial variation of the wind speed implies three terms of turbulence intensities: longitudinal, lateral and vertical. An isotropic turbulence is considered when $TI_x = TI_y = TI_z$. The most widely used turbulence models are the von Karman and Kaimal spectra:

$$S_{Karman}(f) = \frac{\sigma_i^2 4L_v/\bar{U}}{(1 + 70.8(fL_v/\bar{U})^2)^{5/6}} \tag{2-3}$$

$$S_{Kaimal}(f) = \frac{\sigma_i^2 4L_v/\bar{U}}{(1 + 6fL_v/\bar{U}^{5/3})} \tag{2-4}$$

where f is the frequency and L_v the integral length scale. For a detailed presentation of both models the reader can consult the standards [43].

Wind Shear

The phenomenon during which the friction caused by the Earth's surface reduces the wind speed is defined as wind shear. This phenomenon is observed in the lowest part of the atmosphere: the atmospheric boundary layer as Fig. 2-1 illustrates. Similarly to the turbulence, wind shear has a great impact not only on the power estimation of a wind turbine but also on the loading of a structure.

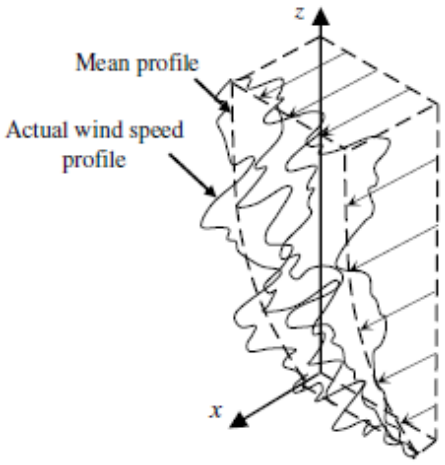

Figure 2-1: The wind shear caused by the atmospheric boundary layer [27]

This variation of horizontal wind speed with height can be described by two models: the logarithmic profile (law) and the power law. Both are strongly related to the complexity of the terrain. A rough terrain produces momentum wakes and eddies that result in a disturbed flow, hence with decreased wind speed. The aforementioned models are presented by the following equations accordingly:

$$U(z) = U(z_{ref}) \frac{ln(z/z_o)}{ln(z_{ref}/z_o)} \tag{2-5}$$

$$U(z) = U(z_{ref}) \left(\frac{z}{z_{ref}} \right)^{\alpha_{sh}} \tag{2-6}$$

where $U(z_{ref})$ is the mean wind speed at the reference height, z_o the surface roughness, z_{ref} the reference height $(10m)$ and α_{sh} the power law exponent.

Aerodynamic Loading

The wind-induced loads that are exerted on the rotor are derived on the basis of the Blade Element Momentum (BEM) theory, a combination of an actuator disc-based theory (Momentum) and a blade element theory [6] [27].

According to Momentum theory, an analysis based on the annular control volume, the conservation of linear momentum to the control volume leads to the calculation of the thrust T:

$$T = C_T \frac{1}{2} \rho_{air} \pi \frac{D^2}{4} \bar{U}^2 \tag{2-7}$$

where C_T is the thrust coefficient, ρ_{air} the air density and D the rotor diameter.

In the blade element theory, a blade consists of a number of elements and the theory describes the forces on a particular element considering it be independent from the rest. The two forces on each element, the incremental lift and drag force, compose the thrust which is normal to the rotation plane. The geometry and velocity vectors are shown in Fig. 2-2. The two components of the thrust (on each element) are calculated as:

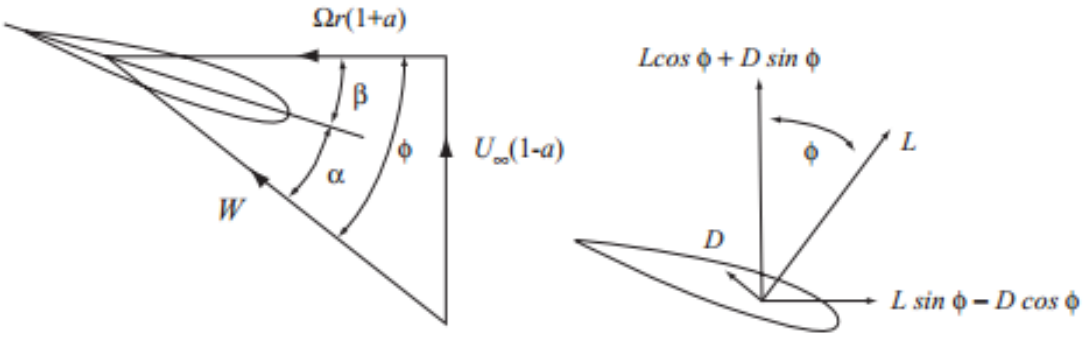

Figure 2-2: Blade geometry and wind vectors of a horizontal axis wind turbine [27]

$$dF_L = C_L \frac{1}{2} \rho_{air} c \Delta r W^2 \tag{2-8}$$

$$dF_D = C_D \frac{1}{2} \rho_{air} c \Delta r W^2 \tag{2-9}$$

where dF_L is the incremental aerodynamic lift, dF_D the incremental aerodynamic drag, C_L the lift coefficient, C_D the drag coefficient, c the chord, Δr the length of blade element and W the relative velocity.

With N_b the number of the blades, the thrust is the integral of the forces along the blade:

$$T = \int_{r=0}^{r=D/2} dF = N_b \int_{r=0}^{r=D/2} (dF_L cos\phi + dF_D sin\phi) \tag{2-10}$$

The rotor is not the only body that interrupts the flow of the wind. A drag force is additionally exerted on the tower and is given (per unit length) as:

$$f_T = C_{D,T} \frac{1}{2} \rho_{air} D_T \bar{U}^2 \tag{2-11}$$

where f_T the tower drag, $C_{D,T}$ the tower drag coefficient and D_T the tower diameter.

Unlike the thrust, the tower drag is a distributed load over the tower which means that the effect of the wind shear is quite visible here. The shape of the tower drag is presented in Fig. 2-3.

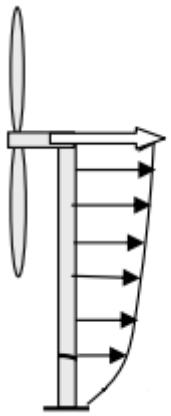

Figure 2-3: Drag force exerted on the tower under wind shear [21]

2-2 Waves

The sea state and particularly the waves is the other crucial environmental state for offshore wind, the conditions of which are largely experienced by the structures. As for the currents, these are in the majority of the studies neglected when investigating fatigue, therefore they are omitted here as well [38] [46] [36].

Wave Theories

There are three parameters to describe a sea surface: i) the height of the elevation with respect to still water line/level (amplitude of the wave), ii) the time between passing of equal

elevations from a fixed point (zero-crossing or peak period) and iii) the direction in which the waves propagate. Upon these parameters the following wave models are formulated. There are two basic models that describe the waves: the deterministic (periodic) and the probabilistic (random) model.

- Periodic wave model

  The periodic model consists of either linear or non-linear theory meaning that there is only one frequency present or the wave consists additionally of higher harmonics respectively. All models assume uni-directional propagation. According to Fig. 2-4, the theory is highly dependent on the (normalised) water depth and wave height. Clearly, the linear wave, or Airy theory, is mostly applicable to deep water depths and for waves with infinitely small wave amplitude. On the contrary, for intermediate water depths the Stoke's higher order theories are capable of representing the waves and for shallow water cnoidal and solitary waves have been developed.

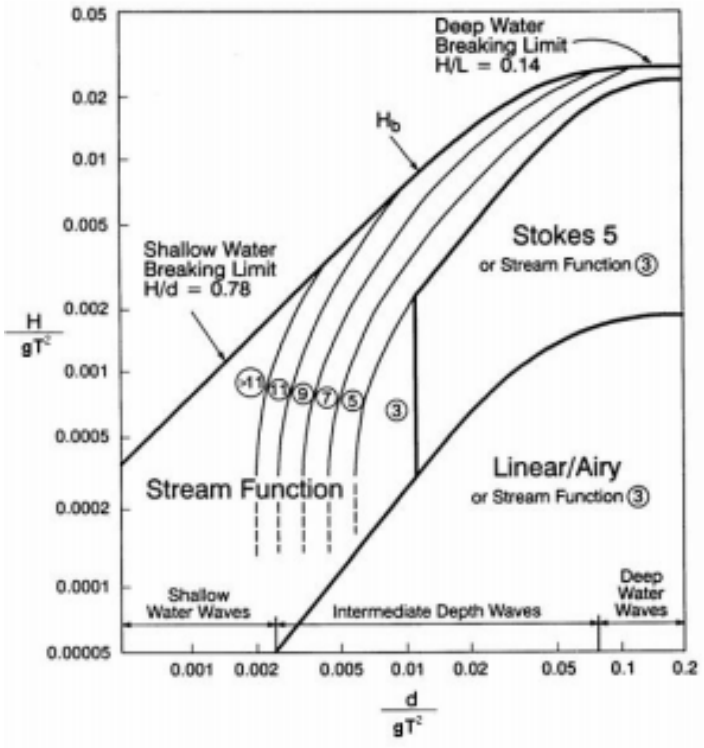

Figure 2-4: Wave theory selection graph [49]

- Random wave model

  The linear random wave model has a wide application in the offshore industry. The superposition of an infinite number of random waves with their own amplitude, frequency, direction and phase angle (each of these building components described by the typical periodic wave theory) forms a random sea state. The method is depicted in Fig. 2-5.

Regarding the kinematics, the water particle velocity and acceleration are given by the following equations respectively:

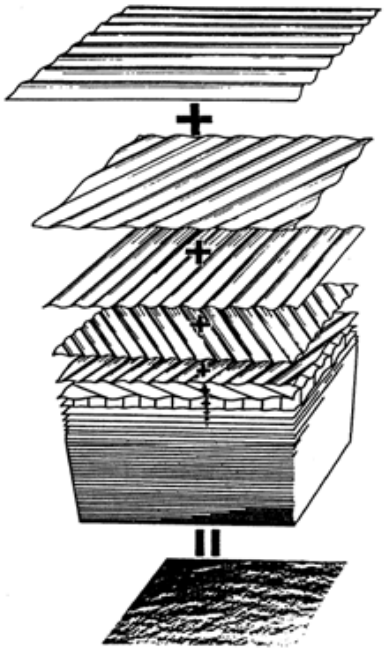

Figure 2-5: A random sea state is formed by superposition of random waves [49]

$$u_w(x,z,t) = \frac{H_s}{2} 2\pi f \frac{cosh(k(z+d))}{sinh(kd)} cos(kx - 2\pi ft) \tag{2-12}$$

$$\dot{u}_w(x,z,t) = \frac{H_s}{2} (2\pi f)^2 \frac{cosh(k(z+d))}{sinh(kd)} sin(kx - 2\pi ft) \tag{2-13}$$

where $u_w(x,z,t)$ the water particle velocity, $\dot{u}_w(x,z,t)$ the water particle acceleration, H_s the significant wave height, λ the wavelength, k the wave number and d the water depth. A limitation of the Airy theory is that it is valid up to the still water level. Therefore, this is faced by Wheeler stretching or other methods which are thoroughly explained in the literature [50].

Wave Spectral Density

The random nature of a real sea can be represented by the superposition of several individual components, with each of them having its own amplitude, frequency and direction of propagation. Neglecting the directional wave spectrum, there are two most frequently used formulations of spectra in the offshore sector: the Pierson-Moskowitz for a fully developed sea (or at infinite fetch) and the JONSWAP for a developing sea (or fetch-limited) spectrum. Unlike the fully developed sea which implies a low-peaked energy density and distribution over a wider frequency range, the fetch-limited spectrum has a sharper peak and significant concentration of the energy density in a narrow range. For a detailed presentation of the spectral densities the reader can consult the standards [10].

- The Pierson-Moskowitz spectrum

  This wave spectrum is developed from measurements in the Atlantic Ocean and after several adjustments over years of development, it is given as:

$$S_{PM}(f) = \frac{\alpha g^2}{(2\pi)^4 f^5} exp\left(-\frac{5}{4}\left(\frac{f}{f_p}\right)^{-4}\right) \tag{2-14}$$

  where S_{PM} the power spectral density (for Pierson-Moskowitz), f_p the peak frequency, γ the peak enhancement factor, g the acceleration of gravity and

$$\alpha = 5\left(\frac{H_s^2 f_p^4}{g^2}\right)(1 - 0.287 ln\gamma)\pi^4 \tag{2-15}$$

- The JONSWAP spectrum

  This is an improved version of the Pierson-Moskowitz based on further measurements of wave spectra in the North Sea. The factor that induces this enhancement is the peak enhancement factor (a function of peak shape parameter and slope factors). Furthermore, in order to retain the total area under the spectrum constant and, thus, represent the real energy density of the sea state despite the application of the peak enhancement factor, a normalising factor is introduced:

$$S_{JS}(f) = \frac{\alpha g^2}{(2\pi)^4 f^5} exp\left(-\frac{5}{4}\left(\frac{f}{f_p}\right)^{-4}\right)\gamma^r \tag{2-16}$$

  where γ is the peak enhancement factor (3.3 for JONSWAP) and

$$r = exp\left(-0.5\left(\frac{f - f_p}{\sigma_{JS} f_p}\right)^2\right) \tag{2-17}$$

$$\sigma_{JS} = \begin{cases} 0.07 for f \leqslant f_p \\ 0.09 for f > f_p \end{cases} \tag{2-18}$$

Hydrodynamic Loading

For the calculation of the hydrodynamic load on slender structures the Morison equation is used. The state of motion of the fluid is distinguished in steady and unsteady flow and these are the two components of the equation: the drag load corresponds to the velocity of the water particles, while the inertia load corresponds to the acceleration of the water particles. The summation of the two result in the total load as Fig. 2-6 illustrates. The aforementioned forces are calculated:

$$f_H(z,t) = f_{H,D}(z,t) + f_{H,M}(z,t) \tag{2-19}$$

$$f_{H,D}(z,t) = C_D \frac{1}{2}\rho_{wat} D_P u_w^2(z,t) \tag{2-20}$$

$$f_{H,M}(z,t) = C_M \frac{1}{4} \rho_{wat} \pi D_P^2 \dot{u}_w(z,t) \tag{2-21}$$

where f_H is the hydrodynamic load, $f_{H,D}$ the drag component of f_H, $f_{H,M}$ the inertia component of f_H, C_D the drag coefficient of the submerged structure, C_M the inertia coefficient of the submerged structure, ρ_{wat} the density of water and D_P the diameter of the submerged structure.

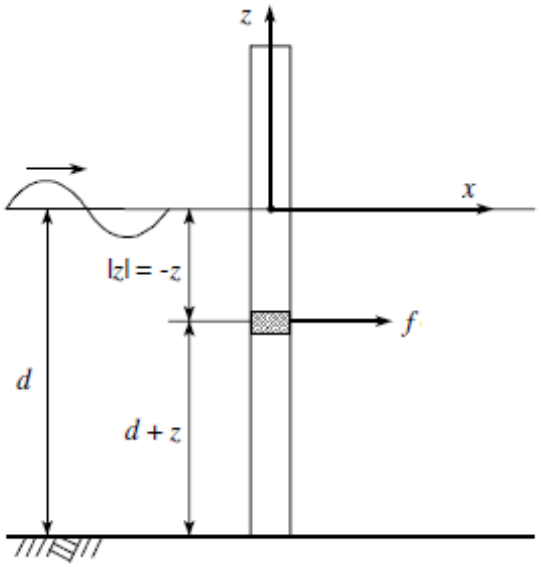

Figure 2-6: Combined drag and inertia hydrodynamic load on a bottom founded structure [49]

2-3 Soil

The discussion about wind and sea climate is here followed by the soil description. A seabed consists of several layers of soil with different properties. Focusing on the North Sea, the major types of soil are two: sand and clay (and to a lesser extent gravel)[3]. Geotechnical investigations, accompanied by laboratory testing of the specimen are the usual way from which developers can get an insight into the soil conditions. The most crucial properties for the follow-up structural calculations are listed below:

$\boldsymbol{\phi}$ **:** The external friction angle shows the friction between a soil medium and a material such as a retaining wall or pile. It is expressed in degrees and it is defined only for cohesionless soil types like sand.

$\boldsymbol{C_u}$ **:** The undrained shear strength is a property of soil that describes the shear stress that a soil can sustain. It is expressed in N/m^2 and is valid only for cohesive soil types such as clay.

$\boldsymbol{\gamma}$ **:** The submerged unit weight of a soil mass is the ratio of the submerged total weight of soil to the total volume of soil. It is expressed in N/m^3.

$\boldsymbol{N_q}$ **:** The bearing capacity factor is a dimensionless factor that is used in the calculation of the bearing capacity of the soil. It is defined only for sand.

$\boldsymbol{e50\%}$ **:** This property gives the strain in percentage for 50% of the maximum strength and is defined for clay as soil type.

$\boldsymbol{f_{lim}}$ **:** The limit unit skin friction is the friction resistance on the skin of a pile and given in kPa. It is defined for sand as soil type.

$\boldsymbol{q_{lim}}$ **:** The limit unit end bearing pressure is the resistance on the end of the pile and given in kPa. It is valid for sand as soil type.

2-4 General Fatigue Principles

Imperfections of the material in the forms of cracks and sharp edges result in locally high stresses and plastic deformations. Continuously varying stresses cause a gradual deterioration of the material, propagation of the cracks and ultimately failure. Fatigue is the phenomenon that the material, subjected to stresses that are globally lower than the yield limit, breaks after a certain number of cyclic loading. A depiction of this behaviour is provided by Fig. 2-7.

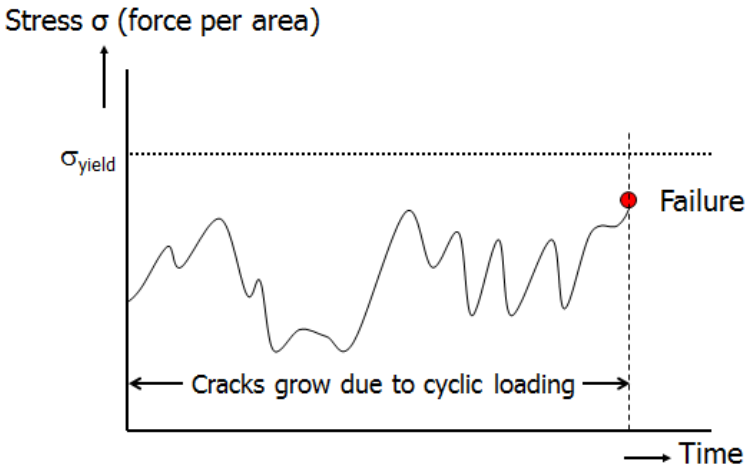

Figure 2-7: Failure at lower load than the maximum allowable [55]

S-N Curves

The S-N (or Wöhler) curve gives information regarding the number of load cycles that a material can withstand under a cyclic load with constant mean value and amplitude. Specimen are subjected to a wide range of loads and the cycles after which they fail for every different cyclic load form the Wöhler curve. The curve is given in its simplified version (assuming the term accounting for the thickness ratio t/t_{ref} to be 1) by the equation:

$$log_{10}(N) = log_{10}(\alpha) - mlog_{10}(\Delta\sigma) \tag{2-22}$$

where $\Delta\sigma$ is the stress range, N the number of stress cycles to failure at $\Delta\sigma$, $log_{10}\alpha$ the intercept of $log_{10}N$ axis and m the negative slope of S-N curve on $logN - logS$ plot.

The load range that is the limit below which the life of the material is theoretically infinity is called fatigue strength. This observation is a point to consider when constructing an S-N curve (in the forms of a "knee" in the curve). However, although very small load cycles may not be capable of starting cracks (this is what the previous sentence describes), they cause further propagation of existing cracks [47]. Therefore, a horizontal line starting from the intersection point, known as "Original Miner", is regarded as optimistic [47]. This would essentially mean that small load cycles would never cause a fatigue failure which contradicts to the statement regarding the propagation of the existing cracks. Similarly, the proposal of extending the right part of the curve with the same slope, called Elementary Miner or Corten-Dolan, is conservative and over simplistic [47]. An alternative approach is proposed by Haibach and since it is somewhere in between the two extremes it is considered to be appealing [47]. According to Haibach, the slope should be given as follows:

$$m_{right} = 2m_{left} - 1 \tag{2-23}$$

where m_{right} the negative slope at the right part of the curve and m_{left} at the left part of the curve.

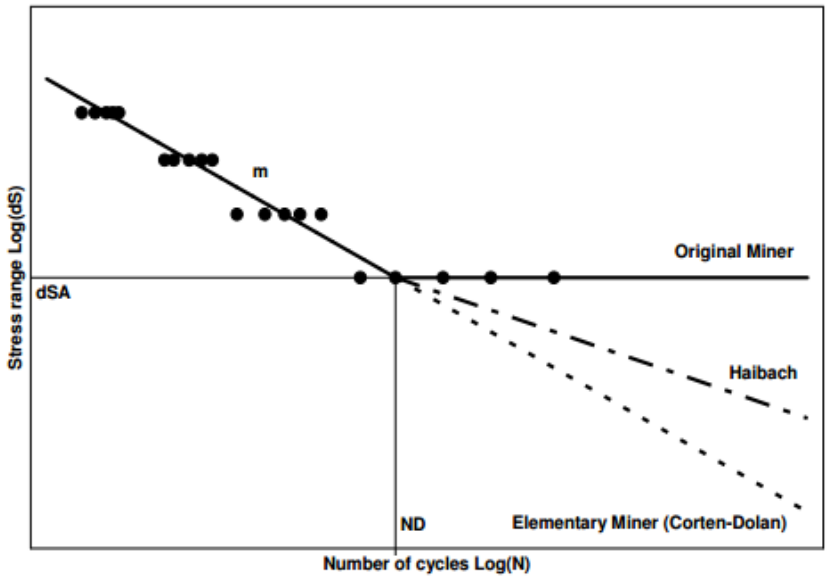

Figure 2-8: S-N curve and correction proposals beyond the point of fatigue strength [47]

Miner's sum

The fatigue damage can be described by the Miner's sum method. This method relies on the summation of the damage caused by each stress range in a stress history, or partial damage:

$$Damage = \sum_i \frac{n_i}{N_i} \tag{2-24}$$

where $Damage$ is the fatigue damage parameter, n_i the cycles present in a signal i with a particular stress range (or amplitude) and N_i the cycles to failure for this signal i.

Despite the limitations that this model introduces to the analysis, it is firmly stated that it has a fair accuracy and has therefore dominated these types of analysis[29]. Such limitations are the following: potential effects of load order are not taken into account and the value of the damage parameter only indicates whether there is failure or not, giving no insight into a physically quantifiable damage [29].

Equivalent Loads

The concept of equivalent load reduces a long history of random fatigue loads to one number. Thus, an easier and more efficient comparison of numerous load cases is feasible. This concept introduces a fatigue damage equivalent load (or stress) which represents the load (or stress) with this constant amplitude that if applied to a material would cause the same damage as the random fatigue load cases. The number of the cycles that are used to derive the equivalent load are predefined: either explicitly (typically 10^7) or implicitly by considering a constant frequency (typically $1Hz$) and a targeted lifetime as time period. The equivalent stress is calculated:

$$\Delta\sigma_{EQ} = \left(\frac{1}{N_{EQ}} \sum n_i \Delta\sigma_i^m \right)^{1/m} \tag{2-25}$$

where $\Delta\sigma_{EQ}$ is the equivalent load, N_{EQ} the equivalent cycles, $\Delta\sigma_i^m$ the fatigue load cases and n_i the cycles that correspond to each load case.

Chapter 3

Fatigue Parameters

Fatigue is the failure mode caused by continuously varying stresses that result in crack propagation on imperfect material areas. Without strong knowledge on the parameters that influence its structural integrity the estimation of whether a support structure reaches or not unaffected the intended design life is in dispute. The fast analysis favouring the early design phase is already by Chapter 1 concretely defined as the primary objective of the developed scheme. Having a strong insight on the mechanisms through which several parameters, hereafter called *fatigue parameters*, leave their impact on the structure can contribute towards the accomplishment of the objective. The present chapter provides this insight.

The major characteristic of the proposed methodology for quick FLS assessment and extrapolation by site variation models (Chapters 4 and 5) is a single structure design; therefore only the environmental conditions are regarded here as fatigue parameters. Otherwise, numerous design choices would be additionally considered as such parameters: for instance, a smaller pile diameter would reduce the hydrodynamic loads and potentially the fatigue.

The first step is to categorise the environmental conditions, as partly presented in Chapter 2, to conditions that affect loading and conditions that affect dynamic response of the structure. These are treated in Sections 3-1 and 3-2 respectively. What induces this distinction is the fact that the vibrations of a structure are attributed to the load that is caused by the fluctuating environmental conditions as well as its own dynamics. In addition, the analysis goes one level deeper to the identification of the way that these affect the loads or the stiffness. This step comprises hence the bridge between the conditions and their impact on structural integrity; in other words, between the excitation and the response. Ultimately, the goal of the dependency study in Section 3-3 is to group parameters depending on the similarity of the mechanisms, since a potential match of these bridges proves of valuable significance for the developed method.

3-1 Influence on Loads

The first category of the fatigue parameters are these that determine the loads exerted on the structure.

- Wind speed

  The mean wind speed may not give direct rise to fluctuating forces, its impact on fatigue loads is however captured indirectly in two ways: firstly, the dynamic component of the thrust is linearly dependent on it (as Section 4-2 later proves) and secondly, both Kaimal and von Karman turbulence models (presented in Section 2-1) are a function of the mean wind speed.

- Turbulence

  The deviation of the wind speed around a mean value (over a specified time period) causes thrust and drag variation. The turbulence (visualised in Fig. 3-1) is expressed by the standard deviation of the wind speed, therefore induces dynamic loads.

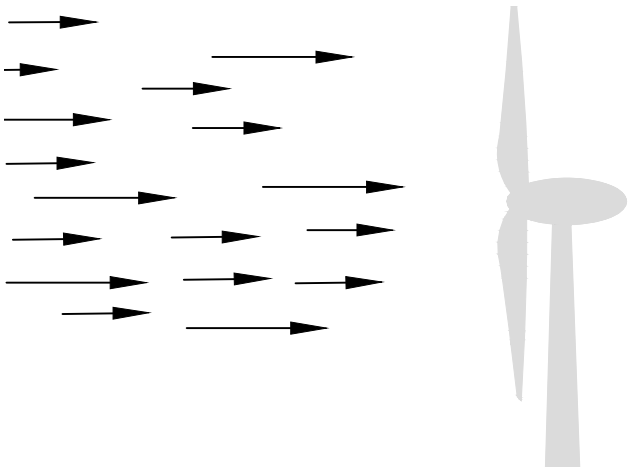

Figure 3-1: Longitudinal turbulence of the wind field approaching the wind turbine

- Wave height

  The wave height plays a tremendous role on the hydrodynamic load. To observe this, one has to look back at the equations giving the water particle velocity and acceleration in Section 2-2, where both terms are a function of it. The wave kinematics in turn determine the loads from the Morison equation, also given in Section 2-2.

- Wave period

  Similarly to the wave height, the wave (peak) period determines the water particle velocity and acceleration influencing the fluctuating hydrodynamic load by Morison equation. Assuming a fixed point (in x-axis) on the sea surface, its elevation is depicted in Fig. 3-2.

- Water depth

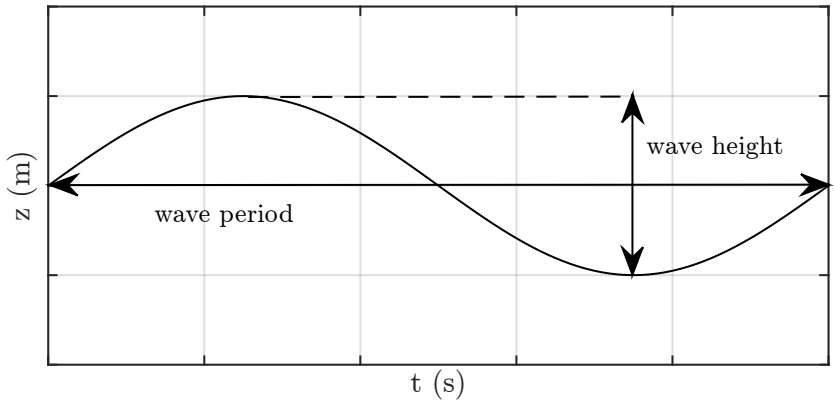

Figure 3-2: Elevation of a fixed point at the surface of the sea over time

The water depth is in principle the lever-arm over which the distributed loads are integrated for seabed load calculations. Obviously, the actual value of this property varies with time, however the mean sea level (MSL) is primarily addressed. Moreover, the water kinematics is affected by the water depth.

3-2 Influence on Stiffness

The approach of the previous section highlights the need for covering the dynamic behaviour of the system as well. Given the strong dependence of any structure's dynamics on the stiffness, the second category of investigated environmental conditions are those that affect the stiffness:

- Soil properties

  The soil provides a support structure with additional stiffness next to its elastic and geometric stiffness. The lateral stiffness (on which the analysis focuses) is usually modeled by non-linear horizontal springs distributed along the foundation pile as depicted in Fig. 3-3. The p-y curves characterise the stiffness of the soil springs, are function of the soil parameters and can be calculated for different piles and penetration depths [28]. Qualitative p-y curves with the typical pile deflection are also shown in Fig. 3-3.

- Scour

  The lowering of the seabed caused by the sediment transport has eventually a substantial consequence on the soil stiffness. More specifically, currents and waves stir and move seabed masses creating holes around the foundation piles of offshore structures. Thus, they reduce the supportive layers surrounding the pile at the seabed level, as Fig. 3-4 shows, leading to a more flexible structure.

- Water depth

  Regardless of the model applied to estimate the eigen-frequency of a support structure (e.g. effective fixity depth, distributed springs along the pile penetration, seabed coupled or uncoupled springs etc.), the water depth, as defined in Fig. 3-4, always has the same

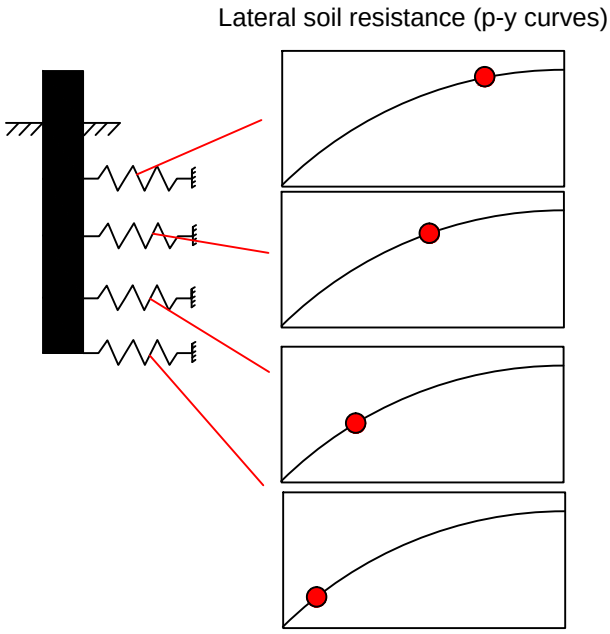

Figure 3-3: Typical p-y curves along the pile and pile deflection at different depths (red spots)

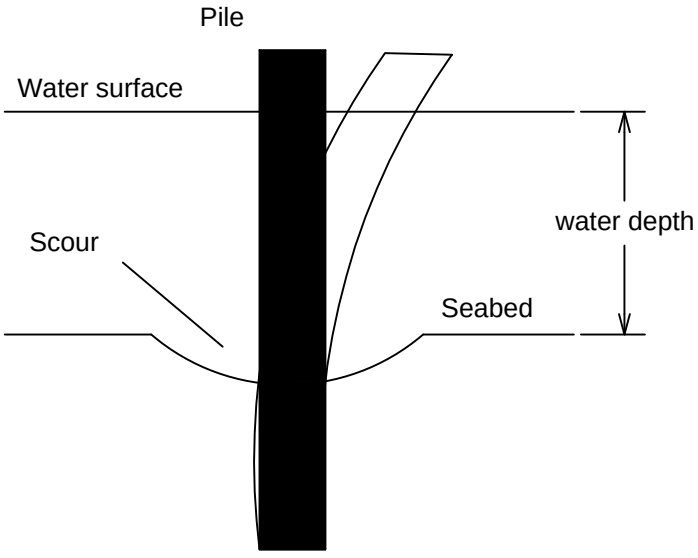

Figure 3-4: Complexity of several fatigue estimation models and relative comparison to the proposed methodology

apparent behaviour: deeper water implies longer, consequently more flexible beams, while shallower water implies shorter and stiffer structures.

3-3 Dependency Study and Grouping

A visualisation of the dependencies, provided by Fig. 3-5, can ease the identification of grouping possibilities to ultimately formulate the foundation blocks of the proposed methodology.

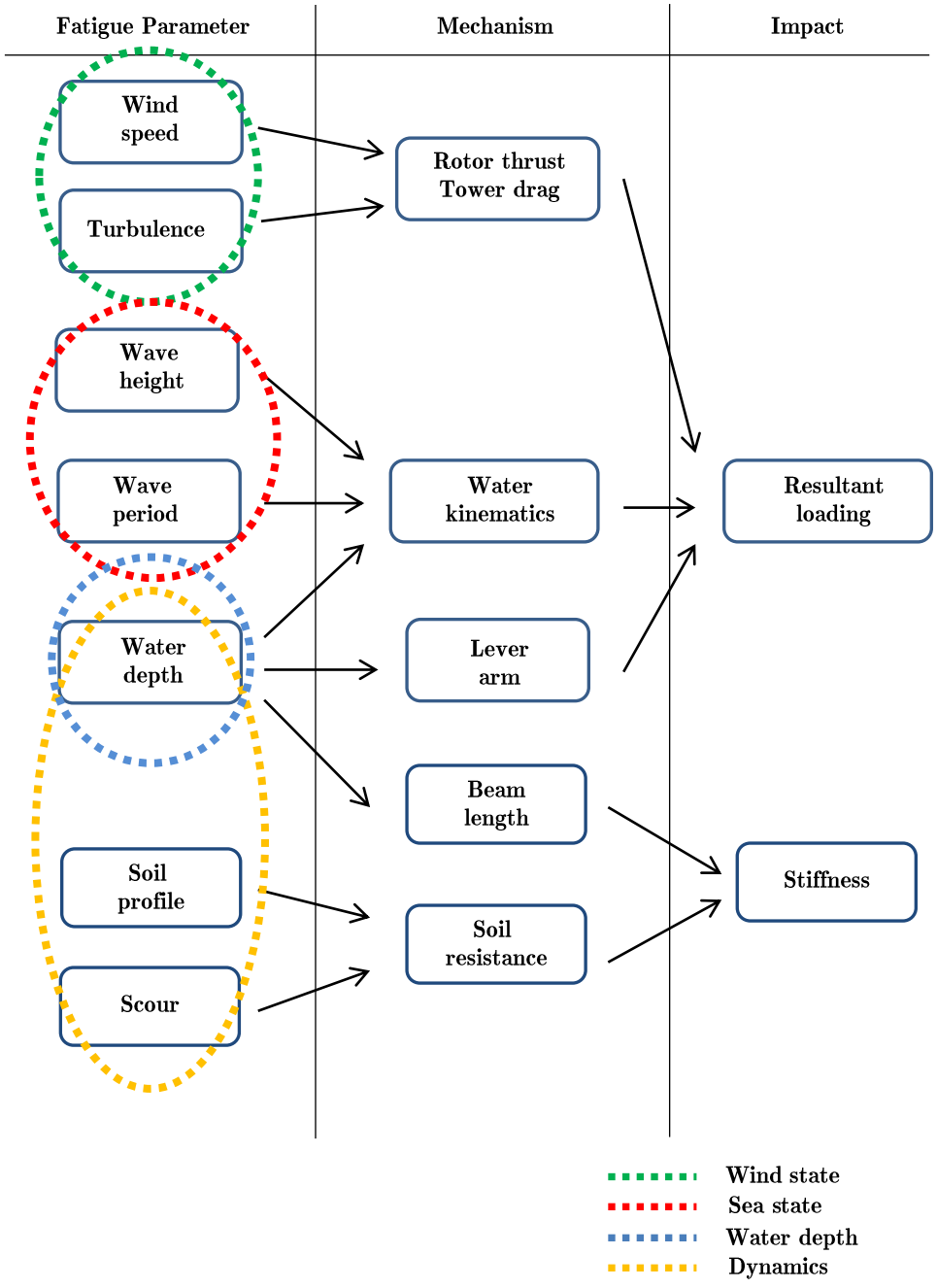

Figure 3-5: Dependency study between fatigue and fatigue parameters along with the parameter grouping used in the methodology presented in the next chapter

The grouping is performed such that parameters that cause fatigue damage through the same mechanisms are treated as a separate block. This prevents a global re-usage of the analysis when only certain fatigue parameters change from a reference location to the examined one. By looking at Fig. 3-5, it is clear that three such blocks can be observed:

- Block 1: Wind speed and turbulence
- Block 2: Wave height and wave period
- Block 3: Soil profile and scour

which are hereafter referred to as *Wind state*, *Sea state* and *Dynamics* respectively.

The water depth is undeniably a challenging parameter to group with others and forms itself Block 4 due to its dual role: it affects loads and stiffness. In fact, even the variety of the mechanisms through which it influences the resultant loading contradicts the aforementioned criterion of common mechanisms. Therefore, it is chosen to be treated separately as a distinct block. However, it should not be neglected that this parameter determines, along with soil properties and scour, also the stiffness by specifying the length of the beam representing the monopile, as Fig. 3-5 shows. This is the reason why *Dynamics* also has the *Water depth* incorporated besides the rest. The blocks are summarised in Fig. 3-6.

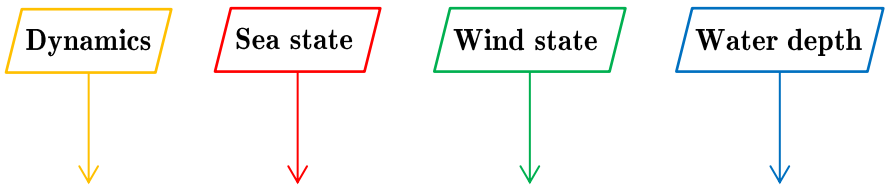

Figure 3-6: Starting blocks of the developed method for simplified fatigue assessment of different monopiles in the same farm

It is now feasible to assess each site variation on the basis of the above blocks. For a complete assessment the definition of all at the same time is apparently prerequisite, whilst for extrapolation to a different location within the farm only a number of them, saving thus time considerably (assuming that an analysis for the reference location is taken for granted). The latter reveals the motivation behind this dependency study which becomes fully clear and is further explained in Chapter 5. In that chapter, having presented the main scheme, site variability is evaluated taking advantage of the outcome of the present chapter.

Chapter 4

Proposed Methodology for FLS Estimations

The key requirement is to develop a methodology that estimates fatigue at different farm locations and is suitable for the early design phase (outlined in red in Fig. 1-1). The complexity of the scheme should therefore be a profoundly treated factor. The baseline on which FLS frameworks principally rely are the time- and frequency-domain. Both methods, however, are considered advanced and not in accordance with the aforementioned requirements. It could also be argued that since these are the mainstream methods for a detailed assessment, there would hardly be any benefit in terms of simplicity and speed if implemented for all site positions. In other words, such a proposal would imply multiple detailed assessments, ignoring thus the motivation: one detailed assessment followed by site variation-dependent extrapolation.

4-1 Framework Basis and Scheme Introduction

The introduction clarifies that an alternative approach is necessary. The frequency-domain is quicker than time-domain framework and it is quite often easier to obtain power spectral densities (PSD) than response time-series [16]. Therefore, in a scale with increasing complexity the time-domain is characterised as the rightmost method with the frequency-domain on its left-hand side. In addition to these, some first fatigue estimates can be derived by the system's linear response assumption and are given as [24]:

$$\begin{aligned} Damage &\propto \Delta\sigma^m \propto H_s^m \\ Damage &\propto n \propto \frac{1}{T_z} \\ Damage &\propto \Delta\sigma^m \propto \bar{U}^m \end{aligned} \tag{4-1}$$

Provided that these correlations neglect aspects of tremendous importance and therefore are regarded as over-simplistic, this approach is placed at the leftmost edge in the complexity

scale introduced earlier. In conclusion, the previous discussion results in the targeted position of the proposed scheme: in-between the frequency-domain and the correlations, as Fig. 4-1 shows.

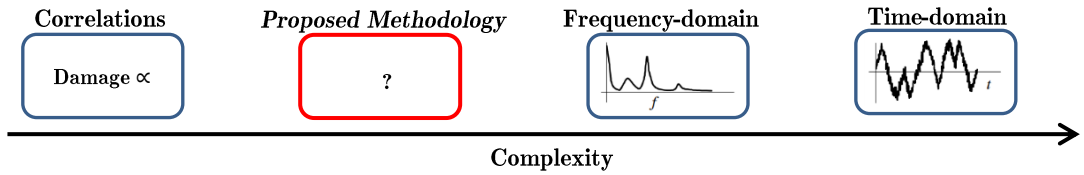

Figure 4-1: Complexity of common-practice FLS models and comparison to the proposed methodology

Having presented the basis of the analysis and the requirements that this analysis should fulfill, a framework is developed accordingly. The flow chart of Fig. 4-2 depicts the structure of the blocks that formulate the framework. The functions of the main stages, denoted in Fig. 4-2, are briefly discussed:

- **Stage 1** The parameters that implicitly determine fatigue by affecting the loading are specified. These lead to the excitation (e.g. wind and wave PSD) and the corresponding operational state.
- **Stage 2** The efficient prediction of the response of the system necessitates the implementation of an amplification factor that accounts for the dynamics.
- **Stage 3** By calculating the quasi-static response to the excitation and taking into consideration the dynamic effects, the overturning (fore-aft) moment PSD can be determined for different states.
- **Stage 4** The rotor in operational mode induces also harmonic loads which are here treated separately. An accurate prediction of these load ranges yields the damage over the lifetime by estimating the cycles for each range over this period.
- **Stage 5** Upon conversion of moment to stress PSD for the superposed wind and wave loads, the Dirlik method is applied for the generation of stress range histograms. Next, the fatigue damage is extracted by comparing the calculated stress ranges to the allowable ranges. In addition, the two terms of damage that are attributed to the cyclic loads (Stage 4) are added up.
- **Stage 6** Finally, the total damage and a predefined number of equivalent cycles result in the equivalent stress range or load.

Although the sequence of the steps might resemble a conventional frequency-domain assessment, it is appropriately adjusted to accomplish the goal of simplification. The rationality lies in the analytical nature of the method. This arguably fulfills any needs for auxiliary structural F.E. software, aeroelastic codes or time-consuming Fourier Transformations. The calculation of the moment spectra is a concept that has been recently highlighted by Arany, Bhattacharya, Macdonald and Hogan [2]. The developed framework here considers their method as starting point and with the necessary improvements and additions estimates quickly the resistance of

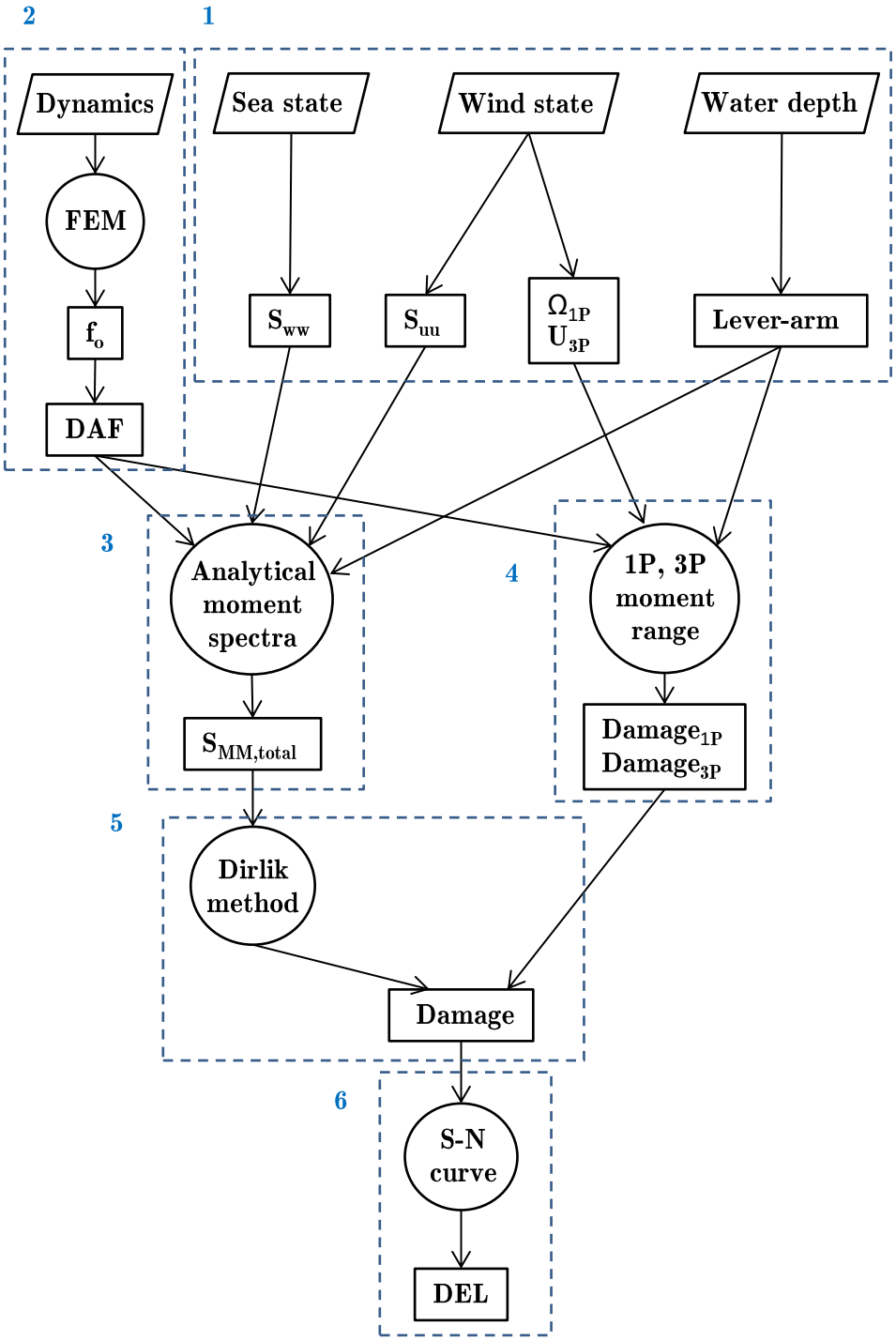

Figure 4-2: Proposed methodology for simplified FLS assessment

monopiles to fatigue failure. The major steps (illustrated in Fig. 4-3) that render the scheme a simplified version of the frequency-domain are:

- The identification of the dynamic load components for calculating the excitation

- The analytical calculation of the quasi-static response of the system
- The replacement of the Transfer Function (TRF) by a 1 degree-of-freedom (DOF) Dynamic Amplification Factor (DAF) for the dynamic response.

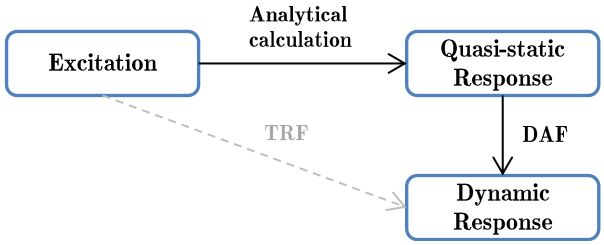

Figure 4-3: The by-pass of the TRF that would be essential for a conventionally calculated fatigue on the grounds of frequency-domain

Finally, the emphasis is here given on the fore-aft direction provided the substantially higher loads in the fore-aft direction compared to the side-to-side and secondly, their intense variation. Factors that result in these fluctuations are mainly the longitudinal component of the wind turbulence and the sinusoidal shape of the wave load. On the other hand, side-to-side variations originate from the blades' self-weight centrifugal forces, mass imbalances and potential wind-wave misalignment yet at a less intense pace.

4-2 Detailed Scheme Presentation

The brief introduction of the proposed methodology in the previous section is here followed by detailed elaboration on its working principles. All the following mathematical derivations and remarks explain the process in-depth.

4-2-1 Wind and Wave Spectra

The 1^{st} part of the analysis is the investigation of the response of the system to the experienced wind and wave spectra, the background information of which is given extensively in Chapter 2.

Wind Loads

As far as the wind loads are concerned, the Kaimal spectrum S_{Kaimal} is applied here in order to represent the spectral density of turbulent wind field S_{uu} (Fig. 4-4 and 4-5). Among the two spectra presented in Chapter 2, Kaimal and von Karman, the former is more suitable to model the atmospheric boundary layer, whereas the latter is more accurate for wind tunnel measurements [34]. This choice comes in agreement with the design codes that suggest either Kaimal or Mann (modified von Karman-type spectrum) [43].

The composition of the instantaneous wind speed of a static and a dynamic term results in a fluctuating component of the trust on the rotor T_{dyn}. Neglecting the term containing the dynamic wind speed squared u^2, T_{dyn} is given as:

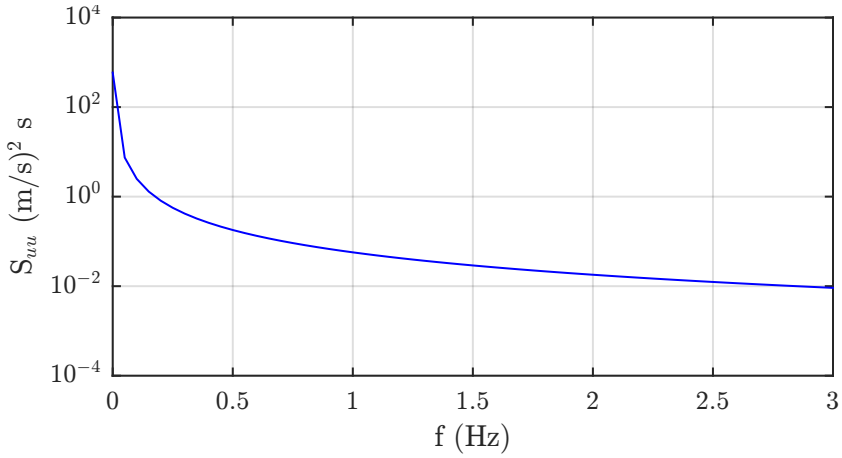

Figure 4-4: Kaimal spectrum for Normal Turbulence Model (NTM) at $\bar{U} = 8m/s$, $\sigma_u = 1.86m/s$, $TI = 0.23$ and $TI_{ref} = 0.16$

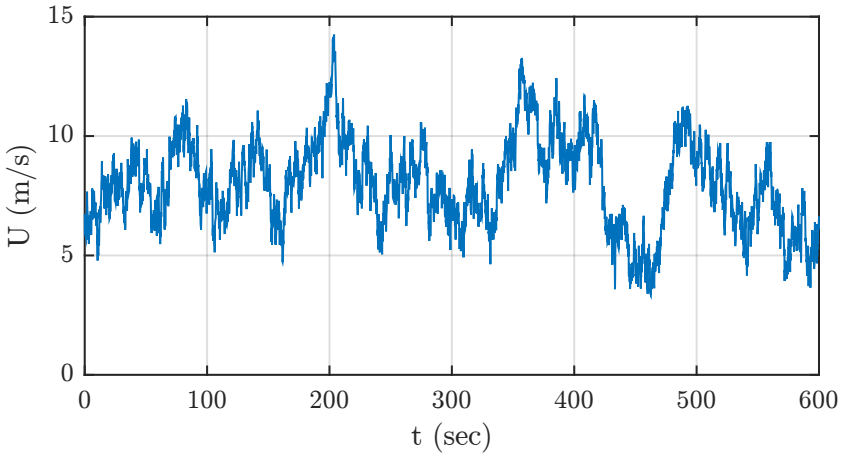

Figure 4-5: Instantaneous wind speed over a 10min period with the same turbulence parameters as in Fig. 4-4

$$T = C_T \frac{1}{2} \rho_{air} \pi \frac{D^2}{4} (\bar{U} + u)^2 = C_T \frac{1}{2} \rho_{air} \pi \frac{D^2}{4} (\bar{U}^2 + 2\bar{U}u) \tag{4-2}$$

$$T_{dyn} = C_T \rho_{air} \pi \frac{D^2}{4} \bar{U} u \tag{4-3}$$

This fluctuating term of the thrust can be converted to PSD of (mudline) moment exerted by the rotor thrust $S_{MM,wind,R}$ at water depth d and point of the thrust application (i.e. the hub height with respect to MSL) Z_{hub} and expressed as:

$$S_{MM,wind,R} = C_T^2 \rho_{air}^2 \pi^2 \frac{D^4}{16} \bar{U}^2 (Z_{hub} + d)^2 S_{uu} \tag{4-4}$$

Despite its fairly low contribution to the overturning moment (compared to the thrust), the tower drag is not excluded from the analysis. Unlike however the thrust, the tower drag is a distributed load along the tower making the derivation of its spectral density somewhat more complex because of the integration from the bottom of the tower ($z_1 = Z_{MSL}$) to the tower top ($z_2 = Z_{MSL} + Z_{hub}$). Applying the logarithmic profile to $\bar{U}(z)$ for the wind shear representation (see Chapter 2), the following equations give firstly the dynamic component of the tower drag (per unit length) $f_{T,dyn}$:

$$f_{T,dyn} = C_{D,T}\rho_{air}D_T\bar{U}u \tag{4-5}$$

the moment at the mudline $M_{T,dyn}$ associated with the wind speed fluctuations:

$$\begin{aligned} M_{T,dyn} &= \int_{z_1}^{z_2} C_{D,T}\rho_{air}\bar{D}_T\bar{U}(z)u\cdot(z+d)dz = \\ &= C_{D,T}\rho_{air}\bar{D}_T\frac{\bar{U}(Z_{hub})}{ln(Z_{hub}/z_o)}u\underbrace{\int_{z_1}^{z_2} ln(z/z_o)\cdot(z+d)dz}_{Q_1} \end{aligned} \tag{4-6}$$

and finally the PSD of this moment $S_{MM,wind,T}$:

$$S_{MM,wind,T} = C_{D,T}^2\rho_{air}^2\bar{D}_T^2\frac{\bar{U}^2(Z_{hub})}{ln^2(Z_{hub}/z_o)}Q_1^2S_{uu} \tag{4-7}$$

where the integral Q_1 is analytically calculated:

$$Q_1 = \left(\left(\frac{z^2}{2}+zd\right)ln\left(\frac{z}{z_0}\right)-\frac{z^2}{4}-zd\right)\Big|_{z_1}^{z_2} \tag{4-8}$$

Notes:

- Considering the significantly low contribution of the tower drag to the moment (particularly when wave loads are also taken into account), certain assumptions have been made. Besides taking the mean value of D_T as constant to simplify the integration, the substituted wind spectrum refers to the hub height. To be more specific, S_{uu} is defined by $\bar{U}$ which in this case corresponds to the height of Z_{hub}. Due to wind shear, nonetheless, this (mean) wind speed decreases as moving downwards from the hub to the sea level.
- The longitudinal turbulence scale parameter Λ_1 is a function of the height which in turn affects the integral length scale Λ_u and ultimately the spectral density of the wind [43]. This is here neglected and Z_{hub} is taken into account for all heights.

Having fully covered the load spectra with the wind as source, they can be easily superposed upon summation. $S_{MM,wind}$ represents the PSD of the mudline moment caused by aerodynamic loads and is found as:

$$S_{MM,wind} = S_{MM,wind,R} + S_{MM,wind,T} \tag{4-9}$$

Wave Loads

The wave-induced fatigue loads can be significant, therefore quite frequently govern the design particularly for monopiles [38]. Regarding the type of the spectrum S_{ww}, the JONSWAP spectrum S_{JS} is applied. As Chapter 2 explains, this version of Pierson-Moskowitz is specifically developed for fetch-limited seas and the North Sea is a typical example of such seas. The choice of the North Sea is justified by the fact that it is currently the area attracting the highest interest for offshore wind.

The most commonly used way of wave force calculation, Morison equation (as presented in Chapter 2), is also followed here. However, it is of great benefit in terms of simplification of the problem to neglect the drag term of the equation; this is a common practice when wave-induced fatigue loads are studied [46] [38] [2]. Fig. 4-6 shows the drag and inertia loading on a pile in the Egmond aan Zee wind farm (OWEZ) under a typical sea state. It verifies the statement about the inertia load being the governing term and thus strengthens the assumption. An additional indicator of whether the forces are drag- or inertia-dominated is the Kreulegan-Carpenter number which is defined by Eq. 4-10 [17]. Values of KC lower than 5 imply an inertia-dominated wave force. To provide a representative example, a substitution of the parameters that apply to OWEZ (the same as in Fig. 4-6) under a regular sea state results in $KC = 1.37$.

$$KC = \frac{u_{max} T_p}{D_P} = \frac{\pi H_s}{D_P} coth(kd) \tag{4-10}$$

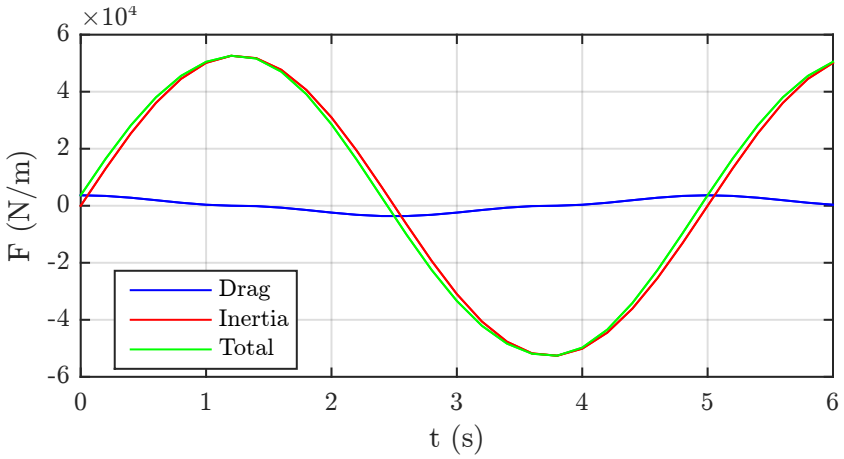

Figure 4-6: Wave loading at surface elevation for OWEZ farm: $D_P = 4.75m$, $d = 20m$ and a typical sea state: $H_s = 2m$ and $T_p = 6sec$

Given the above specifications and the background information provided in Chapter 2, the amplitude of the mudline moment $M_{H,max}$ due to wave forces can be firstly calculated by integrating from the mudline $z_1 = -d$ to the surface elevation z_2 ($z_2 = 0$ at MSL):

$$M_{H,max} = \int_{z_1}^{z_2} f_{H,M,max} \cdot (d+z)dz$$
$$= C_M \rho_{wat} \pi^3 \frac{D^2}{2} \frac{H_s}{T_p^2 sinh(kd)} \underbrace{\int_{z_1}^{z_2} cosh(k(d+z)) \cdot (d+z)dz}_{Q_2} \tag{4-11}$$

where:

$$D = \begin{cases} D_P, & for z < Z_{TP,bot} \\ D_{TP}, & for z \geq Z_{TP,bot} \end{cases} \tag{4-12}$$

and next, the substitution of the wave spectrum S_{ww} leads to the corresponding PSD of the moment at the mudline $S_{MM,wave}$:

$$S_{MM,wave} = C_M^2 \rho_{wat}^2 \pi^6 \frac{D_P^4}{4} \frac{f_p^4}{sinh^2(kd)} Q_2^2 S_{ww} \tag{4-13}$$

where the integral Q_2 is analytically calculated:

$$Q_2 = \left(\frac{(z+d)}{k} sinh(k(z+d)) - \frac{1}{k^2} cosh(k(z+d)) \right) \Big|_{z_1}^{z_2} \tag{4-14}$$

Notes:

- The wave number k is given by the general dispersion relation:

$$\frac{\lambda}{tanh(2\pi d/\lambda)} = \frac{gT_p^2}{2\pi} \tag{4-15}$$

  However, the assumption of deep water waves is made here for simplicity, therefore the dispersion relation reduces and yields the value of k as follows:

$$k = \frac{4\pi^2 f_p^2}{g} \tag{4-16}$$

- Airy theory, upon which the Morison equation is based, is valid only up to the still water level (SWL) [17]. Calculating loads up to the wave crest and not to SWL is possibly applicable mostly to ULS assessment, since it is only an instantaneous elevation. However, the upper limit of the integral of Eq. 4-11 is the crest elevation to make the problem more conservative. Among other options, such as linear extrapolation of wave velocity/acceleration and Wheeler stretching, the constant profile extension is here chosen to address this. An example of the method is seen in Fig. 4-7.

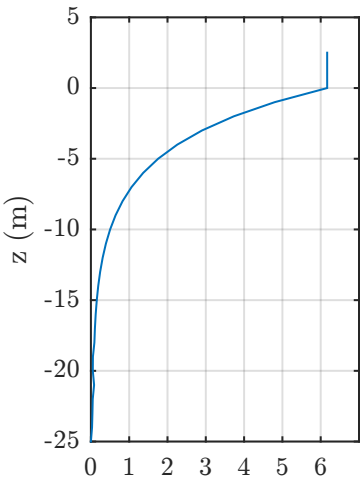

Figure 4-7: Extension of wave particle acceleration above SWL for a wave of $H_s = 5m$ and $T_p = 4s$ at depth $d = 20m$.

- Sharp geometry changes, such as boat landing systems or J-tubes are factors that affect drag and moment coefficients. The proposed formula for the correction of C_M (since the drag term is neglected) is given by Eq. 4-17. The corrected $C_M^{'}$ is assumed to be constant along the structure and over time (in reality this is not correct) and substitutes C_M in Eq. 4-13. Assuming a secondary steel diameter D_{SS}, the corrected value is given as [37]:

$$C_M^{'} = C_M \frac{D_P^2 + D_{SS}^2}{D_P^2} \tag{4-17}$$

- Large submerged structures might disturb the wave flow, a phenomenon known as diffraction and to address this the MacCamy-Fuchs correction is here incorporated [46]. This method expresses diffraction as reduced moment coefficient C_M and relates the reduction to the ratio of pile diameter over wave length as Fig. 4-8 depicts.

4-2-2 1P and 3P Excitation

Unlike static oil and gas top sides, offshore wind structures support a Rotor-Nacelle-Assembly (RNA) with heavy rotating components and machinery. These induce cyclic loads besides the direct response to the environmental excitation. The governing frequencies of the harmonic loading is the rotation of the rotor (1P), as well as the blade passing frequency (3P), i.e. three times the rotation of the rotor (for a 3-bladed turbine). The radical effect of these on the system's behaviour, particularly when resonance occurs, necessitates the modeling of the 1P- and 3P-induced fatigue loads. The notable difference of this approach from Section 4-2-1 lies on the absence of spectral densities and the derivation of moments for distinct frequencies instead.

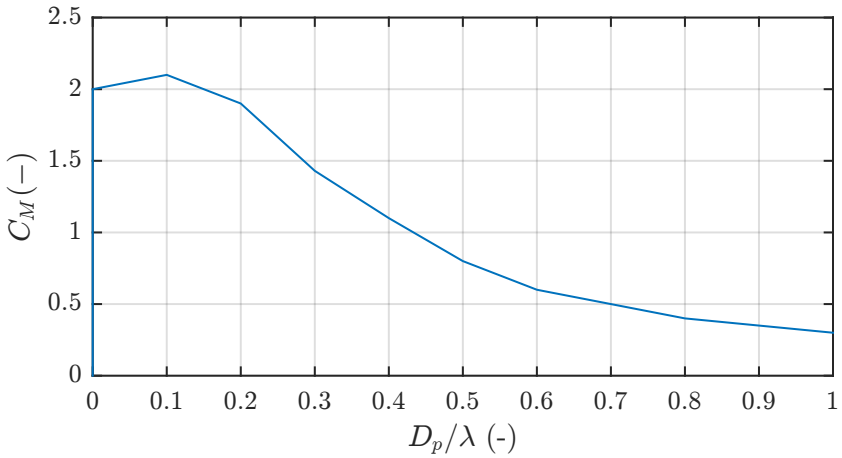

Figure 4-8: MacCamy-Fuchs correction accounting for diffraction occurring at large monopiles

1P Loads

The cyclic loads caused by the rotor at 1P frequency are attributed within the framework of this analysis to mass imbalance: a concentrated mass m_{1P} at a certain radial position R_{1P} on the blade representing manufacturing imperfections that result in differences in the blades. The rotation of the blade at Ω results in a centrifugal force F_{1P}, consequently a moment assuming rotor overhang b. This overturning moment M_{1P} at an azimuth angle θ is calculated as follows:

$$M_{1P}(\theta) = F_{1P}(\theta)b = (m_{1P}R_{1P}\Omega^2 cos\theta)b \tag{4-18}$$

while the range over one full rotation of the blade is, as Fig. 4-9 clearly shows,:

$$M_{1P} = 2m_{1P}R_{1P}\Omega^2 b \tag{4-19}$$

The Dirac function $\delta(f - f_{1P})$ could be applied so that this load is represented over the frequency range along with the previously derived spectra [2]. However, the infinity that $\delta(f - f_{1P})$ would reach at $f = f_{1P}$ would make the graph illegible. Alternatively, it is here treated as a separate/distinct fatigue factor. The state (defined by $\bar{U}$) specifies Ω, which in turn yields the load range $2m_{1P}R_{1P}\Omega^2 b$. Subsequently, 1P-induced fatigue can be estimated upon the translation of Ω into cycles over the lifetime given the occurrence per state.

3P Loads

Similarly to the mass imbalance for 1P varying response, the tower shadow is here modeled to represent the 3P cyclic load. The motivation behind the focus exclusively on the tower shadow and not on the wind shear for instance is that this is the most important deterministic load [4] [42]. This cyclic load source originates from the obstruction of a uniform wind flow caused by the tower. The tower shadow in a 3-bladed rotor is a load variation experienced at 3 times the frequency of the rotor, or in other words the blade-passing frequency and results in a fluctuation of the thrust.

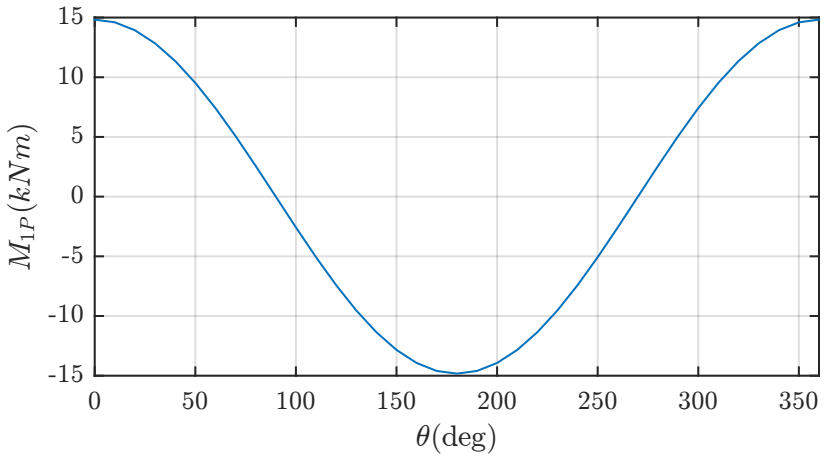

Figure 4-9: Overturning moment caused by 1P cyclic load over one rotation of the rotor, assuming $m_{1P}R_{1P} = 1900kgm$, $b = 5m$ and $\Omega = 1.25rad/s = 12RPM$

Focusing on the wind speed experienced by a single blade, however, it is evident that its fluctuation has the same frequency as the one of the rotor. The drop in the wind is a function of the overhang b, tower diameter D_T, a certain radial position r along the blade at an azimuth angle (for 1 blade) θ (for $\theta \geq 90deg$ or $\theta \leq 270deg$). It is estimated according to Eq. 4-20 [41]. The summation of the ambient wind speed and the (negative) drop gives the resultant velocity (disturbed by the tower shadow) U_{3P}. A comparison of the wind flow disturbance at different positions span-wise is provided by Fig. 4-10.

$$U_{tower}(r,\theta) = U(Z_{hub})\frac{(D_T/2)^2\,(r^2 sin^2\theta - b^2)}{(r^2 sin^2\theta + b^2)^2} \tag{4-20}$$

$$U_{3P} = U(Z_{hub}) + U_{tower} \tag{4-21}$$

The expression of the wind speed drop to load drop when the blades of a rotor encounter the tower disturbance is based on the following remarks:

- Although, as clearly noticeable in Fig. 4-10, the part of the blade in the vicinity of the hub is time-wise more prone to disturbed flow, the maximum drop is almost independent of the radial position.
- The fitted sinusoidal curve representing the load variation must have 1/3 times smaller period (i.e. 3 times the rotor frequency) regardless of the actual shape of the wind fluctuation illustrated in Fig. 4-10.
- The aggregation of these 3 (one for each blade) cyclic loads with 1/3 of the revolution as phase shift from each other results in a composed 3P signal with the same amplitude. In other words, the 3 signals do not cancel when aggregated.

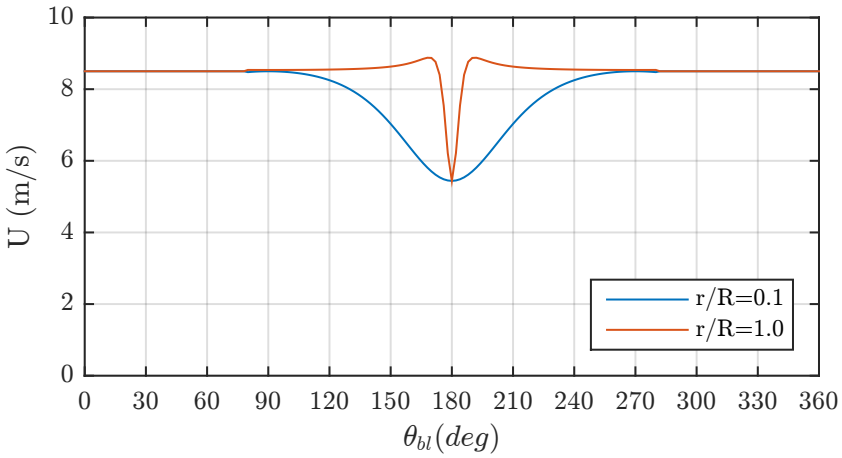

Figure 4-10: The velocity of the longitudinal (steady) wind flow of $U(Z_{hub}) = 8.5m/s$ disturbed by a tower with $D_T = 6m$ and a rotor overhang of $b = 5m$ (experienced by a radial blade position at 10% and at the blade tip)

On the grounds of these observations, namely with defined frequency and amplitude, the radial position does not affect the load variation. Therefore, it is valid to assume that this cyclic source can be rather accurately represented by the red curve in Fig. 4-11.

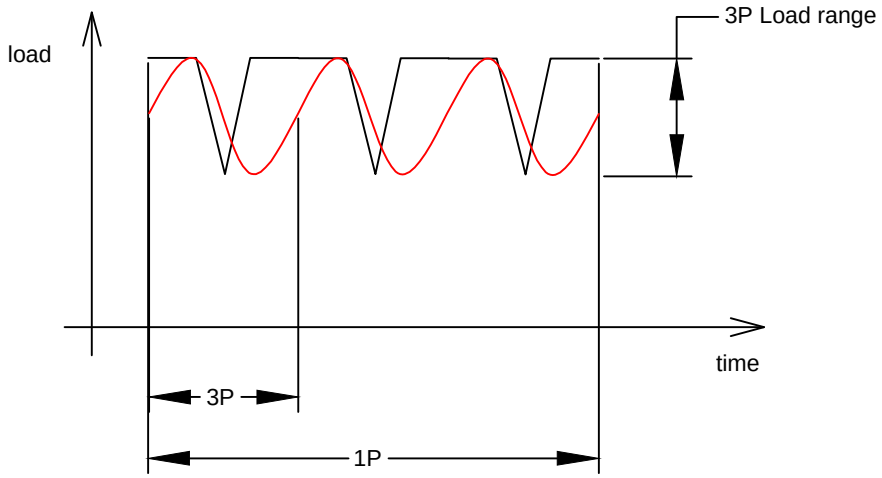

Figure 4-11: Assumption of sinusoidal thrust variation (red curve) to resemble a representative thrust variation (black curve) due to the effect of the tower shadow

This fatigue-inducing 3P moment range can now be approximated as the product of the thrust difference $T(U(Z_{hub})) - T(U_{3P})$ multiplied by the distance of the hub height from the mudline. At this point, the following question arises: how to calculate the reduced T for U_{3P} in terms of C_T? The answer is to assume constant induction Ua. Thereby, given $U(Z_{hub})$, U_{3P} and $a(Z_{hub})$, the new induction factor a_{3P} can be found and the new thrust coefficient $C_{T,3P}$ approximated by the wind turbine specifications input.

$$U(Z_{hub}) \cdot a(Z_{hub}) = U_{3P} \cdot a_{3P} \tag{4-22}$$

To summarise, the 3P moment range is regarded as a cyclic load with frequency of 3P and is approximated to be in magnitude:

$$M_{3P} = \left(C_T \frac{1}{2} \rho_{air} \frac{\pi D^2}{4} U^2 - C_{T,3P} \frac{1}{2} \rho_{air} \frac{\pi D^2}{4} U_{3P}^2 \right) (Z_{hub} + d) \tag{4-23}$$

4-2-3 Dynamics

The flexibility of the support structure gives rise to dynamic response. These dynamic effects are crucial especially when analysing long-term stress history and are here taken into consideration in the forms of the dynamic amplification factor DAF. It is defined as [10]:

$$DAF = \frac{1}{\sqrt{(1-\beta^2)^2 + (2\xi\beta)^2}} \tag{4-24}$$

where $\beta = f/f_o$, f_o is the 1^{st} natural frequency of the structure and ξ the damping ratio.

The damping ratio constitutes primarily the aerodynamic and to a lesser extent the structural and soil damping. The former originates from the counteracting outcome of the tower top motion and the instantaneous thrust: fore displacement results in higher wind speeds and thrust, while aft displacement results in lower wind speeds and thrust. This pattern acts as a damper. Several methods, like Garrad, numerical linearisation and non-linear simulation, are capable of providing the aerodynamic damping [46]. The structural damping is obviously associated with the damping in the structural material and specifically the inner friction. Given the recommended values (4-7% for aerodynamic, 0.5-1% for structural and 0.5-1.5% for soil), an overall estimate of 5% is a reasonable assumption [2].

In order to include DAF into the analysis, the quasi-static response spectra of wind and wave loads, $S_{MM,wind}$ and $S_{MM,wave}$, are superposed and multiplied by the corresponding DAF squared (the 1P and 3P moments are multiplied by the corresponding DAF but not squared):

$$S_{MM,total} = (S_{MM,wind} + S_{MM,wave}) DAF^2 \tag{4-25}$$

Having presented rigorously the most fundamental aspects of the proposed methodology, a graphical summary follows highlighting the dynamic amplification as well. Firstly, the wind and wave PSD (with and without DAF) are given in Fig. 4-12 for the conditions that are specified in the caption. Moreover, Fig. 4-13 and Fig. 4-14 illustrate the moment range caused by 1P and 3P cyclic loads (with and without DAF) for 5 representative wind states ($U = 4, 8, 12, 14, 18 m/s$ in this order).

The spectra in Fig. 4-12 point out the substantial amplification in the region of f_o both for wind and wave response. Additionally, the scenario of the wave peak frequency f_p being in the vicinity of f_o is here visually proven why it must be avoided. Eventually, the separate

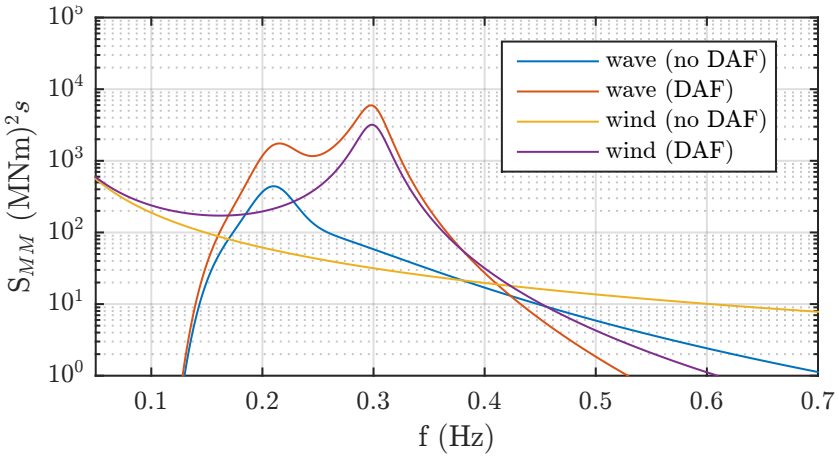

Figure 4-12: Overturning mudline moment spectral densities for wind- and wave-induced loads (with and without dynamic amplification); for a Vestas V90 on a support structure with $D_P = 6m$, $f_o = 0.31Hz$ and typical conditions $\bar{U} = 8.5m/s$, $H_s = 1.74m$ and $T_p = 4.76sec$.

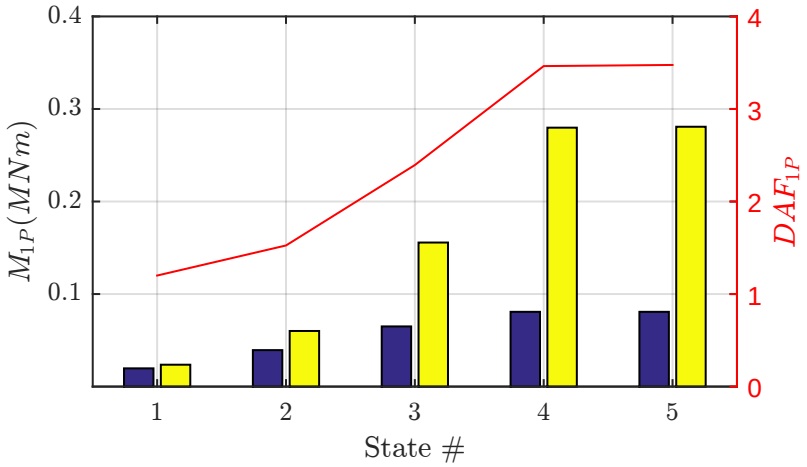

Figure 4-13: 1P excitation moment range at mudline with (yellow bars) and without (blue bars) dynamic amplification, along with the value of DAF (red curve); for a Vestas V90 on a support structure with $D_P = 6m$, $f_o = 0.31Hz$ and 5 states as defined in the main text

handling of 1P and 3P excitations justifies the absence of the corresponding peaks; that would be visible in any similar PSD graph conventionally generated by FFT in a response time-series.

With respect to Fig. 4-13 and 4-14, notable observations can be made for 1P and 3P response accordingly. These bins show that higher wind speed implies increasing Ω, therefore higher M_{1P} (see Eq. 4-18). Beyond the rated wind speed, though, Ω has reached the maximum value keeping M_{1P} constant as well. DAF increases in this case given that $\Omega_{max} \approx 2.9rad/s \approx 0.27Hz$ is the closest value to $f_o = 0.31Hz$. As for the 3P response, the non-amplified M_{3P} resembles as presumed the thrust curve (i.e. peaking at the rated wind speed). Unlike 1P amplification however, the gradual shifting of the blade-passing frequency 3Ω to frequencies higher ($\approx 0.80Hz$)than the eigen-frequency f_o induces a significant damping to high wind

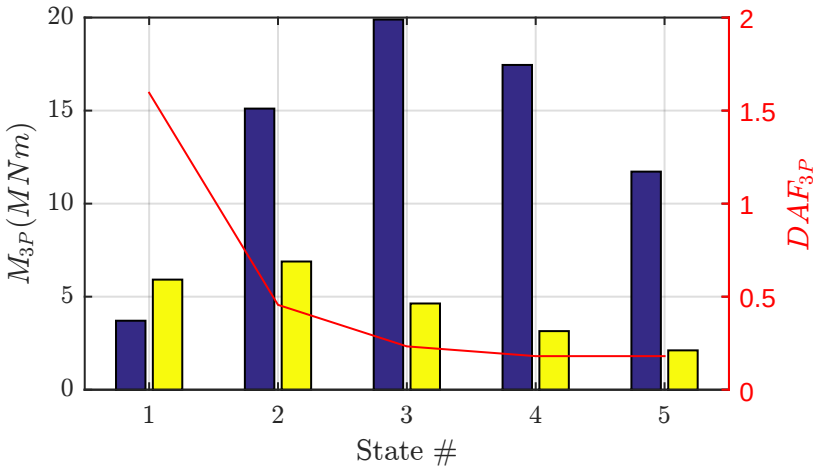

Figure 4-14: 3P excitation moment range at mudline with (yellow bars) and without (blue bars) dynamic amplification, along with the value of DAF (red curve); for the same turbine, support structure and states as in Fig. 4-13

speed states. Despite this damping though, M_{3P} seems way more damaging than M_{1P}.

4-2-4 Additional Specifications

Although the most crucial aspects that specify the framework are by now presented, there are parts in the methodology worth highlighting. These are discussed in this section. Such parts are blocks of the flow chart (Fig. 4-2) that are untreated yet, e.g. FEM model and Dirlik method, as well as additional incorporated options that target to improve the analysis.

FEM model

The calculation of the natural frequency is performed by an Euler-Bernoulli theory-based finite element model. Along with Timoshenko theory, they are widely implemented for beams [26] . The model is not presented in-depth in the present report since it is developed within the framework of another project of TU Delft's Wind Energy group but further details on this work can be found [32]. The foundation is modeled by p-y curves along the penetrated pile, the approach with the highest accuracy compared to uncoupled springs, effective fixity depth and others [53]. The structure as depicted in Fig. 4-15 consists of n nodes and $n-1$ cylindrical (up to the platform) or conical (along the tower) elements with the turbine mass on the top node. Elements matrices of mass $[M_e]$, elastic stiffness $[K_e]$, geometrical stiffness $[K_g]$ and soil stiffness $[K_s]$ assemble the global system's mass and stiffness matrices $[M]$ and$[K]$. Implementing a harmonic solution $\{\psi\}\, sin(\omega t)$ to the equation of motion of the global system:

$$([K] - \omega^2 [M])\{\psi\} = 0 \tag{4-26}$$

and solving it as an eigenvalue problem, $f_o = \omega/(2\pi)$ represents the vector that contains the natural frequencies.

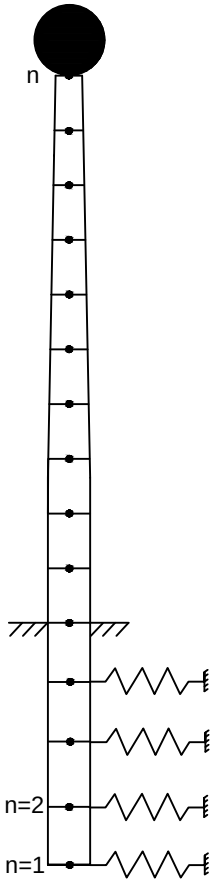

Figure 4-15: Finite Element model for the natural frequency calculation

In Fig. 4-16 a comparison is illustrated between the frequencies calculated by the model above and those derived with ANSYS. A matching that is not perfect yet with sufficient accuracy is indicated. After all, the conservatism that the applied FEM model yields is acceptable.

Scour

The scour development over the lifetime involves thorough investigations, therefore the scour depth is a parameter to take into consideration. The lowering of the seabed has as consequence the absence of the soil stiffness matrices for the upper layers, namely from the scour depth L_S up to the mudline. The stiffness of the structure, consequently the eigen-frequency, in this case drops with not negligible impact on the fatigue resistance. The influence of L_S on f_o is depicted in Fig. 4-17.

Load factors

To ensure the integrity of the structure by facing any uncertainties of the calculation procedures, certain load factors γ are applied. Like DAF, the superposed PSD are multiplied by these factors squared:

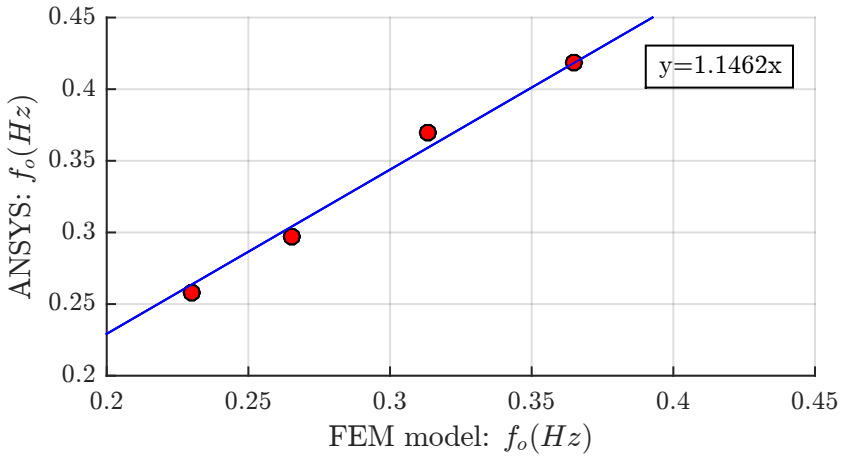

Figure 4-16: Comparison between the estimated system's natural frequency and the one calculated by advanced modeling in ANSYS

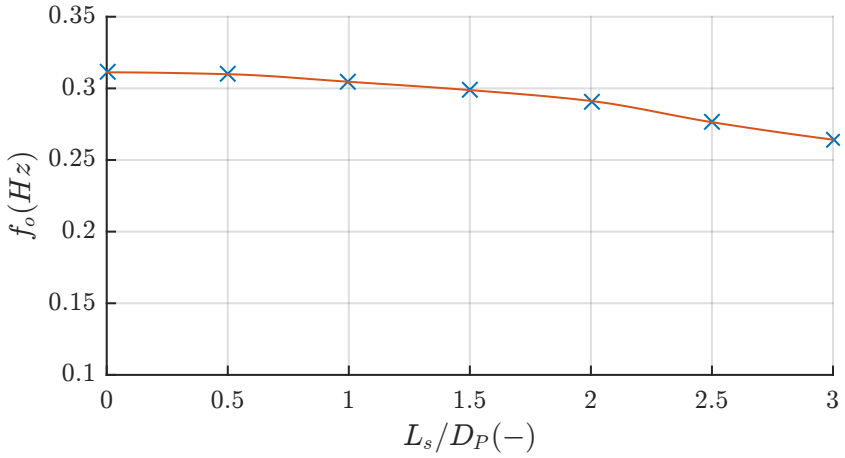

Figure 4-17: Drop of the natural frequency ($D_P = 4.7m$) with increasing ratios of scour depths over pile diameter

$$S_{MM,total} = (S_{MM,wind} + S_{MM,wave})\gamma^2 \tag{4-27}$$

Stress spectrum

Up to now, only moment PSD have been treated. It is acknowledged that the fatigue assessment is a process that is more convenient to be performed in terms of stress instead of load range. Therefore, the spectral density of the mudline moment (or at any other elevation as explained later) is converted to stress PSD. Given the geometry of the structure, namely the moment of inertia I of the cross-section of interest and the (outer) radius R, the stress range spectrum $S_{\Delta\sigma}$ is calculated as Eq. 4-28 shows. The emphasis on the fore-aft loading effectively specifies the location of the stress check point in the cross-section as depicted in Fig. 4-18

$$S_{\Delta\sigma} = \frac{S_{MM,total}}{I^2} R^2 = S_{\Delta\sigma,nominal} \tag{4-28}$$

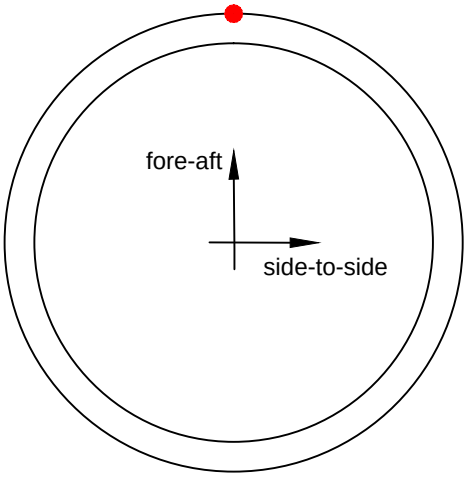

Figure 4-18: The point on the circumference where the stresses are calculated

As one can easily observe, the stresses are solely defined by the overturning moment. This is correct to assume since the stresses caused by the vertical compressive force might be high yet hardly fluctuating since they are attributed to the structure's self-weight. This is what the equation below explains assuming a PSD of the vertical forces S_{Fz} acting on the annulus of Fig. 4-18 with area A:

$$S_{\Delta\sigma} = \frac{S_{MM,total}}{I^2} R^2 + \cancelto{0}{\frac{S_{Fz}}{A^2}} \tag{4-29}$$

Stress Concentration Factors

The geometrical discontinuities on every structure require a careful analysis of the stress peaks which are quite higher than the nominal stresses [49]. The locally increased stresses are accounted here as well. In the present methodology, stress concentration factors SCF can be applied: having been defined, SCF are squared and then multiplied by the (nominal) stress spectrum $S_{\Delta\sigma,nominal}$ (or $S_{\Delta\sigma}$ as introduced above) in order to calculate the local spectrum $S_{\Delta\sigma,local}$. It is needless to add that the 1P and 3P stress ranges $\Delta\sigma_{1P}$ and $\Delta\sigma_{3P}$ are derived in the same manner:

$$S_{\Delta\sigma,local} = SCF^2 \cdot S_{\Delta\sigma,nominal} \tag{4-30}$$

$$\Delta\sigma_{1P} = SCF \cdot \frac{M_{1P}}{I} R \tag{4-31}$$

$$\Delta\sigma_{3P} = SCF \cdot \frac{M_{3P}}{I} R \tag{4-32}$$

S-N curve

The S-N curve is defined in accordance with the standards [10] [25]. Section 2-4 raises the issue of different proposals beyond the fatigue strength (or "knee") and concludes that Haibach method, "or Type B", is more suitable than Corten-Dolan or Original Miner. The parameter that needs to be defined for the simulations and specifies the S-N curve characteristic values, e.g. $log_{10}\alpha$, m, "knee" position, is the environment: whether in air, seawater with anti-corrosive protection, or seawater without corrosion protection [10].

Dirlik method

Of the three methods (Rayleigh, Rice, Dirlik) available to create stress range histograms out of stress spectra, the Dirlik solution is here applied; this comes in agreement with all relevant frequency-domain approaches [52] [35] [46] . The key reason is Rayleigh's tendency towards conservatism for offshore wind wide band stress spectra. The pattern works as follows: the stress spectrum is processed such that stress range probability density and distribution graphs are created, which finally yield the cumulative fatigue damage. A representative distribution of Dirlik's and Rayleigh's probability density functions can be seen in Fig. 4-19, where the over-prediction of the latter is clearly visible due to the corresponding curve being shifted to higher stress ranges.

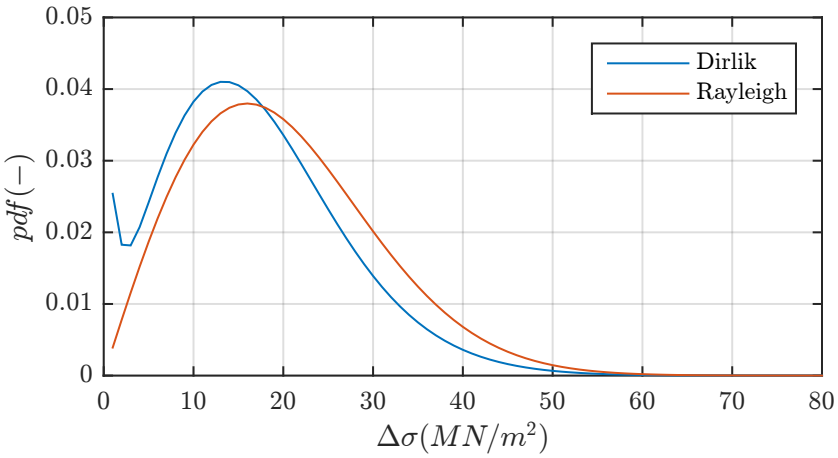

Figure 4-19: Probability density function applying Dirlik and Rayleigh method derived by a typical stress range PSD

Different elevations

Although the previous sections focus exclusively on the mudline, the scheme is developed such that it is capable of deriving response PSD at any elevation point. In order to satisfy this requirement, the integrals are adjusted accordingly and there is also a clear distinction between elevations above the MSL and submerged elevations. Fig. 4-20 depicts the PSD of moment caused by wind and wave at different elevations z.

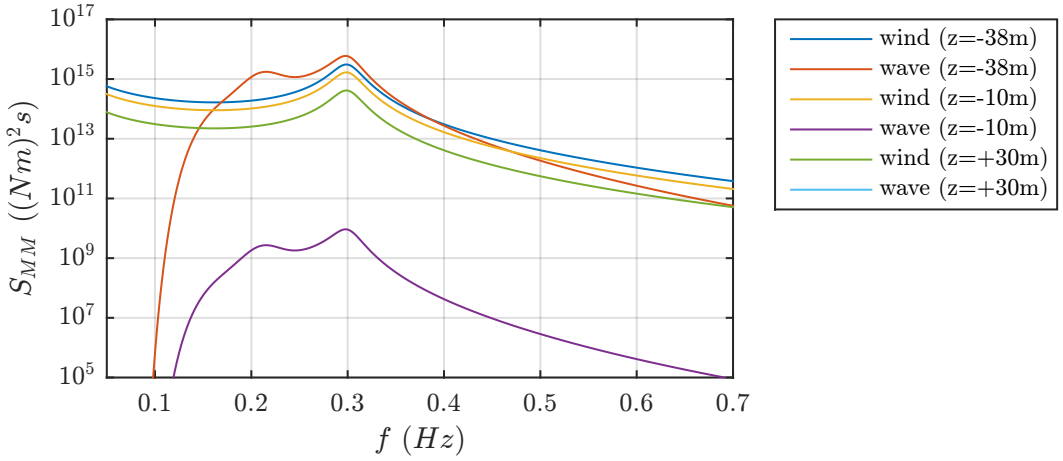

Figure 4-20: Overturning mudline moment PSD for wind- and wave-induced loads (with dynamic amplification); for a support structure with $D_P = 6m$, $f_o = 0.31Hz$ and typical conditions $\bar{U} = 8.5m/s$, $H_s = 1.74m$ and $T_p = 4.76sec$.

A comparison between the wind- and wave- induced moment spectra at different elevation, as illustrated in Fig. 4-20, depicts their variation along the support structure. Assuming the same monopile and the same conditions as in Fig. 4-12, one can see the significant shift of the wave spectrum downwards close to the sea surface elevation ($z = -10m$) compared to the mudline ($z = -38m$). At $z = +30m$ it is assumed that there is no wave-excitation, hence no response spectrum. Unlike wave, the moment PSD caused by the wind decreases only slightly at higher elevations. The less intense decrease originates from the fact that wind-induced loads are dominated by T_{dyn} (which exerts moment at any elevation) while the distributed $F_{T,dyn}$ contributes far less.

4-3 Limitations

The simplified nature of the presented scheme, aiming in this way at a quick yet as accurate as possible fatigue estimation is inevitably accompanied by certain tool limitations:

- The wave load does not give rise to moments above the sea level in the way the model is developed. However, in such complex systems the sea state affects the tower loads besides structural damping. This propagation, that would be captured by the TRF in the conventional frequency-domain, is neglected here. The necessity for the simplification of the method though has this unexamined behaviour as inevitable consequence.

- The wind-wave misalignment is not accounted for. Uni-directionality might on the one hand be conservative (therefore to some extent favourable), but on the other hand the damping is lower for any direction other than along-wind. Effectively, the side-to-side loads under misalignment would have an impact on the fatigue damage and move the point in the circumference where the maximum stress is expected to occur (Fig. 4-18).

- The 1-DOF approach on dynamics examines only the resonance at the 1^{st} nat. frequency. Similarly to the first remark, the higher eigen-frequencies would be incorporated if the TRF were not replaced by DAF. Nonetheless, it is not seen as a crucial limitation, since these frequencies do not amplify as intensely as the 1^{st} does.

- A restriction of the 1P and 3P excitation to mass imbalance and tower shadow respectively ignores others, such as aerodynamic imbalance, yaw misalignment, wind shear etc. Although the modeling of all would be ideal for the sake of completeness, the choice is made such that only the determining ones are included, as stated in Section 4-2-2 for the wind shear.

- The environmental states are lumped load cases. The distinction between operating- and non operating-modes excludes the transient start-ups and shut-downs which can be addressed only in the time-domain.

4-4 Validation

In order to confirm that this analytical scheme is suitable for its intended use, it is benchmarked with the time-domain software Bladed. For this validation the support structure used in the Dutch OWF Egmond aan Zee (OWEZ) is studied. With a mean water depth of $20m$, a tidal range of $3.8m$ and a scour depth of $8.5m$ (slightly deeper than what the design standards suggest [10]), a monopile with the geometry as defined in Fig. 4-21 is installed. As for the turbine, a Vestas V90 [1] is mounted onto the towers of OWEZ with the gross properties given in Table 4-1. Regarding the environmental conditions, described in Table 4-2, the fatigue bins are retrieved lumped and no post-processing of collected data is required except for adding longitudinal turbulence TI for the normal turbulence model (NTM) [46]. Due to lack of sufficient data for the soil profile, the assumption of only sand layers with $\phi = 35deg$ and $\gamma = 10kN/m^3$ is made [14]. Finally, a load factor $\gamma_L = 1.35$ and a material factor $\gamma_m = 1.1$ are applied to the load calculations [10].

Table 4-1: Gross properties of Vestas V90

Turbine: Vestas V90	
P_R	3,000 kW
D	90 m
U_{cut-in}/ U_R/$U_{cut-out}$	4 / 15 / 25 m/s
Ω	8.6 -16.1 (18.4)RPM
m_{top}	111,000 kg
m_{1P}	70 kg
R_{1P}	30 m

The main indicator of the reliability is the fatigue damage (the failure factor derived by Miner's rule). The proposed methodology (PM) performs rather effectively in contrast to the time-domain (TD) analysis as Table 4-3 clearly shows; fatigue damage of 1.006 and 0.979

[1] The turbine model used in the time-domain assessment is developed to approximate the performance of a Vestas V90 and is not provided by Vestas.

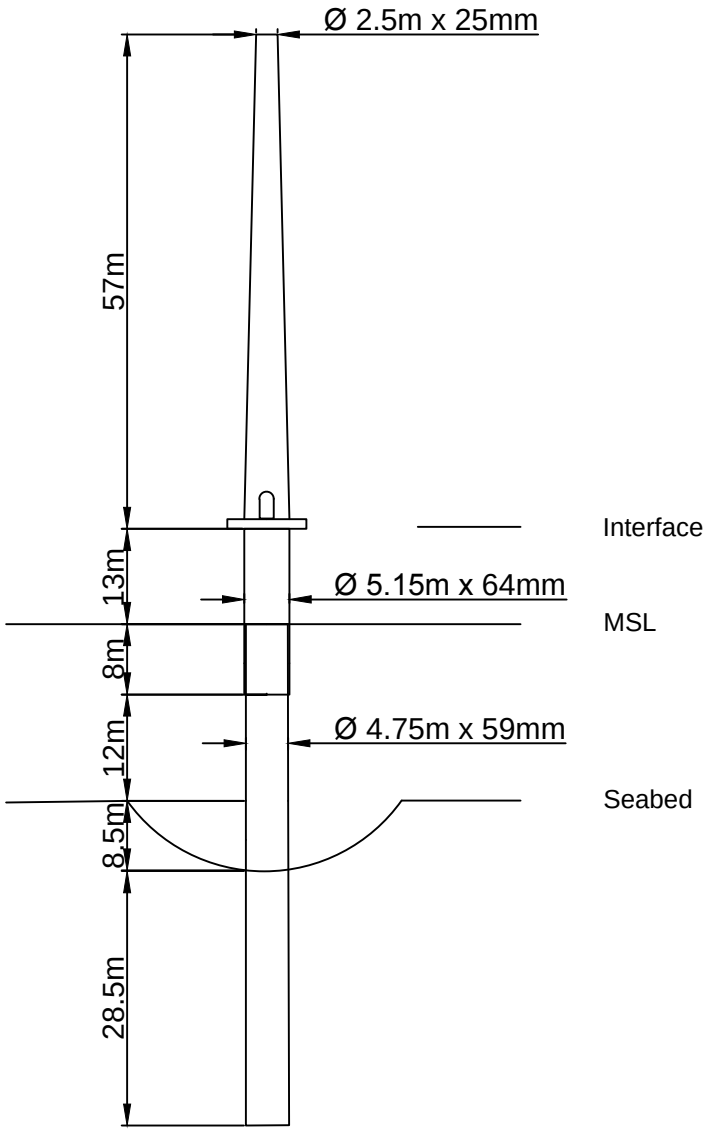

Figure 4-21: Approximated geometry of the support structure installed in OWEZ

respectively. The impressively low error of about 3% is considered negligible from an engineering point of view especially for the early design phase that this scheme is intended to be used. The independence from advanced numerical software and particularly the short simulation time are factors that provide additional arguments to use this methodology. Concerning the equivalent loads, an even lower error is expected provided the fact that $Damage$ is very sensitive to damage equivalent loads DEL (or equvalent stresses $\Delta\sigma_{EQ}$) due to the exponent m, the inverse slope of the S-N curve (Eq. 2-25). However, regardless of the overwhelming matching, one should think of the results critically to avoid deceiving conclusions. The following figures trigger the discussion on the above while Appendix A contains some additional graphs.

Several valuable conclusions about the performance of the developed FLS scheme can be

Table 4-2: Lumped environmental states for the OWF Egmond aan Zee (OWEZ)

Environmental states at OWEZ					
State	$U(m/s)$	$TI(\%)$	$H_s(m)$	$T_P(s)$	Occurence (%)
1	4	25.8	0.5	3	3.95
2	4	25.8	0.5	4	3.21
3	6	20.8	0.5	3	11.16
4	6	20.8	0.5	4	7.22
5	8	17.4	0.5	3	11.44
6	8	17.4	1.0	4	8.68
7	10	15.7	0.5	3	5.31
8	10	15.7	1.0	4	11.32
9	12	14.6	1.0	4	5.85
10	12	14.6	1.5	4	6.00
11	14	13.8	1.5	4	4.48
12	14	13.8	2.0	5	3.26
13	16	13.2	2.0	4	1.79
14	16	13.2	2.5	5	3.10
15	18	12.7	2.5	5	1.74
16	18	12.7	3.0	5	0.80
17	20	12.4	2.5	5	0.43
18	20	12.4	3.0	5	1.14
19	22	12.1	3.0	5	3.95
20	22	12.1	4.0	6	2.93
21	24	11.8	3.5	5	1.52
22	24	11.8	4.0	6	0.10

Table 4-3: Comparison of lifetime $Damage$, $\Delta\sigma_{EQ}$ and DEL between fatigue assessment by time-domain Bladed (TD) and the developed scheme (PM)

Fatigue analysis in OWEZ structure			
	TD	PM	Error (%)
$Damage(20y)$	0.979	1.006	2.76
$\Delta\sigma_{EQ}$ (MPa)	61.32	61.52	0.33
DEL (MNm)	40.49	40.63	0.33

drawn by a profound look at the environmental states. The lifetime weighted DEL, given in Fig. 4-22, reveal differences between the two analyses that are not visible in the first place when one focuses solely on fatigue $Damage$. More specifically, they show a general tendency for PM to over-estimate the damaging character of the partial load fatigue bins implying over-calculation of wind loads that generally peak at and thus dominate this region. The conclusion that wave loads do not cause this over-prediction is extracted by the fact that the sea states occurring at the partial-load area are very mild, therefore not state governing. On the contrary, PM under-predicts DEL (yet with somewhat higher accuracy) for the full-load right-most states of Fig. 4-22, namely with lower wind and governing wave loads. Coincidentally, wind over- and wave-under predictions compensate ideally for each other leading to the elusively low errors provided in Table 4-3.

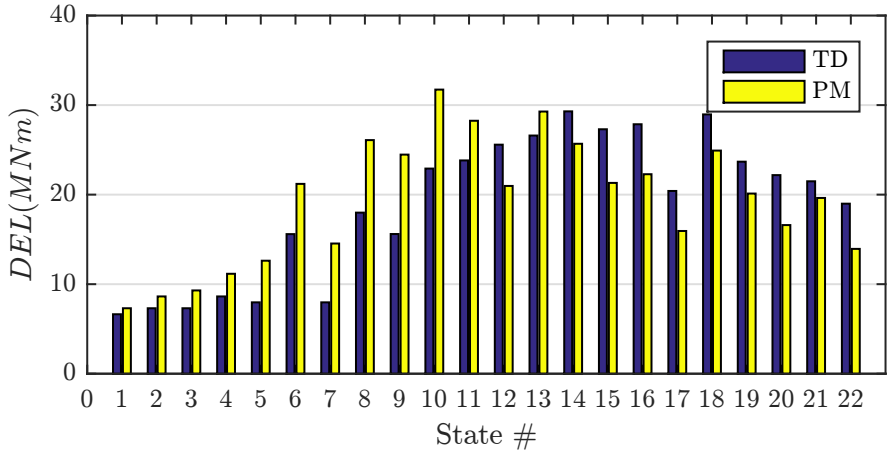

Figure 4-22: Lifetime weighted (unfactored) damage equivalent loads DEL of all fatigue bins for time-domain (TM) framework and the proposed methodology (PM)

By performing Fast Fourier Transformation (FFT) to the time-series produced by Bladed, the PSD from TD are illustrated in Fig. 4-23 along with those of the PM. An appropriate selection of bins to be depicted are a mild (state 1), a moderate (state 10) and a severe (state 21) wind/sea state to cover a broad range of environmental conditions. The spectra here visualise over a frequency range the remarks made previously with respect to Fig. 4-22. In all 3 bins the response to wind (occurring at very low frequencies) is over-predicted. This difference has high impact at bin 1 and 10 due to the mildness of the sea state, hence not being able to cancel the over-estimation. In states above rated wind speed (here bin 21) however, not only is the sea state critical, therefore governs DEL, but also the wind loads drop significantly and their over-prediction is no more visible in DEL of Fig. 4-22. In fact, the wave-induced load peak of PM (at about $0.2Hz$) is slightly lower than that of TD and this is where the slight DEL under-prediction of the right-most states originates from. It should also be highlighted that any 1P or 3P excitation responses present in TD cannot be observed in PM because of the separate analysis that these are imposed to.

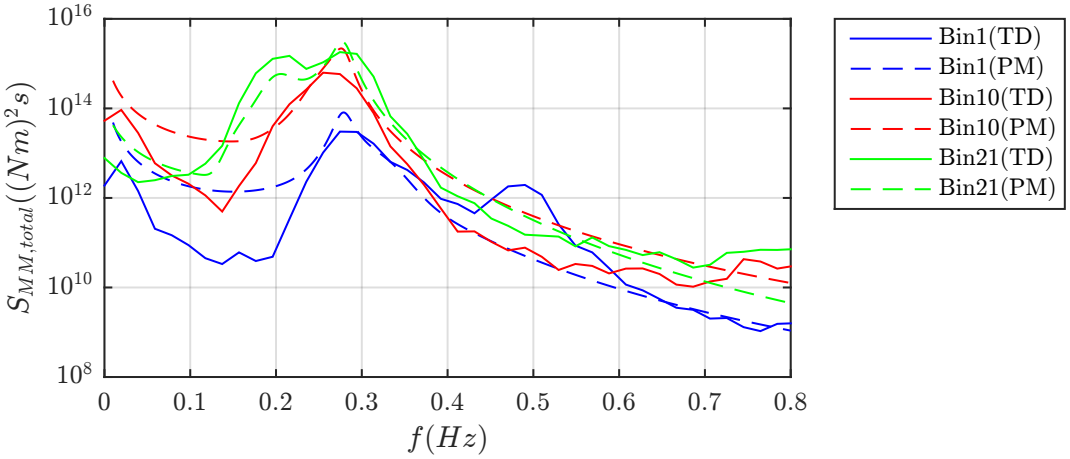

Figure 4-23: Comparison of PSD of the mudline moment for Bin 1, 10 and 21 for TD and PM

Finally, it is interesting to assess the outcome of the different methods with which Bladed and PM produce the stress range histograms: Rainflow counting and Dirlik method accordingly. Examining the same states as previously, it is notable from Fig. 4-24 that the histograms converge adequately. Obviously, TD histograms have numerous spikes but this behaviour is impossible to be captured by a smooth statistical distribution like Dirlik. However, the general trend is captured both in terms of shape and magnitude.

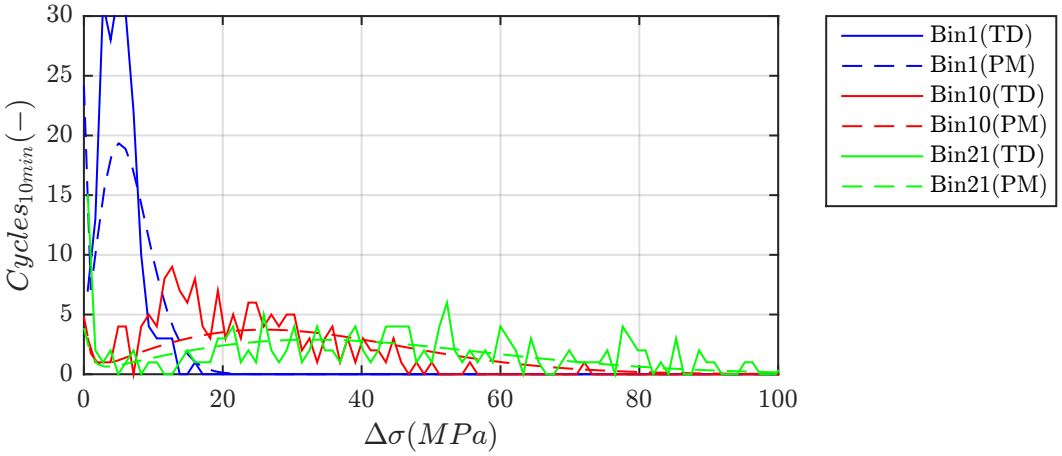

Figure 4-24: Comparison between stress histograms for 10-min periods for Bin 1, 10 and 21 for TD and PM

Chapter 5

Site Variation Models

A support structure does not respond identically to any site variation which rises the need for a closer investigation of the factors that influence the integrity of the structure. Insight into the extent to which these variations deteriorate the resistance to fatigue failure is of tremendous benefit during the early design phase. Chapter 4 already supplies the necessary framework on the basis of which to build models that extrapolate a detailed fatigue assessment at one location in the farm to another when variation is specified. In the following sections, these models are firstly qualitatively explained and at a next stage a sensitivity analysis is conducted.

5-1 Soil Profile

Although the most well known variation of soil properties is vertical, the spatial variation over different locations within a farm occurs rather frequently (Fig. 5-1). Slight or radical, a difference in the soil properties of layers or even totally different layers influence the natural frequency of the structure. How the consequences of the latter affect the overall behaviour and integrity has been explicitly discussed in the previous chapter.

The non-linear soil springs calculated by the F.E. model for the estimation of the natural frequency are specified by the profile of the soil surrounding the foundation pile (see Section 4-2-4). Such properties are: friction angle ϕ (for sand), shear strength C_u (for clay), the strain at half the maximum allowable stress $e50\%$ (for clay) and submerged unit weight γ. Apart from the p-y curves, no other term except for *Dynamics* is dependent on the soil profile as it has been identified in Section 3-2. This description is illustrated in Fig. 5-2. The superscripts *ref* and *new* indicate whether certain blocks remain the same as at the reference location or need to be re-calculated (DAF for instance), namely whether the modules are disabled or enabled respectively.

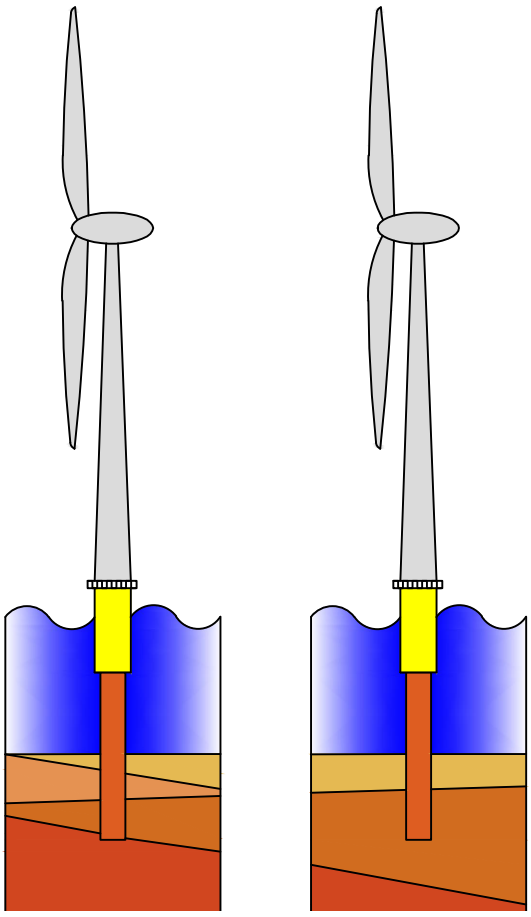

Figure 5-1: Soil variation, hence different layers, at two different locations within an OWF

Despite the successful benchmarking of the base framework, presented in Section 4-4, the accuracy can be further strengthened to account for uncertainties or systematic errors. The over-estimation of wind and the slight under-estimation of wave loads as Fig. 4-22 and 4-23 denote are for instance such systematic errors. To effectively address the above, correction factors are implemented for the analysis at the new location, as shown in Fig. 5-2. They are derived by performing the developed (simplified) fatigue assessment at the reference location and comparing the results to the outcome of the detailed assessment as Fig. 5-3 explains. More specifically, the correction factor cf for the i^{th} state is the ratio of the partial damage calculated by the proposed methodology (PM) and the time-domain (TD):

$$cf_i = \frac{Damage_i^{ref,TD}}{Damage_i^{ref,PM}} \tag{5-1}$$

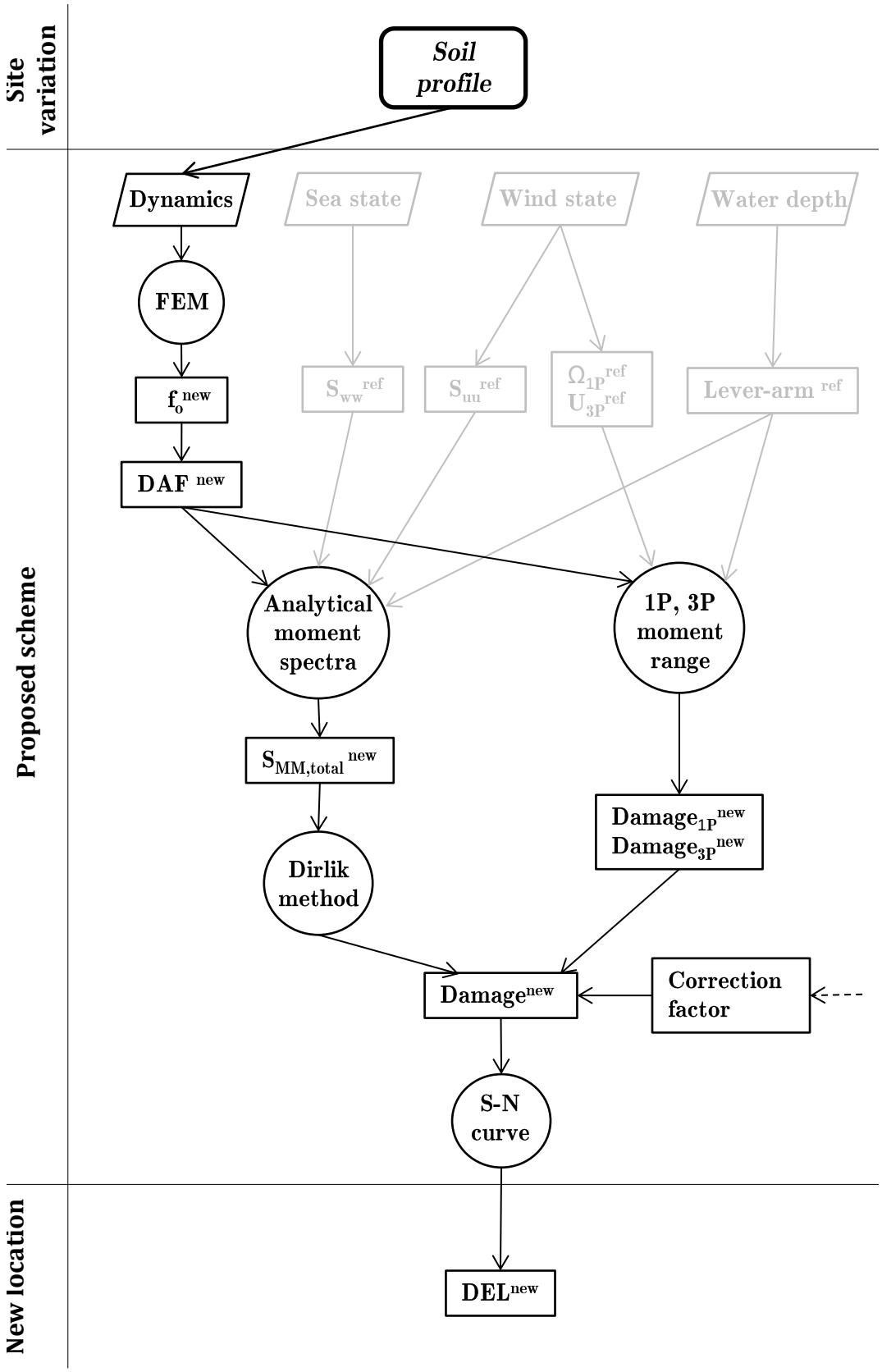

Figure 5-2: Simplified fatigue assessment model accounting for soil profile variation in a farm

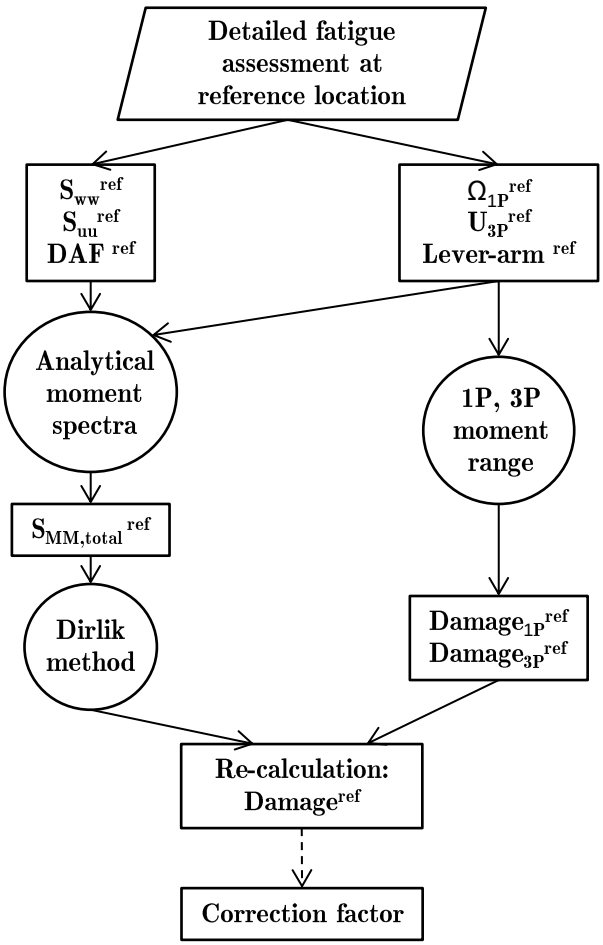

Figure 5-3: Application of the proposed methodology explained in Chapter 4 at the reference location for the derivation of the correction factors.

5-2 Bathymetry

Like soil profile, the bathymetry might change considerably over a site. However, the complexity of addressing different depths rises compared to soil profile. The dependency study in Section 3-3 proves that looking at either of loads or natural frequency when investigating depth variation would be insufficient. Hence, such a variation requires re-analysis of the *Dynamics* that affects the stiffness, as well as the *Water depth* that affects the loads. In addition, the *Sea state* is dependent on the depth. For instance, smaller depth might make water waves to be characterised from deep to shallow and as a result the friction between the sea surface and bottom affects the wave height and period [22]. A theory describing this effect is the Sverdrup-Munk-Bretschneider (SMB) method [22]. As far as the correction factors are concerned, these are applied to this model as well following the process given in Fig. 5-3.

Regarding the forms of the input, the new water depth is obviously inserted as a separate value when triggering *Dynamics* and *Water depth*, but the influence on the *Sea state* is somewhat more complex. Leaving the responsibility for the pre-analysis to the wind farm developer, this impact can be incorporated as an updated table with environmental states: with either the same states and appropriately adjusted probabilities of occurrence or a totally renewed table for the new location.

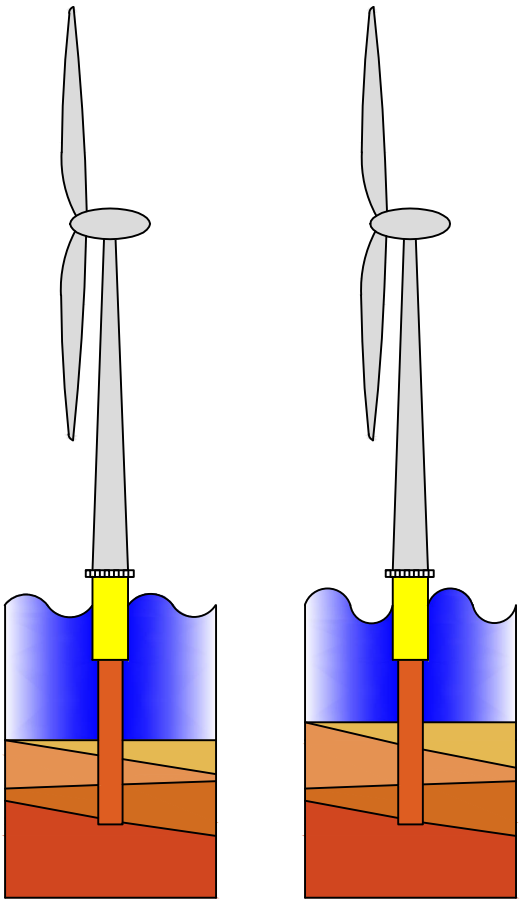

Figure 5-4: Water depth variation and the accompanied impact on the wave height at two different locations within an OWF

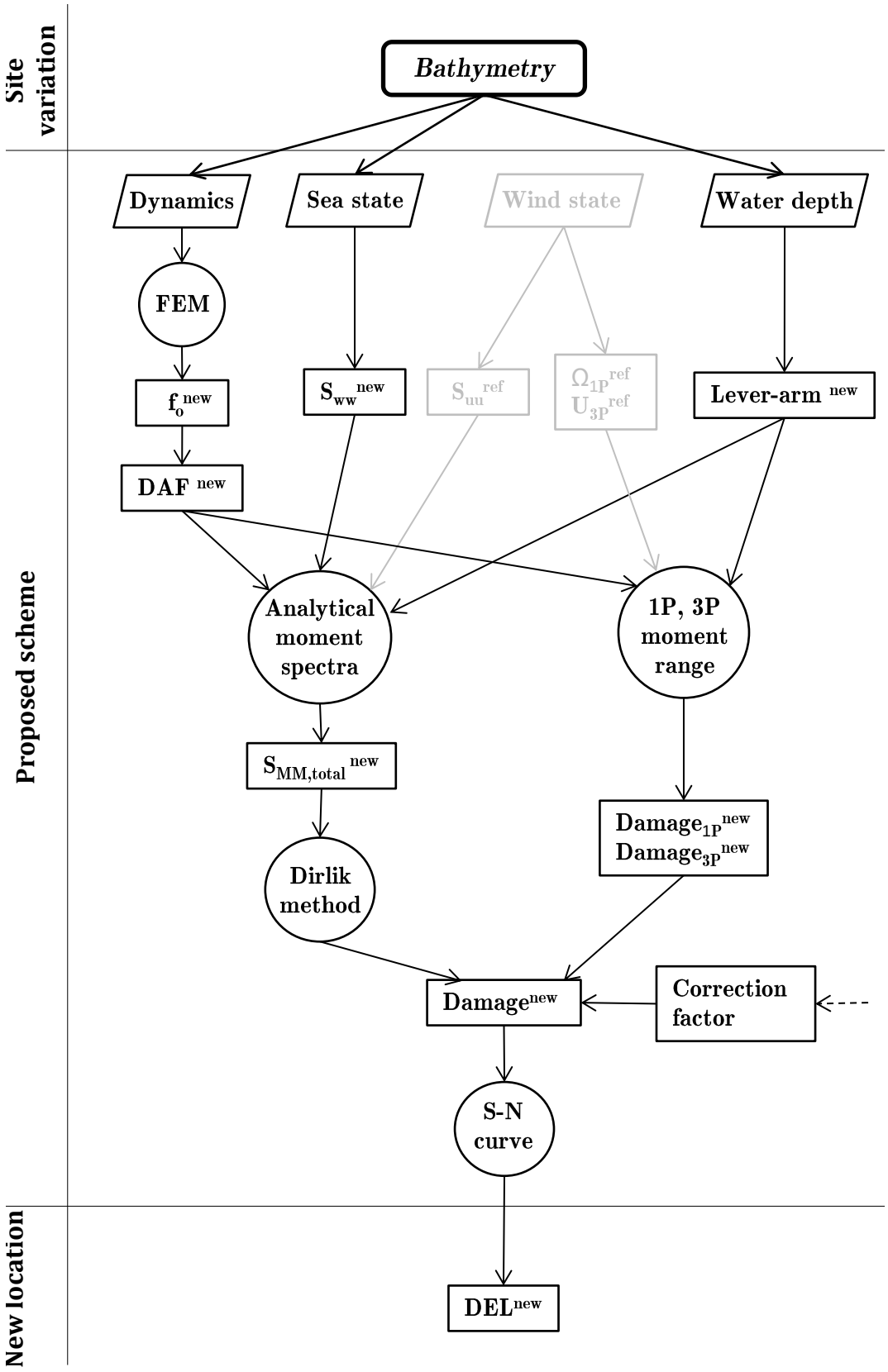

Figure 5-5: Simplified fatigue assessment model accounting for bathymetry variation in a farm

5-3 Wake Effects

The disturbance of the flow downwind of a turbine is a major aspect not only when it comes to power production loss but also loading. In OWF's the need to identify the wake effects is greater than onshore for two reasons:

- The lower turbulence implies insufficient mixing of the outer flow with the wakes, thereby slower wind speed recovery.
- The wake-induced turbulence is of importance offshore because the ambient turbulence is lower than onshore.

A wake effect analysis on a preliminary layout is expected in this model to result in the wind speed deficit as well as the increased turbulence, both depicted in Fig. 5-6 and ultimately an updated table with the lumped environmental states. Similarly to the water depth variation, wake effects can either affect the probabilities of each state or are likely to necessitate a complete re-formulation of these states. In either case Fig. 5-7 explains that only the *Wind state* module is enabled while the *Dynamics*, the *Sea state* and the *Water depth* remain unaffected.

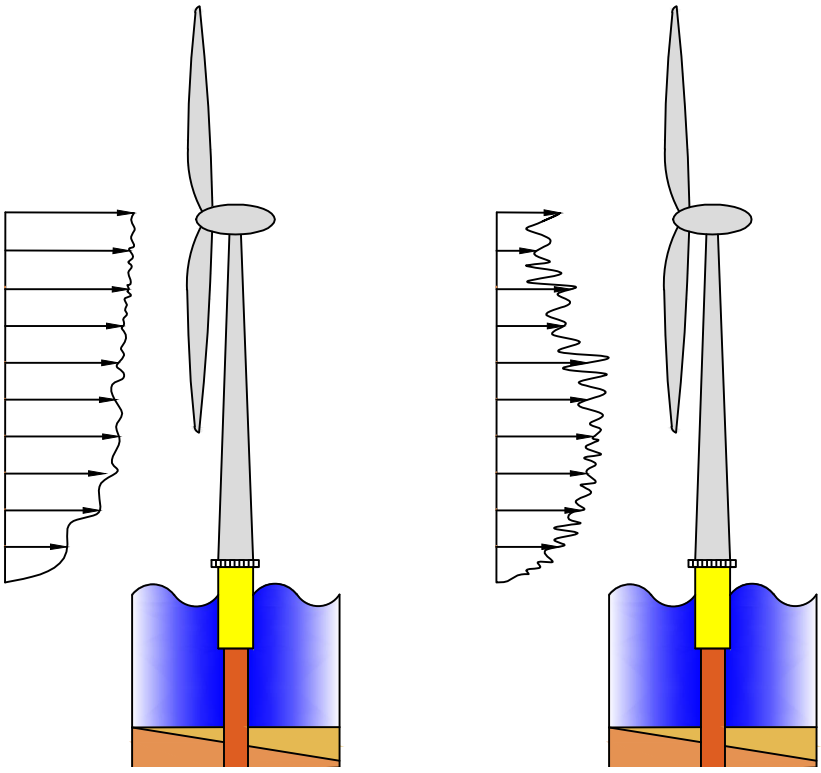

Figure 5-6: Wake effects resulting in disturbed wind field experienced by a turbine located at a downwind location within an OWF

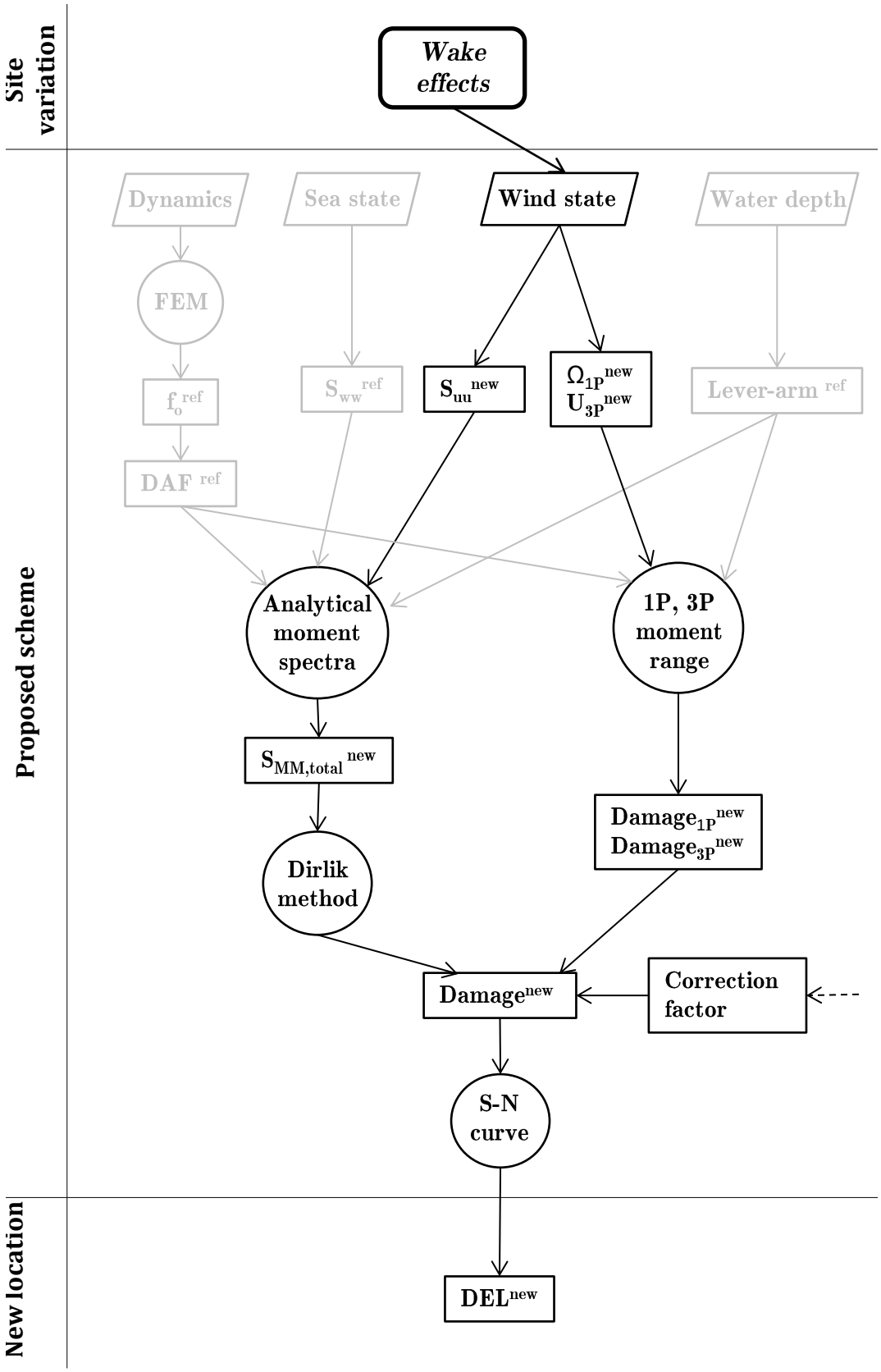

Figure 5-7: Simplified fatigue assessment model accounting for wake effects in a farm

5-4 Sensitivity Analysis

In this section, the previously presented variation models are applied to conduct a sensitivity analysis. By tuning appropriately and to a realistic extent several site parameters, the crucial, moderate and less-damaging factors are identified based on DEL and further discussed. In accordance with the flow charts illustrated in Fig. 5-2, 5-5 and 5-7, it should be noted that the *Correction factors* are not applied since the relative change is here of importance instead of the absolute values. The investigated site variations are H_s, T_p, ϕ, γ, $\bar{U}$, TI and d.

Remarks

- As baseline for the sensitivity analysis, a Vestas V90 is considered with the specifications given in Table 4-1. The support structure is the one installed in OWEZ and already presented in Section 4-4 for the validation of the methodology. Accordingly, the environmental states are the same. As far as the soil profile is concerned, baseline soil consists of only sand layers with $\gamma = 10kN/m^3$ and $\phi = 30deg$ (an acceptable assumption when targeting the analysis to the North Sea [3]) resulting in $f_o = 0.28Hz$.
- With regards to the variation pattern for distributed parameters, Fig. 5-8 explains that when either of ϕ or γ varies, this variation is automatically applied to all soil layers. Likewise, when H_s, T_P, $\bar{U}$ or TI are assessed the change is implemented to all environmental states by multiplying the values of the baseline's table by the corresponding factor each time as Fig. 5-9 shows.

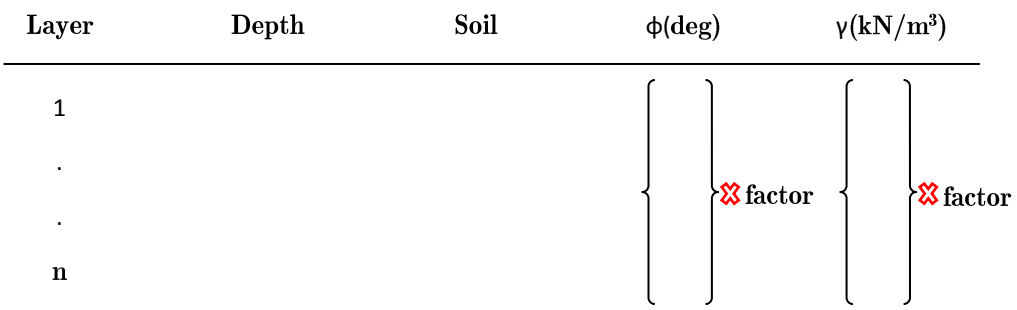

Figure 5-8: Application of soil property change universally to the soil profile

- As far as the water depth is concerned, there are two different cases under which the sensitivity of DEL to d can be evaluated:

  1. Keeping L_P constant as in the baseline point, elongating thus the structure length for increased d (or shortening it for shallower waters).
  2. Fixing the total length of the structure, assuming always constant Z_{hub} and adjusting thus L_P according to d.

  Despite the direct influence of d on the sea state, as Fig. 5-5 shows, the actual effect of depths on H_s and T_P extends beyond the scope of the present study. Therefore, the sea state is always input assigning the responsibility for this calculation to the wind farm

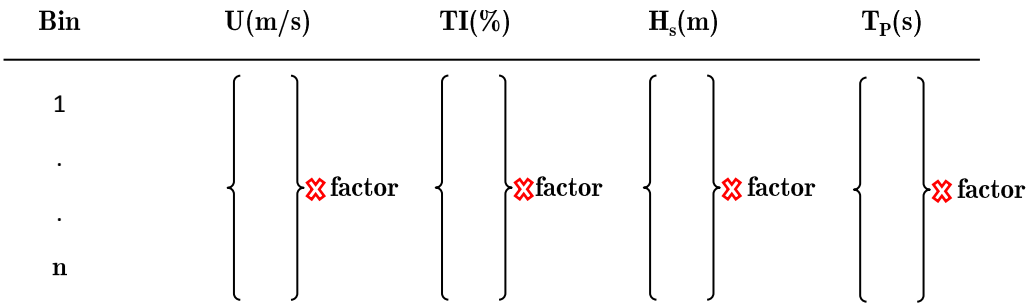

Figure 5-9: Application of change of environmental conditions universally to the lumped fatigue bins

developer. Likewise, wake effects are not calculated by the presented scheme but given as input.

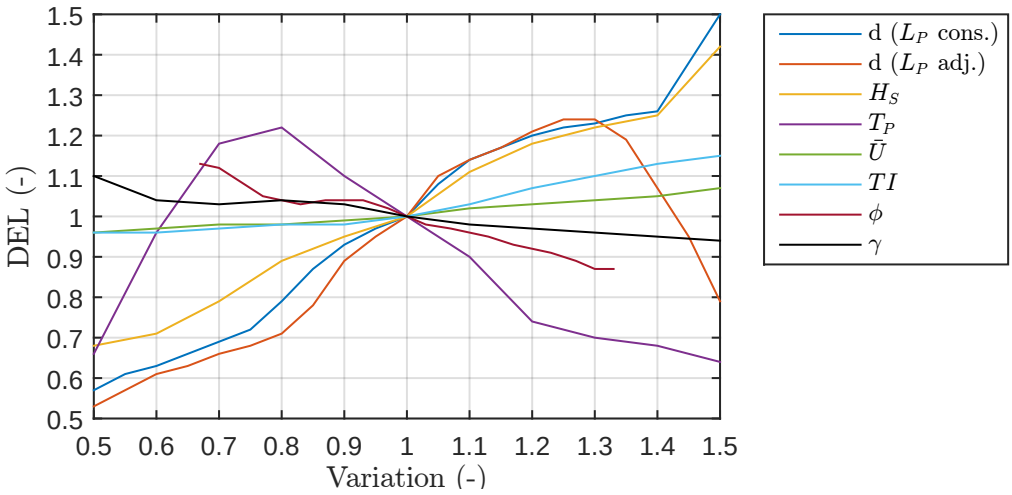

Figure 5-10: Sensitivity of equivalent loads DEL to varying site conditions

The results of the sensitivity analysis, depicted in Fig. 5-10, clarify first of all that deep waters give severe rise to fatigue. The factors that play a role to this are the higher flexibility (f_o closer to excitation frequencies) and the bigger lever-arms, hence higher moments. Interestingly, DEL in the case of the adjustable L_P increase only up to a certain point. Beyond this point the fatigue seems to be less intense. Any peculiarity accompanying this observation vanishes by a closer look at f_o. More specifically, L_P is so short at the right edge of the graph that f_o reaches $0.14Hz$. In other words, the structure leaves the 1P region and performs soft-soft, a behaviour that is provided in Fig. 5-11. On the contrary, the rightmost point for fixed L_P in Fig. 5-10 corresponds to $0.22Hz$. Hence, it is not only well within the core of the 1P region but also in the vicinity of severe sea states, therefore the higher fatigue damage. However, to prevent misleading conclusions it is by no means implied that deep waters and insignificant penetration lengths are in reality favourable regarding stability or other limit states, e.g. the ultimate limit state (ULS).

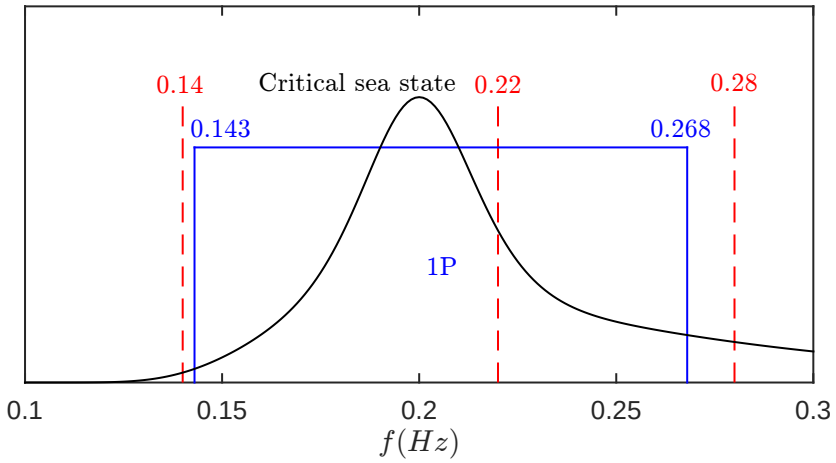

Figure 5-11: 1P frequency range for the example used in the sensitivity analysis with respect to the baseline f_o $(0.28Hz)$ and the rightmost f_o of Fig. 5-10 for two cases: L_P fixed and not fixed, 0.22 and $0.14Hz$ respectively

Regarding the sea characteristics, both H_s and T_P seem to be almost as fatigue determining as d. Waves with higher heights obviously increase the loads, while the short wave periods not only increase the loads but they also excite the structure closer to its f_o. More specifically, although f_p is in the majority of the fatigue bins lower than f_o, it might in some cases lie in the vicinity of f_o amplifying the response. The impact is substantial particularly when these states are severe and with relatively high occurrence probability. This resonance is noticed in Fig. 5-10 where DEL increase with shorter T_P and upon coinciding with f_o they drop again as the period becomes very small. This observation is also illustrated in Fig. 5-12 for the example used in the present sensitivity analysis.

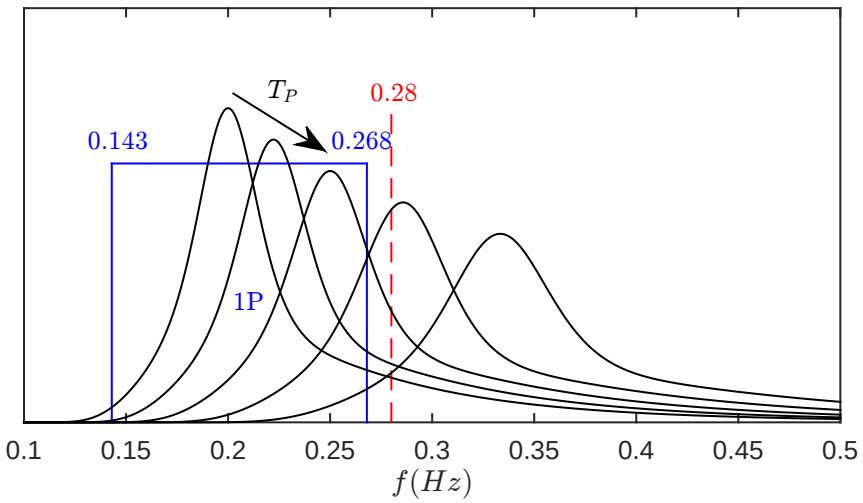

Figure 5-12: Higher fatigue damage induced by shorter T_P (higher f) as it approaches resonance at f_o $(0.28Hz)$ and reduction of damage once f_P exceeds f_o

Emphasising on the wind characteristics, TI affects DEL to a lesser extent than d, H_s and

T_P. In principle, this observation could be presumed beforehand since wave loading is in general the design driver for offshore wind structures [38]. Notably, this would be even more visible if the analysis were conducted for a deeper location ($20m$ can be regarded as moderate depth). Furthermore, a difference between the sensitivity to TI and $\bar{U}$ is observed and can prove to be of importance when addressing layout, wake and fatigue aspects in the design phase.

Finally, with respect to the soil it is evident that an increase of either of the two parameters induces further soil support, stiffer structure (higher f_o) and ultimately a drop of DEL. It is additionally worth to highlight that the outcome reveals a stronger dependence of DEL on ϕ than on γ. Therefore, it can be concluded that ϕ variation in a farm is more critical than γ variation. Tables with absolute values of the varying properties can be found in Appendix B.

Chapter 6

FLS Extrapolation: Case Study

Having formulated the methodology to estimate the resistance of the structure to fatigue failure (Chapter 4) and incorporated it to individual site variation models (Chapter 5), a case study is performed in this chapter under combined variations. The main objectives of this case study are to elaborate on efficient ways of application of the developed framework and to ultimately demonstrate its practical usefulness. The above must be achieved under realistic site variations that are likely to be encountered by OWF developers universally. Finally, the functionality of the correction factors, as introduced in Chapter 5, is tested.

6-1 Set-up Specifications

This section contains all the necessary information with regards to the set-up of the case study. The construction is a rather crucial process provided the aforementioned goal of resemblance to reality. Aspects, such as the examined location, its environmental conditions, the type of the turbine and the geometry of the support structure are here specified and justified.

6-1-1 Site Selection

The location of Hornsea (United Kingdom) is selected which is a designated part of the North Sea from the Round 3 permitting process (Fig.6-1). The selection is made such that the site fulfills the following criteria:

- it favours the analysis of the site variability, for instance by having a wide range of water depths (yet still suitable for monopiles)
- it is an area that attracts global attention when it comes to offshore wind
- it has not been developed yet so as to prevent contradicting results or misleading conclusions

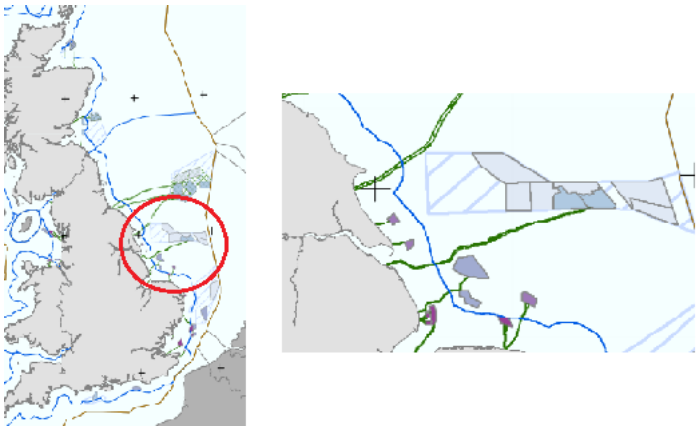

Figure 6-1: Offshore site of Hornsea, UK

Following a site-specific processing of the environmental data for wind speed, wave height and wave period, a 3D scatter diagram is constructed and presented in Fig. 6-2. The environmental states are specified by lumping this diagram with the highest possible accuracy and applying the necessary adjustments, e.g. expressing the wind speed at 90m (estimated hub height) and calculating the peak period from the zero-crossing period. Table 6-1 contains the states that characterise the global climate of Hornsea.

		Tz (s)							Total
Hs (m)	U (m/s)	3.0 - 4.0	4.0 - 5.0	5.0 - 6.0	6.0 - 7.0	7.0 - 8.0	8.0 - 9.0	9.0 - 10.0	
> 4.0	24						0.4	0.3	0.7
	21							0.1	0.1
3.5 - 4.0	18					0.3	0.2		0.5
	15					0.2	0.2		0.4
	12						0.4		0.4
3.0 - 3.5	17				0.2	0.7			0.9
	14				0.1	0.5	0.1		0.7
	11					0.4	0.4		0.8
2.5 - 3.0	15				1.5	0.1			1.6
	12				0.9	1.2	0.2		2.3
	9					1.1	0.3		1.4
2.0 - 2.5	14				0.6	2.9			3.5
	10				3.7	0.6			4.3
	6				0.3	0.6			0.9
1.5 - 2.0	11			5.6	0.9				6.5
	7			3.6	4.2				7.8
	2			0.5	0.7				1.2
1.0 - 1.5	9		3.7	6					9.7
	6		2.2	5.7	2.2	1.7			11.8
	2				1.9	0.9			2.8
0.5 - 1.0	7	14	2.5						16.5
	3	1.8	6.4	1.7					9.9
0.0 - 0.5	6	3.6	3.1						6.7
	2	3.9	3.9	0.8					8.6
Total		23.3	21.8	23.9	17.2	11.2	2.2	0.4	100.0

Figure 6-2: The 3D scatter diagram (wind speed, significant wave height and zero-crossing period) for Hornsea

6-1-2 Variations

The variations to be taken into account have already been defined in previous chapters and are related to: soil profile changes, water depth differences over the site and wake effects. The former two can be arbitrarily assigned to different locations and are independent from

Table 6-1: Lumped environmental states at the area of Hornsea

Global climate for Hornsea					
State	$U(m/s)$	$TI(\%)$	$H_s(m)$	$T_P(s)$	Occurence (%)
1	3.8	26.5	0.3	6.0	7.5
2	4.7	23.2	0.3	4.6	7.8
3	4.7	23.2	0.6	5.6	10.6
4	5.2	21.9	1.3	8.8	6.7
5	7.3	18.3	1.3	7.1	17.6
6	7.9	17.5	0.9	4.6	15.8
7	8.4	17.0	1.8	8.5	5.8
8	10.0	15.7	1.9	7.2	9.7
9	12.0	14.6	2.3	8.5	4.6
10	12.6	14.3	2.8	11.2	0.5
11	12.9	14.2	2.6	9.8	2.4
12	13.6	13.9	2.8	9.8	4.1
13	13.8	13.9	3.1	11.2	0.5
14	14.9	13.5	3.6	11.2	0.8
15	16.7	13.0	2.9	8.5	2.4
16	17.2	12.9	3.3	10.1	1.9
17	21.4	12.1	3.8	9.8	0.5
18	28.5	11.4	4.3	11.8	0.8

the interaction between the neighbouring turbines. On the contrary, the wake effects stem by definition from this interaction. Therefore, a preliminary farm layout has to be conceptualised. The layout with the denoted reference position and these that are examined as new (according to the terminology of the previous chapters) is illustrated in Fig. 6-3.

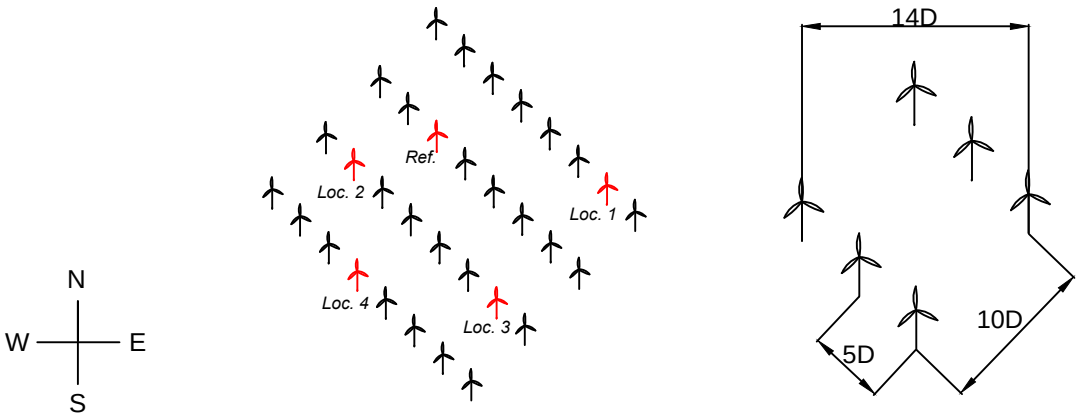

Figure 6-3: The conceptually designed farm layout investigated in the case study

Bathymetry

The zone of Hornsea is rather large which implies radical water depth variation beyond the desired extent. Since the monopile is not suitable for very deep waters, the case study is essentially targeted to a certain part of the zone where the bathymetry is predominantly between 25 and 35m [39]. This comes in agreement with a rough estimation of the depths, depicted in Fig. 6-4, by retrieving satellite data and creating contour lines from it.

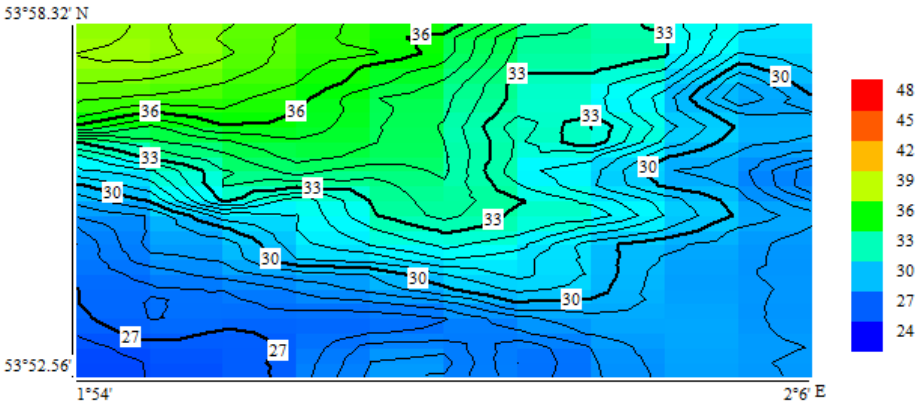

Figure 6-4: Bathymetry map of (part of) the area of Hornsea

Sea State

The influence of the water depth on the wave height and period is regarded prerequisite knowledge of the end user of the proposed scheme. Therefore, the depth-sea state interaction needs to be accounted for in order to imply a suitable variation to this case study thanks to the diverse bathymetry of Hornsea. To this direction, the theory describing the sea profile oriented to the shore is used [40]. It is also assumed that the waves propagating to deeper waters obey this theory. Doing so, the global sea climate of Table 6-1 can be assigned to the mean depth (30m) and thus get insight into the effects of both higher and smaller wave heights. Finally, assuming same wave length and frequency (namely unaffected by the water depth), the correlation reduces to [40]:

$$\frac{H_{s2}}{H_{s1}} = \sqrt{\frac{d_1}{d_2}} \tag{6-1}$$

Wind State

The wake effects are, as the sea state variations, prerequisite knowledge for the present framework. The approximation of the former is considered here with the implementation of the following calculations. Regarding the wind speed deficit, the Jensen model is used to estimate the reduced speed $U_{wake,i}$ at each location i and for every wind direction θ that prevails in the examined farm of Fig. 6-3 [20]. The power curve and the thrust coefficient curve for the chosen turbine, as this is introduced in Section 6-1-3, are input for the analysis. This procedure requires also the lumping of the wind rose in 8 directional bins with probabilities f_{wd} (θ) and the assumption of same Weibull distributions in each bin. Following these steps,

every undisturbed wind speed U (Table 6-1) is translated to a local (or effective) wind speed U_{eff} at each location i:

$$U_{eff}(U)_i = \int_{-180}^{180} U_{wake,i}(\theta) f_{wd}(\theta) d\theta \tag{6-2}$$

For the wake-induced turbulence, the concept of *wind farm ambient turbulence intensity* (introduced by Frandsen) is applied to derive TI_{wake} for every direction [15]. Unlike wind speed, the linear relation of DEL to TI results in an effective TI_{eff} (accounting for the S-N exponent m) when assessing fatigue load cases according to the equation below. Hence, for every undisturbed wind speed U (Table 6-1), the effective intensity TI_{eff} is found at location i:

$$TI_{eff}(U)_i = \left[\int_{-180}^{180} TI_{wake}(\theta)_i^m f_{wd}(\theta) d\theta \right]^{1/m} \tag{6-3}$$

Soil Conditions

The access to accurate soil profiles for the specific zone is quite difficult (a problem that is also encountered in Section 4-4). Instead, three datasets of soil layers are available for an area in the Danish North Sea. Considering them representative for the UK North Sea as well, they are used in the present case study and are presented in Table 6-2.

Table 6-2: Three soil profiles used in the case study (with depth in m below mudline, γ in kN/m^3, ϕ in deg and C_u in kPa)

Soil profiles for Hornsea											
Soil 1				Soil 2				Soil 3			
Depth	γ	ϕ	C_u	Depth	γ	ϕ	C_u	Depth	γ	ϕ	C_u
9.2	9.5	35.0	0.0	5.0	8.5	25.0	0.0	5.0	8.5	25.0	0.0
10.2	9.5	0.0	100.0	8.6	8.5	25.0	0.0	8.5	8.5	25.0	0.0
14.7	9.5	33.0	0.0	11.9	9.0	35.0	0.0	11.9	9.0	35.0	0.0
36.0	10.0	35.0	0.0	22.0	9.0	35.0	0.0	22.0	9.0	35.0	0.0
39.3	10.0	33.0	0.0	30.0	9.0	35.0	0.0	33.3	9.0	0.0	75.0
43.4	9.5	0.0	200.0	33.3	9.0	35.0	0.0	35.1	9.0	35.0	0.0
50.0	9.5	30.0	0.0	35.1	9.0	0.0	75.0	44.5	9.0	35.0	0.0
62.0	10.0	33.0	0.0	44.5	9.0	35.0	0.0	51.4	9.0	35.0	0.0
				48.5	9.0	30.0	0.0				
				49.4	9.0	35.0	0.0				
				51.4	9.0	25.0	0.0				

Summary of Variations

Having presented the principles behind the variations, the local environmental conditions of each location are summarised in Table 6-3 and are predicted in the following manner:

- the local wave height H_s of each state is adjusted according to Eq. 6-1

- the local wind speed U_{eff} and turbulence intensity TI_{eff} of each state are calculated for every undisturbed wind speed (Table 6-1) by Eq. 6-2 and Eq. 6-3 respectively
- a soil profile from Table 6-2 is arbitrarily assigned

Table 6-3: Specifications for the reference position and the investigated locations in the test case

Specifications of Hornsea farm locations					
Location	Reference	1	2	3	4
Env. States	Table C-1	Table C-2	Table C-3	Table C-4	Table C-5
Depth	$30m$	$32m$	$36m$	$30m$	$26m$
Soil profile	1	2	2	3	1

6-1-3 Turbine Selection

As far as the wind turbine is concerned, the developers of the Hornsea farm have reached to an agreement for a large-scale turbine with a rated power of 6MW (Siemens 6.0-154). Due to lack of detailed information on its performance and behaviour, NREL 5MW is used instead [18]. The similar rated capacity and size render this turbine suitable for the following investigation. The general specifications of the turbine are provided in Table 6-4.

Table 6-4: Gross properties of NREL 5MW [18]

Turbine: NREL 5MW	
P_R	5,000 kW
D	126 m
U_{cut-in}, U_R, $U_{cut-out}$	3, 11.4, 25 m/s
Ω	6.9 - 12.1RPM
m_{top}	350,000 kg
m_{1P}	220 kg
R_{1P}	42 m

6-1-4 Support Structure Geometry

The support structure is designed for the reference location. More specifically, the structure consists of a pile with $6.2m$ diameter (presently well within the engineering limits), a transition piece with $6.5m$ diameter and a tower with $68m$ length. The typical ratios of D/t are chosen approximately 80 for the monopile and 100 for the tower. The penetration depth is $45m$, i.e. 7 times the pile diameter. As for the platform height, extreme conditions such as $H_{s,50}$, storm surge and maximum tides elevate it to $+16m$ (to MSL) [39]. The overlap length of the transition piece is defined by the required grout length and is $9m$. Finally, scour protection is considered for all the positions in the farm. The stucture (at the reference location) is given in Fig. 6-5 while the drawings for the other positions are provided in Appendix C. The only difference of the latter from Fig. 6-5 is obviously the penetration at each location.

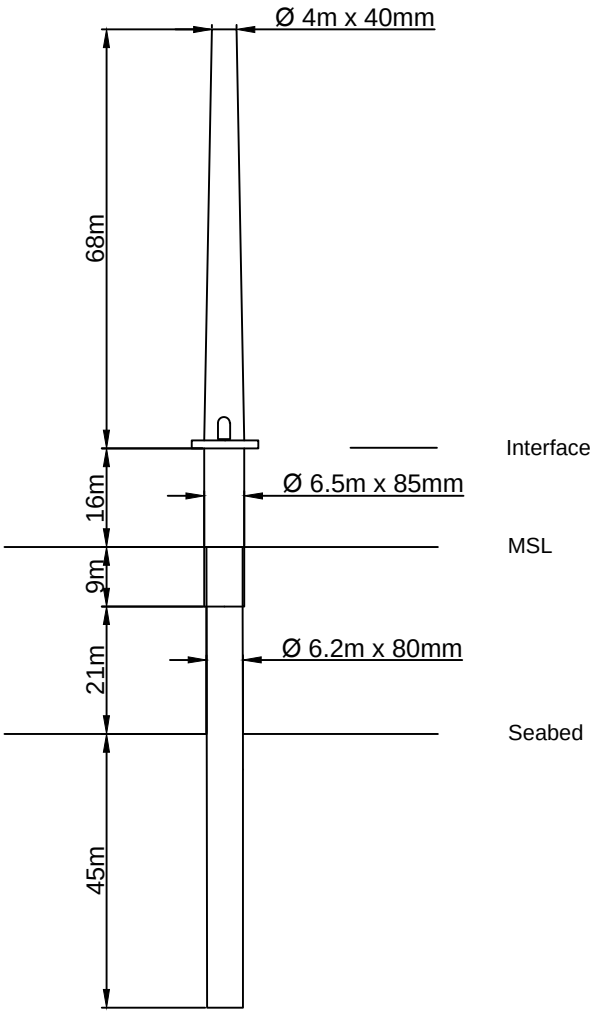

Figure 6-5: The support structure considered for the case study (here installed at the reference position with $d = 30m$ and $L_P = 45m$)

6-2 Results of Fatigue Extrapolation

The complete set-up of the case study allows now the application of the developed framework. The meticulous analysis is treated first and next the outcome of the extrapolation at the new locations is assessed.

Reference location

The detailed assessment calibrates the model by yielding the correction factors cf that are applied later to the locations of interest. In this way, it becomes feasible to diminish the systematic errors identified and discussed in Section 4-4. Bladed is again used to perform the detailed analysis in the time-domain (TD) at the reference position and Table 6-5 presents the results.

In the process of extracting the values of cf on the basis of Eq. 5-3, the matching shown by

Table 6-5: Assessment of fatigue at the mudline of the reference location by applying the proposed methodology (PM) and the time-domain (TD) framework for the derivation of the correction factors cf

Reference position of Hornsea		
	TD	PM (before correction)
$Damage(-)$	0.196	0.154
$\Delta\sigma_{EQ}(MPa)$	44.58	43.70
$DEL(MNm)$	103.57	101.53

Table 6-5 is already satisfactory before the calibration. As anticipated though, the results do not converge to the same level as in the validation presented in Section 4-4. The reasons for this are explained in that section. To achieve higher accuracy, cf are calculated per state (not for the ultimate $Damage$) and they can be expressed in terms of $Damage$ or DEL ratios. The values in terms of the latter for this case study are given in Fig. 6-6.

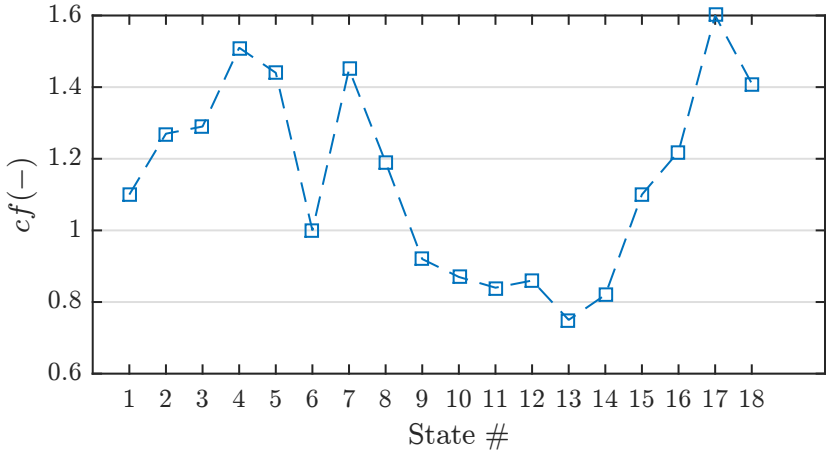

Figure 6-6: The correction factors cf in terms of DEL that are applied later to the new locations

Values higher than 1 show that the partial $Damage_i$ of the state i that is calculated by the PM is lower than the corresponding value produced in TD. Likewise, the PM damaging character of the state is higher than in TD for values lower than 1. The rigorous discussion in Section 4-4 about the methodology's performance has concluded that peaking wind loads are over- whereas severe waves are under-predicted. This is noticed once again in this case study by observing cf in Fig. 6-6 at states 9-14 and 15-18 respectively.

A final remark concerning the low values of $Damage$ (< 0.2) is that although the focus in this study is the FLS, the structure must withstand all limit states. However, the integrity of the structure is assumed to be achieved only by the satisfaction of the natural frequency constraint in order to avoid meticulous ULS calculations. As a consequence, $Damage$ is not close to 1, as it would be if fatigue were the design driver.

New locations

The extrapolation from the reference location to locations 1-4 is at this stage performed: the developed model (Chapter 4) is applied at each location and is accompanied by the

correction factors as stemmed from the reference location (Fig 6-6). The results are denoted as PM again, while time-domain (TD) analysis with Bladed is conducted at these locations as well to benchmark the results. Doing so, the ultimate efficiency of the extrapolation can be determined by assessing the deviation in terms of errors.

Table 6-6: The results of extrapolating fatigue at the mudline by applying the PM (with cf) and verification by comparing them to TD for the examined locations of the case study

Extrapolation of fatigue assessment and verification				
Location	Result	TD	PM	Error (%)
1	$Damage(-)$	0.333	0.236	-29.1
	$DEL(MNm)$	122.65	110.29	-10.1
2	$Damage(-)$	0.608	0.402	-34.0
	$DEL(MNm)$	136.24	127.80	-6.2
3	$Damage(-)$	0.199	0.208	+5.0
	$DEL(MNm)$	103.68	104.78	+1.1
4	$Damage(-)$	0.076	0.122	+61.8
	$DEL(MNm)$	91.67	99.06	+8.1

By looking at Table 6-6, it is undeniable that the trend is captured and the errors are within acceptable engineering limits. The locations 1 and 2 are more onerous than the rest, since the structure installed in these (particularly in the latter) have the shortest lifetime. On the other hand, both methods indicate that location 4 is the least critical, while location 3 is quite comparable to the reference position. Although the two equally critical environmental conditions, d and H_s (see Section 5-4), are here conflicting as Eq. 6-1 explains, the d increase outweighs the H_s decrease with respect to $Damage$. One reason for the bigger influence of d is the fact that the range here is 26-36m, whereas the sensitivity analysis is performed for a range of less dominant depths, 20-30m (detailed results for the sensitivity analysis are provided in Appendix B). Another reason is the square root in Eq. 6-1 that lessens the impact of d on H_s. Finally, the conclusion in Section 5-4 about the soil being not significantly crucial is verified by location 3. With the soil (and wake effects) being the only factor that differentiates it from the reference position, $Damage$ and DEL are almost equal.

Regarding the errors given in Table 6-6, $Damage$ is considerably more sensitive to DEL, therefore the errors of the former are, as anticipated, much higher than these of the latter. However, the sign of the error and specifically its correlation with d is more of importance to point out. In Fig. 6-7, $Damage$ and DEL errors are depicted against d (normalised by the reference depth $d_{ref} = 30m$). There is an obvious tendency towards optimism regarding fatigue resistance at locations with greater depths (negative errors) and conservatism (positive errors) at locations with depths shallower than d_{ref}. On the contrary, the error at the location with equal d is insignificant. In addition, it is also notable to observe the effectiveness of the correction factors as illustrated in Fig. 6-7. Upon their application, the errors drop with the exception of the shallowest location. At that position (location 4: $d/d_{ref} = 0.87$), the tendency of the correction factors to correct DEL and $Damage$ by increasing them is not efficient since they are over-estimated in the first place.

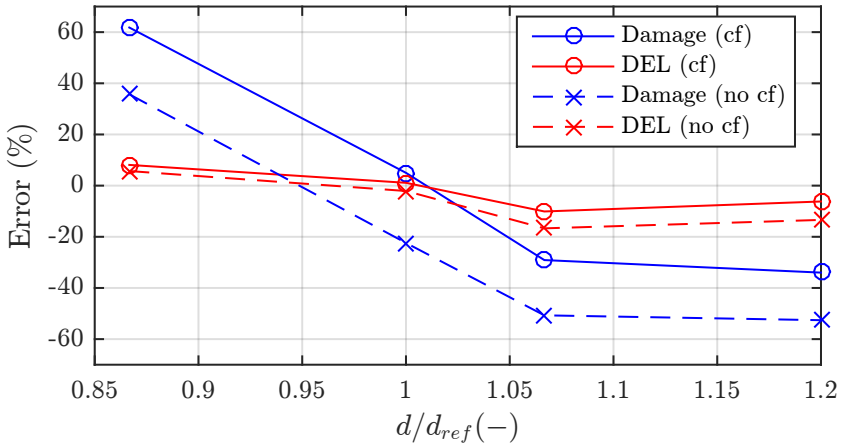

Figure 6-7: The errors for $Damage$ and DEL from the extrapolation of the FLS assessment to the 4 investigated locations plotted versus the normalised d (by the reference $d_{ref} = 30m$) - before (no cf) and after (cf) applying the correction factors cf

6-3 Discussion and Expansion of the Method

The main emphasis of the discussion is placed on the origin of the errors presented earlier. An issue that has not been covered yet is the part of the pile that is subjected to the analysis. The results of Table 6-6 and Fig. 6-7 correspond to the mudline of each location. This means that the values of cf are calculated at $z = -30m$ for the reference position but later applied at $z = -32m$, $-36m$ and $-26m$ (location 1, 2 and 4 respectively, whereas location 3 has the same $d = 30m$). However, it is worth to additionally look into the application of the cf at other parts of the structure as well.

The extrapolation of the FLS assessment at several elevations is shown in Fig. 6-8. More specifically, the elevation (i) is in principle the mudline-assessment at all locations, the results of which are presented in Table 6-6. To examine whether cf are more efficient when calculated and applied at always the same heights, elevations (ii) and (iii) are assessed. Finally, crucial limitations discussed in Section 4-3 are the non-capturing of the wave loading propagation to the tower and the 1-DOF DAF. Therefore, the MSL and $z = +40m$ are investigated as elevations (iv) and (v) respectively. The former is the elevation that is the closest to the sea level and more prone to experience this propagation, while the mode shape of the 2^{nd} eigen-frequency would have the largest deflection at the latter if not ignored. It could be stated that instead of the largest deflection of the mode shape, the elevation where the curvature of the mode shape is maximum would be the most suitable to focus on as elevation (v). The limited accuracy of the available mode shape, however, makes it difficult to spot this elevation with high precision. Table 6-7 summarises the above.

A comparison of the PM (with the correction factors from the reference position) to FLS assessments with Bladed yields the error of DEL at the elevations given in Fig.6-9. This extensive look triggers discussion on the performance of the model. It also quantifies the implications of the model's weaknesses. With respect to the elevations well below MSL, i.e. $(i), (ii)$ and (iii), the conclusion is that PM results in substantial convergence from an engineering point of view to the analysis of Bladed.

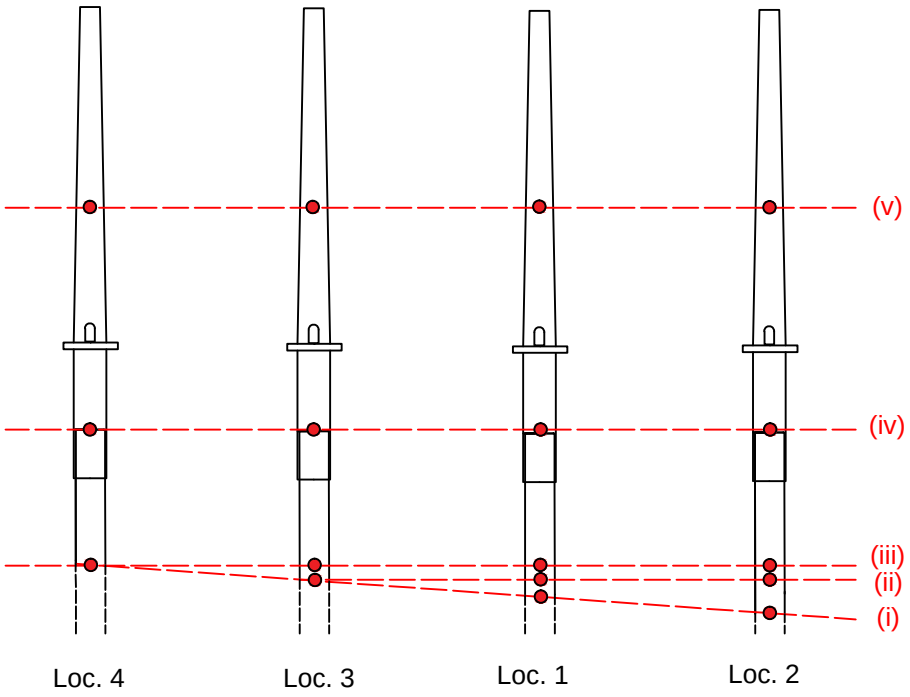

Figure 6-8: Different elevations at which FLS extrapolation is in the case study conducted

Table 6-7: Specifications of the different elevations presented in Fig. 6-8

Further investigation of fatigue extrapolation

Elevation	Description	Motivation
i	Mudline (Table 6-6)	Critical section (for driven pile)
ii	Depth of the reference location ($z = -30m$)	Same elevation of calculation and application of cf
iii	Depth of the shallowest location ($z = -26m$)	as in (ii)
iv	MSL	Influence of wave load propagation above MSL
v	$z = +40m$	Influence of higher eigen-frequencies

On the contrary, significant deviation is observed at elevations (iv) and (v), the highest of which occurs at (iv). By integrating the forces from the bottom to the top (as in static cantilever beams) any wave-induced loads at the tower are dismissed. This explains why DEL are under-predicted by more than 15% at this elevation. Slightly lower yet still considerable errors are also observed at elevation (v) which means that neglecting the higher eigen-frequencies is not insignificant at this part of the structure. This observation along with that of the previous paragraph imply that PM is more efficient when performed close to the mudline and can, hence, contribute to the optimisation of the foundation pile specifically. As a last remark, the dynamics still possesses an important role since the error bars for (iv)

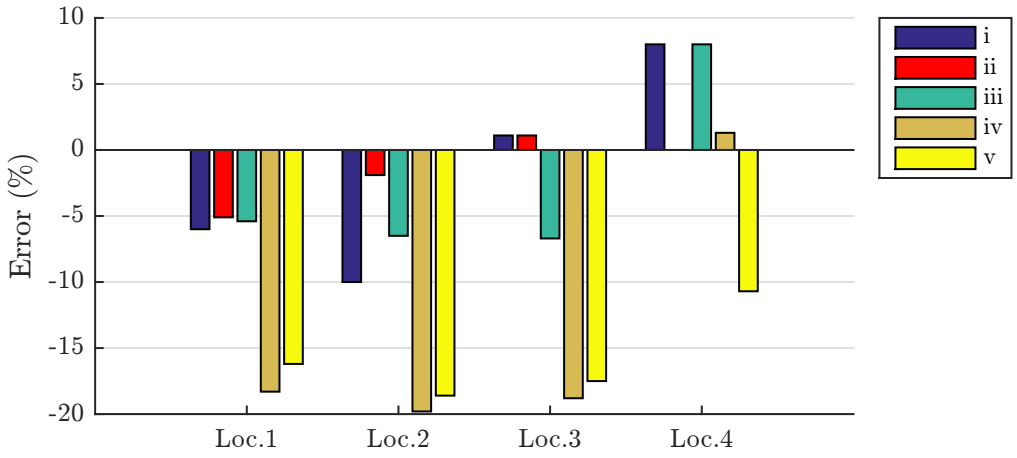

Figure 6-9: The error of DEL at every location and for the five extrapolation patterns as illustrated in Fig. 6-8

maximise at location 2 and for (v) minimise at location 4. The reason is that the flexible structure at location 2 has a natural frequency closer to the governing wave excitations, a phenomenon that is under-predicted by PM. At location 4, though, the frequency lies safely away from them and this under-estimation is not equally visible.

Chapter 7

Fatigue-driven Tailored Design of Monopiles

The facilitation of financially vital choices in the early stage of the design of an OWF when it comes to efficient support structure dimensioning has been set as one of the objectives in Chapter 1. The developed and previously presented scheme for fast FLS extrapolation at various locations can drive this procedure from a perspective of fatigue. Hence, the approximation of the strength of multiple structures against cyclic loads takes the design process forward halfway. The remaining way to the solution requires suitable re-designs to bring the approximated strength of the structures to the desired level. The outcome can then serve as the starting point of a detailed assessment. The fact that the re-designs will have been the result of such a fast yet extended analysis is expected to diminish the number of the iterations that will be ultimately required for the detailed assessment.

7-1 General Principles

Individually designed support structures have the potential to reduce the total mass of steel in an OWF with large variations. This section specifies firstly the failure mechanisms that are investigated in the presented tailoring procedure. Next, it explains the concept behind the exploration of the possibility of mass reduction and finally makes explicit the required steps. It is also clarified that the tailoring of the structures is restricted to varying foundation piles to come in accordance with the conclusions of the reliability of the method from the previous chapter.

7-1-1 Limiting States

The core of the present research is FLS, therefore the customisation of the design is primarily triggered in this chapter by fatigue. The assumption, however, that the structure is susceptible solely to FLS failure would not be fair. Therefore, an elaboration on other critical limiting states follows below.

Yield stress

The utilisation of the strength of the material under ULS, namely exceeding the yield stress, is not included in the analysis. What justifies this option is that any adjustments in the geometry driven by fatigue strength are not restricted by the requirement of integrity under ULS.

Buckling

On the contrary, the buckling of the structure has a complementary behaviour to fatigue. In other words, the satisfaction of the one tends to oppose the satisfaction of the other (as graphically explained later) and it is meaningful to examine the influence of individual designs on both of them.

Foundation stability

Finally regarding the foundation stability, this limit state is not vital to be investigated because the penetration depths, which dominate lateral deflection and rotation, remain constant at every location.

7-1-2 Nature of the Problem

Having defined the limiting states and the objective of the tailoring process, the problem can be formulated. The pile diameter and thickness are the two independent design variables and the problem is initially addressed as an optimisation process with two design variables [54]. As Fig. 7-1 depicts, it is defined by a design space where the acceptable sets of solutions, namely combinations of pile diameter and thickness, are located. The limiting states effectively restrict the design space, from which the optimal set of variables is selected.

Regarding the FLS constraint, the corresponding curve is drawn on the basis of retaining the equivalent stresses $\Delta\sigma_{EQ}^{new}$ at the new location below the maximum allowable $\Delta\sigma_{EQ}^{ref}$ that are calculated at the reference position. Given the equivalent loads DEL^{new} at the new location under the local conditions, the pile diameter, thickness and consequently moment of inertia have to be readjusted such that the inequality $\Delta\sigma_{EQ}^{new} \leq \Delta\sigma_{EQ}^{ref}$ is satisfied. The development of the inequality, assuming moment of inertia $I^{'} \approx \pi/8(D_P^{'})^3 t_p^{'}$ for a thin-walled annular cross-section, leads to the correlation between the readjusted $t_P^{'}$ and $D_P^{'}$ at the new position:

$$t_P^{'} \geq \frac{4DEL^{new}}{\pi(D_P^{'})^2 \Delta\sigma_{EQ}^{ref}} \tag{7-1}$$

As for buckling, sufficient strength has to be achieved so as for the foundation pile not to fail during the installation. To ensure this, the following condition that relates $t_P^{'}$ and $D_P^{'}$ has to be satisfied (both variables in mm) [28]:

$$t_P^{'} \geq 6.35 + \frac{D_P^{'}}{100} \tag{7-2}$$

The aim is to minimise the use of material for the individual support structures, in other words their cross-sectional area $A \approx \pi D_P^{'} t_P^{'}$ and thus bring down costs. Such a goal is achieved by

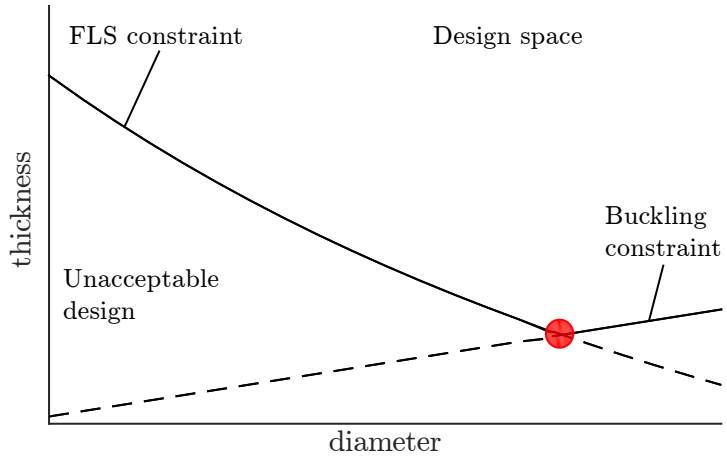

Figure 7-1: Reduction of an optimisation problem with two independent design variables (here, pile diameter and thickness) to a root finding problem towards the adjustment of the geometry of a support structure

reaching values of *Damage* at all locations as close to 1 as possible (accounting for various uncertainties), or the corresponding equivalent stresses close to $\Delta\sigma_{EQ}^{ref}$. The above implies that the solution must lie on the curve that represents the FLS constraint. Likewise, the solution must also lie on the curve of buckling resistance to achieve the minimum strength. As a result, the inequality constraints reduce to equality constraints and the problem for each location is converted from optimisation to a root finding process. The final solution is in each case the intersection of the two equality constraints, as denoted in Fig. 7-1.

7-1-3 Tailoring Procedure

The site-specific design of the support structures is coupled with the scheme for the quick FLS extrapolation as developed and demonstrated in previous chapters. A flow chart of the procedure is provided in Fig. 7-2.

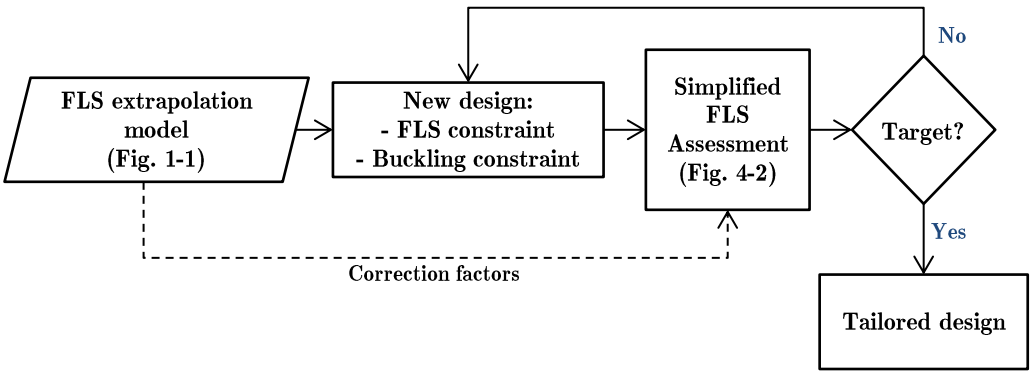

Figure 7-2: The process of tailoring the design of the support structures that follows the fatigue extrapolation over an OWF

Starting from the detailed assessment at the reference position for the derivation of the correction factors, $\Delta\sigma_{EQ}^{ref}$ are calculated. The application of the method for quick fatigue prediction yields DEL^{new} and $\Delta\sigma_{EQ}^{new}$ at the new location under the local environmental conditions. These steps eventually comprise the scheme depicted in Fig. 1-1, the application of which is presented in Chapter 6. The curves of the two equality constraints can at this point be drawn and their intersection leads to the desirable geometry. In principle, this geometry satisfies the constraints. However, the updated dimensions $D_P^{'}$ and $t_P^{'}$ are likely to influence DEL^{new} and ultimately lead to $\Delta\sigma_{EQ}^{new}$ other than $\Delta\sigma_{EQ}^{ref}$. Therefore, the methodology for simplified FLS assessment is conducted iteratively to the constantly updated designs till the targeted $\Delta\sigma_{EQ}^{ref}$ has been reached.

Remarks:

Two important notes that are related to the correction factors are the following:

- how accurate is it to apply those that have been extracted from the initial design to the updated design?
- at which elevation should they be applied to (see Fig. 6-8)?

Regarding the former point, the geometry is on the one hand not expected to change radically by the tailoring procedure. It is, therefore, in principle acceptable to assume that the correction factors attributed to the initial design are equally suitable for the updated geometries. On the other hand, it is still ambiguous to what extent this assumption is accurate. Hence, this doubt requires further attention and should be addressed more rigorously in related work in the future. For the sake of simplicity, though, the same correction factors are implemented in the present study. As for the investigated part of the structure where the extrapolation takes place, the mudline-approach is followed, namely elevation (i) from Fig. 6-8.

7-2 Application to FLS Extrapolation Case Study

The efficiency of the scheme for individual support structures in an OWF given the estimations of fatigue at various locations on a reference structure is demonstrated in this section. The analysis uses as input the results from the case study of Chapter 6 which is effectively extended further to yield tailored piles and obeys the principles as provided in Section 7-1. Hence, the fatigue target $\Delta\sigma_{EQ}^{ref}$ in the process is defined by the reference position which would be anticipated to correspond to *Damage* close to 1. Although the structure at the reference position is designed for Chapter 6 in such a way to have much lower *Damage*, it is still used as a reference. After all, the demonstrative nature of this chapter shifts the interest to the verification of the functionality of the methodology instead of the absolute numbers.

The results of the tailored pile designs are presented in Table 7-1 and the mass reduction that can be achieved seems by no means negligible. Looking at these 4 locations, support structures can be installed that are already lighter by 16 % (0.90/1.06=0.85), than the heaviest one (location 4 with respect to 2) even under this strict target. This percentage presumably rises as the number of investigated locations increases and particularly if the pile length is an additional degree of freedom. As a matter of fact, the mass of the foundation piles in OWF under construction might vary up to 40 % [19].

Table 7-1: Individually designed foundation piles for the locations that are investigated in the case study of Chapter 6

Tailored design applied to the case study					
Location	Ref.	1	2	3	4
Pile diameter (m)	6.2	6.7	6.9	6.6	6.3
Pile thickness (mm)	80	74	76	73	70
Pile mass (tn)	905.2	897.3	963.4	885.5	815.3
Pile mass (relative to the reference)	-	0.99	1.06	0.98	0.90

7-3 Discussion

An observed trend to emphasise is the relation of the tailored geometries with the reference structure. By plotting D_P and t_P in Fig.7-3 for all locations and contrasting them to those of the original structure, the following remarks can be made:

- the customised diameters are in all positions larger - even at locations 3 and 4 with the same and shallower depth than at the reference position respectively
- the individual piles are in all positions thinner - even at locations 1 and 2 which have greater depths and subsequently require piles with higher moment of resistance.

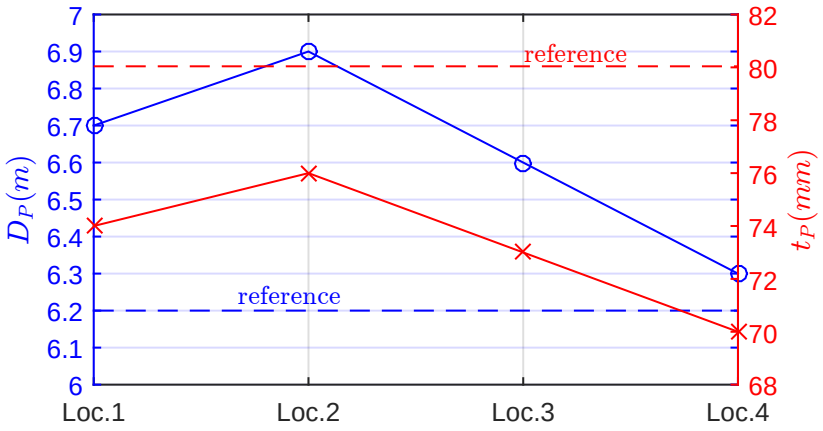

Figure 7-3: Contrast of the tailored designs (pile diameter D_P and thickness t_P) to the reference structure

Notably, Fig.7-3 highlights a difference in the design philosophy. To be more specific, reaching the buckling constraint in the tailoring procedure results in large diameters and small thicknesses of the individual piles. However, a smaller diameter and a larger thickness are selected by not taking into consideration this constraint during the design phase of the reference structure. The consequence of the latter is that the reference structure is likely to be heavier than it would be if the design philosophy of this study was also applied to the reference pile. The location where the estimated equivalent loads are the closest to the reference (or targeted) equivalent loads before the tailoring process is location 3. The reason why this

location resembles the reference location is evidently that it has the same depth. As a result, one would correctly think that tailoring there would hardly be essential. Nonetheless, this is not visible in Fig.7-3. This leads to the conclusion that the developed scheme is also capable of revealing the direction towards more efficient design even at the reference structure since the re-designed pile at location 3 is slightly lighter.

Finally, it is again mentioned that these conclusions are derived by a procedure aiming to demonstrate the functionality of the scheme and with a very strict fatigue target for the re-designing. The present analysis is also subjected to certain degrees of uncertainty. Such degrees are the identified errors of fatigue extrapolation that propagate from the case study to the present chapter (Fig. 6-9). Another such uncertainty is the suitability or not of the correction factors that are calculated for a structure with different geometry. As a consequence, this scheme is mainly intended to provide the basis for the customisation of the design of support structures.

Chapter 8

Conclusions

The conclusions that are extracted are of importance to the future users of the developed methodology and designers in general and are presented in this chapter. Additionally, certain suggestions aim to trigger the attention of future research on the field of fatigue of offshore wind support structures.

8-1 Conclusions

The achievement of this study is that it proves that the development of a framework for FLS estimations in a simple and quick manner so as to address site variations in an OWF is feasible. The first key component of this method is a flexible and fast model for fatigue estimations. The concept of the simplified frequency-domain relies on the analytical approximation of the dynamic response to wind and wave excitation as well as the separate handling of the harmonic loads induced by the operating wind turbine. Through by-passing the need for complicated numerical approaches and advanced software, the process becomes computationally appealing. The second component are the correction factors stemming from a reference location in an OWF. They calibrate the model and increase the overall reliability. On the basis of the above, the scheme is converted from a stand-alone computation to a methodology that is adjusted to location-specific conditions. Ultimately, the overall performance renders the developed framework suitable for the investigation of numerous locations across an OWF and preliminary optimisation of all support structures in the farm and particularly of the foundation piles.

With respect to the stand-alone model itself, the simplification of the conventional frequency-domain is successfully done. Not only is it by far more computationally affordable than the usual procedure in common-practice, but it also yields quite reasonable fatigue predictions. Inevitably, the simplicity with which it estimates the resistance to varying loads rises systematic errors that are not necessarily visible at once. An example of elusively high accuracy is the assessment at OWEZ which reveals limitations only when being looked into extensively. These are identified to be the over-calculation of the peak loads caused by the wind excitation and the under-prediction of those caused by the wave excitation. The former is expected to

dominate the analyses of OWF at shallow waters. The latter becomes crucial for OWF with big depth variations since the correction factors are calculated at one position and are very sensitive to the placement of the eigen-frequency with respect to the wave excitation. Hence, sites with various depths imply different natural frequency at each location and therefore the correction factors can either be insufficient or have higher values than necessary, as revealed at the case study.

Regarding the performance of extrapolating the fatigue analysis upon the application of the correction factors, the case study shows that this concept proves efficient particularly at elevations close to the seabed. The convergence of the damage estimates to the outcome of Bladed at these elevations is clearly adequate and acceptable from an engineering point of view. The fact that this research is targeted to the early design phase and not to the final, therefore detailed, stage strengthens the argument. On the contrary, the poorer performance of the proposed scheme for extrapolation when assessing cross-sections of the structure in the vicinity of the sea level or above seems too significant to ignore. This lower accuracy stems from the following limitations: firstly, that the wave loads propagate to the tower and this is disregarded by the model and secondly, that higher eigen-frequencies would have an impact on the result if not neglected. As a result, the methodology in its present structure can prove useful for the optimisation of the foundation pile design.

Finally and as far as the individual design of monopiles is concerned, a preliminary attempt of implementing the developed framework is presented. The goal is to effectively translate the various fatigue estimations into potential mass reduction. Focusing on the re-design of the piles in the last chapter, the results are rather promising and do not contradict similar scientific efforts that praise the prospects of the customised design. It is concluded that by considering only pile diameter and thickness changes, foundation piles that are already lighter by 16 % can be installed in an OWF. The addition of the pile length as extra design variable would presumably raise this percentage but necessitate simultaneously lateral stability checks that have not been performed here. Furthermore, the provided discussion on the strength and design philosophy of the reference structure proves the significance of this location for the tailoring procedure besides the fatigue extrapolation. Finally, a point to stress is that the benefit of individual designs is not contrasted to increased manufacturing costs since the latter are disregarded in this study. It would perhaps be worth to investigate to what extent these designs would induce extra costs.

8-2 Developments, Extensions and Future Work

The following suggestions for future work are provided on the grounds of the desirable goal that each of them may achieve:

Model accuracy

One of the limitations is observed to be the low reliability of fatigue estimations at and above MSL. Given that disregarding the load impact from lower elevations at higher elevations as well as the 1-DOF approach on dynamics result in this poor performance. A method that could cope with these simplifications would be a dynamic amplification factor as a function of the elevation: $DAF(z)$. Nonetheless, it is still to be investigated whether the requirements

of such an alternative would come in conflict with the simple nature that the scheme must have.

Furthermore, the modeling of the cyclic loads induced by the rotor is another field the accuracy of which can be increased. Especially concerning the 3P loads, the phenomenon of the tower shadow is represented by a thrust variation over the rotation of the blades. Therefore, it is critical to select the suitable thrust coefficient at different azimuth angles and this is now done under Momentum theory. However, the validity of this global theory to represent the local disturbance of the flow is believed to be cumbersome and inaccurate. Alternatives should be introduced.

As far as the geometry of the monopile is concerned, there is definitely room for more accurate approaches. Such alterations are the tapered shape of the pile and the transition piece as well as varying thickness of these two components. This extension is relatively easy to be implemented and becomes even more significant when the methodology is used in industry-oriented projects than in the research level.

Similarly to the previous point, the grouting is a part of the support structure modeling that can be improved. The F.E. model does not distinguish the grout from steel at the overlapping section and simply treat this part as if it would consist of three steel annuli: pile, transition piece and the area in-between the former two. This may over-predict the stiffness or affect the stress calculation.

Model capabilities

The tailoring of the support structure is here inevitably restricted to cross-sectional changes in the foundation pile: diameter and thickness. The reason is that more global tailoring philosophies, such as the alteration of the pile length, would necessitate an investigation of more limit states than fatigue and buckling. Hence, a more complete methodology for individual designs can be achieved with the implementation of preliminary ULS or lateral stability checks during the re-designing. The benefit of the above is that even greater prospects of mass reduction can be claimed as the number of the design variables increases.

Moreover, in order to handle the increasing interest of the offshore wind industry in deeper sites, the methodology for quick FLS estimations can be advanced to include the jacket as a support structure. Evidently, the proposed concept of the simplified frequency-domain framework is recommended again as the basis of the analysis. What needs to be adjusted are the analytical calculations for deriving the PSD of the response. Such a development potentially facilitates feasibility studies of the most efficient type of support structure in terms of fatigue failure.

Holistic OWF optimisation

The most ambitious goal is the incorporation of this analysis for FLS extrapolation into a holistic OWF optimisation process. By adding the influence of the positioning of the turbines on the support structure costs, the sensitivity of the capital expenditure (CAPEX) to design choices increases. After all, the wake effect estimation is, as already explained, required prior to the FLS extrapolation for deriving the wind states locally. Hence, such a coupling can facilitate the development of the optimiser. An alternative scheme would be the selection of the turbine based on fatigue estimations of the support structure over an OWF. In that

case, contradicting conclusions can be examined, such as big-scale turbines for higher energy production but at the same time small and light RNA's for mass reduction of the foundation.

Bibliography

[1] Alati, N. et al. "Fatigue Analysis of Offshore Wind Turbines on Fixed Support Structures." Key Engineering Materials 569 (2013): 539-546.

[2] Arany, L. et al. "Simplified critical mudline bending moment spectra of offshore wind turbine support structures." Wind Energy (2014).

[3] Balson P., Butcher, A. et al. "North Sea Geology" British Geological Survey. (2001).

[4] Bianchi, F. D., De Battista, H. and Mantz, R.J. "Wind turbine control systems: principles, modelling and gain scheduling design". Springer Science & Business Media. (2006).

[5] Blanco, M.I. "The economics of wind energy." Renewable and Sustainable Energy Reviews 13.6 (2009): 1372-1382.

[6] Burton, T. et al. "Wind energy handbook". John Wiley & Sons. (2001).

[7] Carstens, H., Nielsen, H.B. et al. "Lowering Costs by Individual Design of Foundation Structures". Ramboll. (2007).

[8] de Vries, W. E., and Krolis V. D. "Effects of deep water on monopile support structures for offshore wind turbines." EWEC, Milan (2007).

[9] de Vries, W., "Multi-member Structures", Offshore Wind Support Structures presentation. Delft University of Technology. (2014).

[10] DNV. "Design of Offshore Wind Turbine Structures". Offshore Standards. (2007).

[11] DNV. "Joint Industry Project". Offshore Standards. (2010).

[12] Fischer, T., et al. "Optimization of a monopile support structure using offshore-specific wind turbine controls." Proceedings of the European Offshore Wind Conference (EOW). (2009).

[13] Fischer, T., and Kühn, M. "Site sensitive support structure and machine design for offshore wind farms." EWEC, Marseille (2009).

[14] Fischer, T., de Vries, W.B. and B. Schmidt. "Upwind design basis (WP4: offshore foundations and support structures)". Upwind. (2010).

[15] Frandsen, S. T. "Turbulence and turbulence-generated structural loading in wind turbine clusters". RisøNational Laboratory. (2007).

[16] Halfpenny, A. "A frequency domain approach for fatigue life estimation from finite element analysis." Key Engineering Materials 167 (1999): 401-410.

[17] Henderson, A. R., Zaaijer, M.B. and Camp, T.R. "Hydrodynamic loading on offshore wind turbines." Report SW-0218x, Section Wind Energy, Technical University of Delft (2003).

[18] Jonkman, J., Butterfield, S., Musial, W. and Scott G. "Definition of a 5-MW Reference Wind Turbine for Offshore System Development." National Renewable Energy Laboratory. (2009).

[19] Kallehave, D. et al. "Optimization of monopiles for offshore wind turbines." Philosophical Transactions of the Royal Society of London A: Mathematical, Physical and Engineering Sciences 373.2035 (2015): 20140100.

[20] Katic, I., Højstrup, J., and Jensen, N.O. "A simple model for cluster efficiency." European Wind Energy Association Conference and Exhibition. (1986).

[21] Kawai, H., Michishita, K. et al. "Design Wind Loads on a Wind Turbine for Strong Wind". BBAA VI International Colloquium on Bluff Bodies Aerodynamics and Applications. (2008).

[22] Kim, N., and J. W. Jin. "Sensitivity analysis of offshore wind turbine tower caused by the external force." KSCE Journal of Civil Engineering 17.5 (2013): 859-864.

[23] Kost, C., Mayer, J. et al. "Levelised Cost of Electricity Renewable Energy Technologies". Fraunhofer ISE. (2013).

[24] K*ü*hn, M. J. "Dynamics and design optimisation of offshore wind energy conversion systems". TU Delft, Delft University of Technology, (2001).

[25] Lloyd, Germanischer. "Guideline for the certification of offshore wind turbines." (2005).

[26] Labuschagne, A., van Rensburg, J. and Van der Merwe, A.J. "Comparison of linear beam theories." Mathematical and Computer Modelling 49.1 (2009): 20-30.

[27] Manwell, J., McGowan, J. and Rogers, A. "Wind energy explained: theory, design and application". John Wiley & Sons. (2010).

[28] MLA RP2A-WSD, A. P. I. "Recommended practice for planning, designing and constructing fixed offshore platforms-working stress design-." Twenty-. (2000).

[29] Nijssen, R. "Fatigue life prediction and strength degradation of wind turbine rotor blade composites". TU Delft. Delft University of Technology. (2006).

[30] Norton E., "Wind and Wave Misalignment Effects on Fatigue Loading", Garrad Hassan and Partners, (2009).

[31] OWEZ. "Offshore Windfarm Egmond aan Zee - General Report", Shell. (2008).

[32] Pandit, A. "Efficient Support Structure Design for Variation of Environmental Parameters within an Offshore Wind Farm". Delft University of Technology. (2014).

[33] Peeringa, J. "Fatigue Loading on a 5MW Offshore Wind Turbine due to Combined Action of Waves and Current". IOP Science. (2014).

[34] Petersen, E.L., et al. "Wind power meteorology." Riso National Laboratory, Roskilde, Denmark, Technical Document No. Riso-I-1206 (EN) (1997).

[35] Ringeval, A., and Huang, Y. "Random vibration fatigue analysis with LS-DYNA." 12th International LS-DYNA Users" Conference. (2012).

[36] Savenije, F. and Peeringa. J. "Integral Wind Turbine Design and Analysis in the Frequency Domain". ECN. (2009).

[37] Segeren, M. L. A. "Influence of a boatlanding and j-tubes on wave loads and wall thickness of the monopile support structure design". Proceedings of the EWEA Offshore 2011 Conference. (Amsterdam) 2011.

[38] Seidel, M. "Wave induced fatigue loads". Stahlbau 83.8 (2014): 535-541.

[39] SMart Wind."Hornsea Offshore Wind Farm Project One: Environmental Statement". http://infrastructure.planningportal.gov.uk/. (2013).

[40] Sorensen, R. M. "Basic wave mechanics: for coastal and ocean engineers". John Wiley & Sons. (1993).

[41] Swagata, D., Karnik, N. and Santoso, S. "Time-domain modeling of tower shadow and wind shear in wind turbines". International Scholarly Research Notices 2011. (2011).

[42] Tan, J. et al. "Effect of Tower Shadow and Wind Shear in a Wind Farm on AC Tie-Line Power Oscillations of Interconnected Power Systems." Energies 6.12 (2013): 6352-6372.

[43] TC88-MT, I. E. C. "IEC 61400-3: Wind Turbines-Part 1: Design Requirements." International Electrotechnical Commission, Geneva (2005).

[44] Thomsen, K. "Offshore wind: a comprehensive guide to successful offshore wind farm installation". Academic Press, (2014).

[45] Thiry, A. et al. "Optimization of monopile offshore wind structures." Marstruct. (2011).

[46] Van Der Tempel, J. "Design of support structures for offshore wind turbines". TU Delft, Delft University of Technology, (2006).

[47] Veldkamp, H. F. "Chances in wind energy: a probalistic approach to wind turbine fatigue design". TU Delft. Delft University of Technology. (2006).

[48] Vemula, N. K. et al. "Design solution for the upwind reference offshore support structure." Upwind deliverable D 4 (2010).

[49] Vugts, J., "Handbook of Bottom Founded Offshore Structures - Volume 1". Delft University of Technology. (2002).

[50] Wheeler, J. D. "Method for calculating forces produced by irregular waves." Journal of Petroleum Technology 22.03 (1970): 359-367.

[51] Wouter, K. "Lateral Soil - Structure Interaction". Offshore Wind Support Structure presentation. Delft University of Technology. (2014).

[52] Yeter, B., Garbatov Y. and Guedes Soares, C. "Spectral fatigue assessment of an offshore wind turbine structure under wave and wind loading." Frontiers of Discontinuous Numerical Methods and Practical Simulations in Engineering and Disaster Prevention (2013): 425.

[53] Zaaijer, M. B. "Foundation models for the dynamic response of offshore wind turbines." Proceedings of MAREC. (2002).

[54] Zaaijer, M. B. "Great expectations for offshore wind turbines: Emulation of wind farm design to anticipate their value for customers." Diss. TU Delft, Delft University of Technology. (2013).

[55] Zaaijer, M.B. "Strength and Fatigue". Introduction to Wind Energy presentation. Delft University of Technology. (2014).

Appendix A

PM-TD Validation Graphs

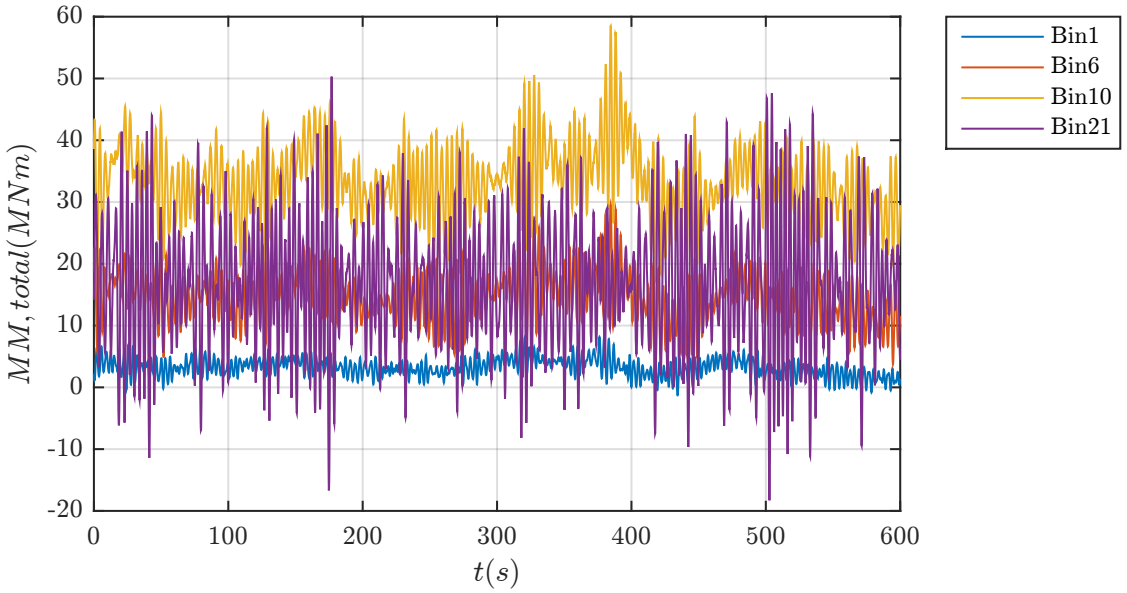

Figure A-1: Time-series of the mudline fore-aft moment at bin 1,6,10,21 produced by Bladed for the validation in Section 4-4.

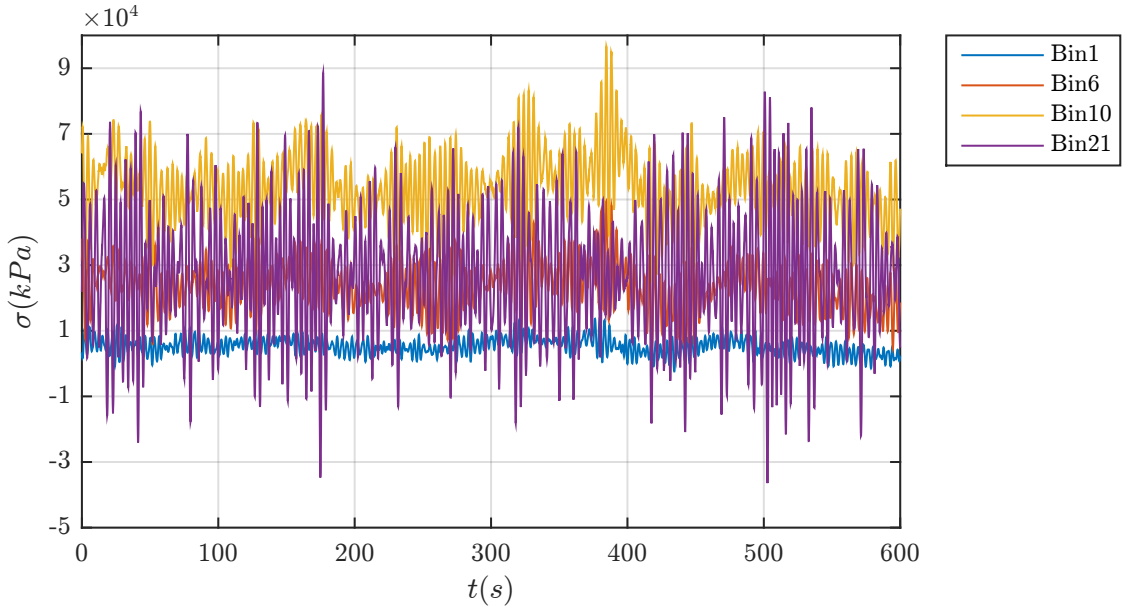

Figure A-2: Time-series of the mudline normal stresses (caused by fore-aft bending moment) at bin 1,6,10,21 produced by Bladed for the validation in Section 4-4.

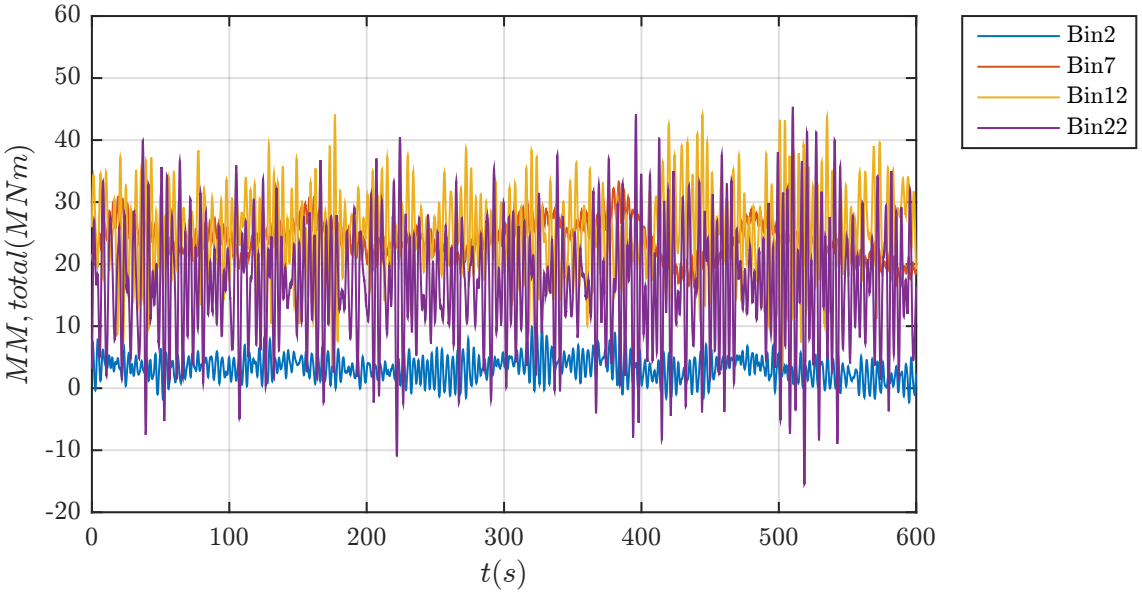

Figure A-3: Time-series of the mudline fore-aft moment at bin 2,7,12,22 produced by Bladed for the validation in Section 4-4.

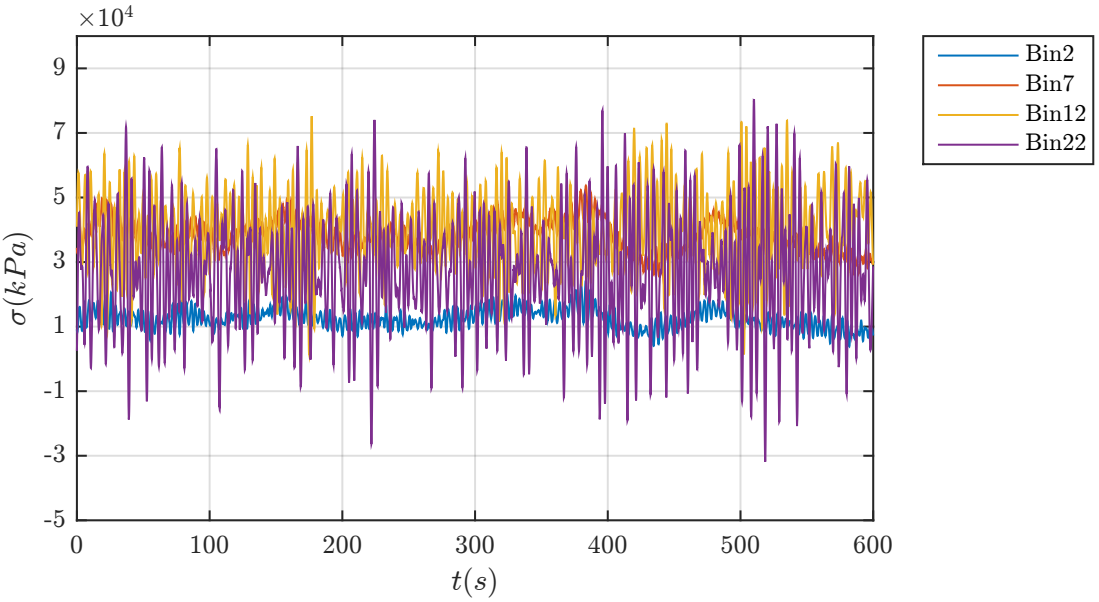

Figure A-4: Time-series of the mudline normal stresses (caused by fore-aft bending moment) at bin 2,7,12,22 produced by Bladed for the validation in Section 4-4.

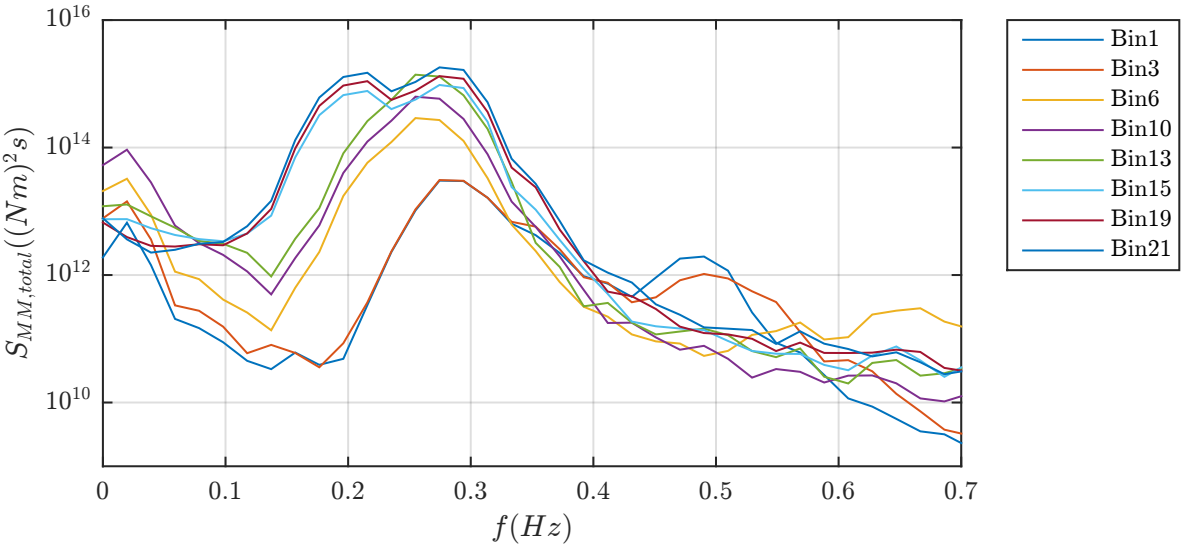

Figure A-5: PSD of the superposed fore-aft mudline moment generated by Bladed on the basis of FFT to the moment time-series for the validation in Section 4-4.

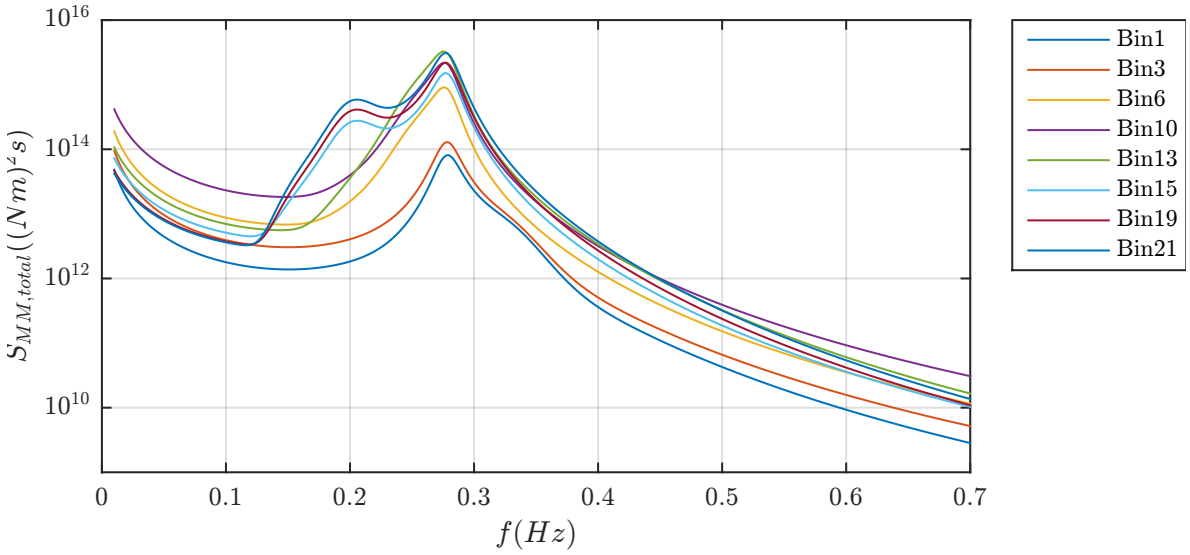

Figure A-6: PSD of the the superposed fore-aft mudline moment calculated by the proposed methodology for the validation in Section 4-4.

Appendix B

Detailed Results of the Sensitivity Analysis

Table B-1: Variation of the soil unit weight γ for the sensitivity analysis of Section 5-4.

Submerged unit weight variation			
γ (kN/m^3)	DEL (MNm)	γ (-)	DEL (-)
5	57.77	0.50	1.10
6	54.42	0.60	1.04
7	54.03	0.70	1.03
8	54.42	0.80	1.04
9	53.93	0.90	1.03
10	52.35	1.00	1.00
11	51.36	1.10	0.98
12	50.77	1.20	0.97
13	50.18	1.30	0.96
14	49.49	1.40	0.95
15	49.00	1.50	0.94

Table B-2: Variation of the wave peak period T_P (globally applied factor to Table 4-2) for the sensitivity analysis of Section 5-4.

Wave peak period variation		
T_p $(-)$	DEL (MNm)	DEL (-)
0.50	34.71	0.66
0.60	50.48	0.96
0.70	61.71	1.18
0.80	64.08	1.22
0.90	57.38	1.10
1.00	52.35	1.00
1.10	46.93	0.90
1.20	38.65	0.74
1.30	36.68	0.70
1.40	35.69	0.68
1.50	33.72	0.64
1.60	32.73	0.63
1.70	32.73	0.63
1.80	31.75	0.61

Table B-3: Variation of the sand friction angle ϕ for the sensitivity analysis of Section 5-4.

Friction angle variation			
ϕ (deg)	DEL (MNm)	ϕ (-)	DEL (-)
20	58.86	0.67	1.13
21	58.56	0.70	1.12
22	56.88	0.73	1.09
23	55.01	0.77	1.05
24	54.03	0.80	1.04
25	53.93	0.83	1.03
26	54.22	0.87	1.04
27	54.42	0.90	1.04
28	54.32	0.93	1.04
29	53.24	0.97	1.02
30	52.15	1.00	1.00
31	51.36	1.03	0.98
32	50.77	1.07	0.97
33	50.18	1.10	0.96
34	49.49	1.13	0.95
35	48.51	1.17	0.93
36	47.91	1.20	0.92
37	47.32	1.23	0.91
38	46.53	1.27	0.89
39	45.55	1.30	0.87
40	45.45	1.33	0.87

Table B-4: Variation of the water depth d for constant and adjusted penetration depth L_P (2 right-most columns of DEL) for the sensitivity analysis of Section 5-4.

Water depth variation					
$d\ (m)$	$DEL\ (MNm)$	d (-)	DEL (-)	$DEL\ (MNm)$	DEL (-)
10	29.78	0.50	0.57	27.81	0.53
11	31.75	0.55	0.61	29.78	0.57
12	32.73	0.60	0.63	31.75	0.61
13	34.71	0.65	0.66	32.73	0.63
14	36.38	0.70	0.69	34.71	0.66
15	37.47	0.75	0.72	35.69	0.68
16	41.61	0.80	0.79	37.17	0.71
17	45.55	0.85	0.87	40.62	0.78
18	48.51	0.90	0.93	46.34	0.89
19	50.58	0.95	0.97	49.79	0.95
20	52.35	1.00	1.00	52.35	1.00
21	56.59	1.05	1.08	57.38	1.10
22	59.45	1.10	1.14	59.55	1.14
23	61.42	1.15	1.17	61.20	1.17
24	62.80	1.20	1.20	63.49	1.21
25	63.84	1.25	1.22	65.03	1.24
26	64.60	1.30	1.23	64.81	1.24
27	65.20	1.35	1.25	62.11	1.19
28	65.72	1.40	1.26	56.00	1.07
29	72.06	1.45	1.38	49.69	0.95
30	78.77	1.50	1.50	41.61	0.79

Table B-5: Variation of the mean wind speed $\bar{U}$ (globally applied factor to Table 4-2) for the sensitivity analysis of Section 5-4.

Mean wind speed variation		
$\bar{U}\ (-)$	$DEL\ (MNm)$	$DEL\ (-)$
0.50	50.08	0.96
0.60	50.58	0.97
0.70	51.07	0.98
0.80	51.46	0.98
0.90	51.66	0.99
1.00	52.35	1.00
1.10	53.24	1.02
1.20	53.73	1.03
1.30	54.42	1.04
1.40	55.01	1.05
1.50	55.80	1.07
1.60	56.69	1.08
1.70	57.38	1.10
1.80	57.87	1.11

Table B-6: Variation of the turbulence intensity TI (globally applied factor to Table 4-2) for the sensitivity analysis of Section 5-4.

Turbulence intensity variation		
TI $(-)$	DEL (MNm)	DEL (-)
0.50	50.18	0.96
0.60	50.48	0.96
0.70	50.77	0.97
0.80	51.17	0.98
0.90	51.46	0.98
1.00	52.35	1.00
1.10	54.12	1.03
1.20	55.90	1.07
1.30	57.38	1.10
1.40	58.95	1.13
1.50	60.33	1.15
1.60	61.52	1.18
1.70	62.55	1.19
1.80	63.45	1.21

Table B-7: Variation of the wave height H_s (globally applied factor to Table 4-2) for the sensitivity analysis of Section 5-4.

Wave height variation		
H_s $(-)$	DEL (MNm)	DEL (-)
0.50	35.69	0.68
0.60	37.27	0.71
0.70	41.61	0.79
0.80	46.53	0.89
0.90	49.98	0.95
1.00	52.35	1.00
1.10	58.07	1.11
1.20	61.59	1.18
1.30	63.82	1.22
1.40	65.30	1.25
1.50	74.53	1.42
1.60	86.46	1.65
1.70	94.93	1.81
1.80	101.14	1.93

Appendix C

Case Study Set-up Specifications and Results

Table C-1: Lumped environmental states for the reference location of Hornsea

Local climate for the reference location					
State	$U(m/s)$	$TI(\%)$	$H_s(m)$	$T_P(s)$	Occurence (%)
1	3.8	26.5	0.3	6.0	7.5
2	4.7	23.2	0.3	4.6	7.8
3	4.7	23.2	0.6	5.6	10.6
4	4.2	22.4	1.3	8.8	6.7
5	5.7	19.4	1.3	7.1	17.6
6	6.1	19.4	0.9	4.6	15.8
7	6.7	18.7	1.8	8.5	5.8
8	7.2	17.9	1.9	7.2	9.7
9	9.0	16.2	2.3	8.5	4.6
10	9.5	16.2	2.8	11.2	0.5
11	9.6	16.2	2.6	9.8	2.4
12	10.8	15.8	2.8	9.8	4.1
13	11.0	15.8	3.1	11.2	0.5
14	12.4	15.2	3.6	11.2	0.8
15	14.9	14.4	2.9	8.5	2.4
16	15.8	13.9	3.3	10.1	1.9
17	20.5	12.8	3.8	9.8	0.5
18	27.8	12.1	4.3	11.8	0.8

Table C-2: Lumped environmental states for the location 1 of Hornsea

Local climate for location 1					
State	$U(m/s)$	$TI(\%)$	$H_s(m)$	$T_P(s)$	Occurence (%)
1	3.8	26.5	0.2	6.0	7.5
2	4.7	23.2	0.2	4.6	7.8
3	4.7	23.2	0.6	5.6	10.6
4	4.4	22.4	1.3	8.8	6.7
5	5.7	19.5	1.3	7.1	17.6
6	6.1	19.5	0.9	4.6	15.8
7	6.4	18.3	1.7	8.5	5.8
8	7.4	17.5	1.8	7.2	9.7
9	8.9	15.8	2.2	8.5	4.6
10	9.4	15.8	2.7	11.2	0.5
11	9.5	15.8	2.5	9.8	2.4
12	10.4	15.4	2.7	9.8	4.1
13	10.6	15.4	3.0	11.2	0.5
14	12.0	14.7	3.5	11.2	0.8
15	14.1	14.4	2.8	8.5	2.4
16	15.1	14.1	3.2	10.1	1.9
17	20.4	12.7	3.7	9.8	0.5
18	27.6	12.1	4.2	11.8	0.8

Table C-3: Lumped environmental states for the location 2 of Hornsea

Local climate for location 2					
State	$U(m/s)$	$TI(\%)$	$H_s(m)$	$T_P(s)$	Occurence (%)
1	3.8	26.5	0.2	6.0	7.5
2	4.7	23.2	0.2	4.6	7.8
3	4.7	23.2	0.5	5.6	10.6
4	4.3	22.4	1.2	8.8	6.7
5	5.9	19.0	1.2	7.1	17.6
6	6.4	19.0	0.8	4.6	15.8
7	6.6	17.8	1.6	8.5	5.8
8	7.8	16.9	1.7	7.2	9.7
9	9.9	15.1	2.1	8.5	4.6
10	10.4	15.1	2.6	11.2	0.5
11	10.6	15.1	2.4	9.8	2.4
12	11.6	14.6	2.6	9.8	4.1
13	11.8	14.6	2.8	11.2	0.5
14	12.9	14.2	3.3	11.2	0.8
15	15.0	13.9	2.6	8.5	2.4
16	15.8	13.6	3.0	10.1	1.9
17	20.5	12.5	3.5	9.8	0.5
18	27.9	11.9	3.9	11.8	0.8

Table C-4: Lumped environmental states for the location 3 of Hornsea

Local climate for location 3					
State	$U(m/s)$	$TI(\%)$	$H_s(m)$	$T_P(s)$	Occurence (%)
1	3.8	26.5	0.3	6.0	7.5
2	4.7	23.2	0.3	4.6	7.8
3	4.7	23.2	0.6	5.6	10.6
4	4.3	22.4	1.3	8.8	6.7
5	5.9	19.0	1.3	7.1	17.6
6	6.4	19.0	0.9	4.6	15.8
7	6.6	17.8	1.8	8.5	5.8
8	7.7	16.9	1.9	7.2	9.7
9	9.5	15.1	2.3	8.5	4.6
10	10.0	15.1	2.8	11.2	0.5
11	10.2	15.1	2.6	9.8	2.4
12	11.1	14.6	2.8	9.8	4.1
13	11.3	14.6	3.1	11.2	0.5
14	12.4	14.2	3.6	11.2	0.8
15	14.4	14.1	2.9	8.5	2.4
16	15.3	13.8	3.3	10.1	1.9
17	20.4	12.6	3.8	9.8	0.5
18	27.7	11.9	4.3	11.8	0.8

Table C-5: Lumped environmental states for the location 4 of Hornsea

Local climate for location 4					
State	$U(m/s)$	$TI(\%)$	$H_s(m)$	$T_P(s)$	Occurence (%)
1	3.8	26.5	0.3	6.0	7.5
2	4.7	23.2	0.3	4.6	7.8
3	4.7	23.2	0.6	5.6	10.6
4	3.6	22.4	1.4	8.8	6.7
5	4.8	19.0	1.4	7.1	17.6
6	5.2	19.0	0.9	4.6	15.8
7	6.8	17.8	1.8	8.5	5.8
8	8.0	16.9	2.0	7.2	9.7
9	9.2	16.0	2.4	8.5	4.6
10	9.7	16.0	3.0	11.2	0.5
11	9.9	16.0	2.7	9.8	2.4
12	10.9	15.5	3.0	9.8	4.1
13	11.1	15.5	3.3	11.2	0.5
14	12.3	15.2	3.8	11.2	0.8
15	15.3	14.1	3.1	8.5	2.4
16	16.0	13.7	3.5	10.1	1.9
17	20.7	12.6	4.0	9.8	0.5
18	27.9	12.0	4.5	11.8	0.8

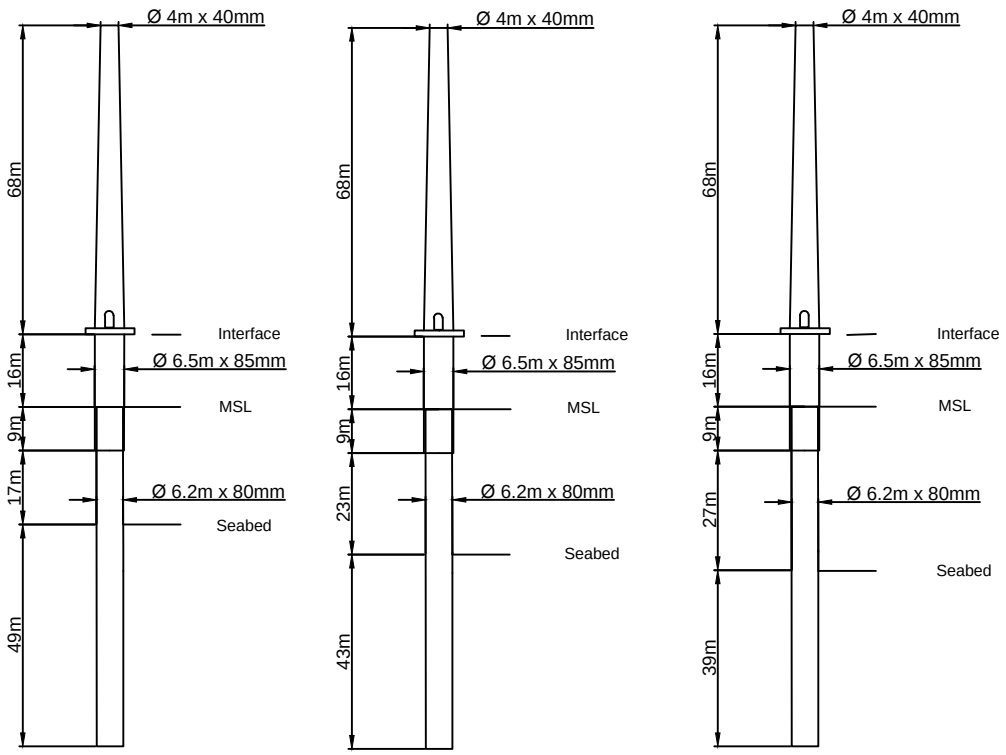

Figure C-1: The support structure used in the case study installed in different locations (from left to right): location 4, 1 and 2, while location 3 has the same depth as in the reference (Fig. 6-5

Table C-6: Results of extrapolating fatigue applying the PM and verifying them with TD at the 4 locations of the case study and under different elevations as defined in Fig. 6-8

Extrapolation at different elevations: $\Delta\sigma_{EQ}$ (MPa)										
Loc.	Elev. (i)		Elev. (ii)		Elev. (iii)		Elev. (iv)		Elev. (v)	
	TD	PM	TD	PM	TD	PM	TD	PM	TD	PM
1	52.8	47.5	48.8	46.2	43.7	41.3	21.3	17.3	21.2	17.8
2	58.6	55.0	53.8	52.8	46.4	43.4	23.2	18.6	23.2	18.9
3	44.6	45.1	44.6	45.1	43.8	40.9	22.3	18.1	22.3	18.4
4	39.5	42.6	-	-	39.5	37.6	16.7	16.9	19.0	17.0